

ClimSim-Online: A Large Multi-Scale Dataset and Framework for Hybrid Physics-ML Climate Emulation

Sungduk Yu^{1,2*}, Zeyuan Hu^{3,4*†}, Akshay Subramaniam³, Walter Hannah⁵, Liran Peng¹, Jerry Lin¹, Mohamed Aziz Bhourri⁶, Ritwik Gupta⁷, Björn Lütjens⁸, Justus C. Will¹, Gunnar Behrens⁹, Julius J. M. Busecke⁶, Nora Loose¹⁰, Charles I Stern⁶, Tom Beucler¹¹, Bryce Harrop¹², Helge Heuer⁹, Benjamin R Hillman¹³, Andrea Jenney¹⁴, Nana Liu¹⁵, Alistair White^{16,17}, Tian Zheng⁶, Zhiming Kuang⁴, Fiaz Ahmed¹⁸, Elizabeth Barnes¹⁹, Noah D. Brenowitz³, Christopher Bretherton²⁰, Veronika Eyring⁹, Savannah Ferretti¹, Nicholas Lutsko²¹, Pierre Gentine⁶, Stephan Mandt¹, J. David Neelin¹⁸, Rose Yu²¹, Laure Zanna²², Nathan M. Urban²³, Janni Yuval²⁴, Ryan Abernathey⁶, Pierre Baldi¹, Wayne Chuang⁶, Yu Huang⁶, Fernando Iglesias-Suarez²⁵, Sanket Jantre²³, Po-Lun Ma¹², Sara Shamekh²², Guang Zhang²¹, Michael Pritchard^{1,3}

¹UCI, ²Intel Labs, ³NVIDIA, ⁴Harvard, ⁵LLNL, ⁶Columbia, ⁷UCB, ⁸MIT, ⁹DLR, ¹⁰Princeton, ¹¹UNIL, ¹²PNNL, ¹³SNL, ¹⁴OSU, ¹⁵CIWRO/NOAA, ¹⁶TUM, ¹⁷PIK, ¹⁸UCLA, ¹⁹CSU, ²⁰Allen AI, ²¹UCSD, ²²NYU, ²³BNL, ²⁴Google Research, ²⁵PRED

Editor: Kilian Weinberger

Abstract

Modern climate projections lack adequate spatial and temporal resolution due to computational constraints, leading to inaccuracies in representing critical processes like thunderstorms that occur on the sub-resolution scale. Hybrid methods combining physics with machine learning (ML) offer faster, higher fidelity climate simulations by outsourcing compute-hungry, high-resolution simulations to ML emulators. However, these hybrid physics-ML simulations require domain-specific data and workflows that have been inaccessible to many ML experts.

This paper is an extended version of our NeurIPS award-winning ClimSim dataset paper (Yu et al., 2024). The ClimSim dataset includes 5.7 billion pairs of multivariate input/output vectors spanning ten years at high temporal resolution, capturing the influence of high-resolution, high-fidelity physics on a host climate simulator’s macro-scale state. In this extended version, we introduce a significant new contribution in Section 5, which provides a cross-platform, containerized pipeline to integrate ML models into operational climate simulators for hybrid testing. We also implement various baselines of ML models and hybrid simulators to highlight the ML challenges of building stable, skillful emulators.

The data (https://huggingface.co/datasets/LEAP/ClimSim_high-res¹) and code² are publicly released to support the development of hybrid physics-ML and high-fidelity climate simulations.

*. Equal contribution

†. Correspondence: zeyuanh@nvidia.com

1. Also in a low-resolution version (https://huggingface.co/datasets/LEAP/ClimSim_low-res) and an aquaplanet version (https://huggingface.co/datasets/LEAP/ClimSim_low-res_aqua-planet).

2. <https://leap-stc.github.io/ClimSim> and <https://github.com/leap-stc/climsim-online>

Keywords: Multi-Scale Dataset, Machine Learning Benchmark, Climate Emulation, Hybrid Physics-ML Climate Simulation, End-to-End Workflow

1. Introduction³

1.1 Overview

Projections from numerical Earth system simulators are the primary tool informing policy on climate change (Tebaldi et al., 2021). However, current climate simulators poorly represent clouds and extreme rainfall physics (IPCC, 2021; Sherwood et al., 2020) despite stretching the limits of the world’s most powerful supercomputers. This is because the required computational power to simulate Earth system complexity imposes significant restrictions on the simulations’ spatial resolution (Schneider et al., 2017; Gentine et al., 2021). Physics occurring on scales smaller than the temporal and/or spatial resolutions of climate simulations are commonly represented using empirical or physically inspired mathematical representations called “parameterizations”. Assumptions in these parameterizations often lead to errors that can grow into inaccuracies in the future predicted climate.

Machine learning (ML) is an attractive approach for learning the complex nonlinear sub-resolution physics—processes (and properties) occurring on scales smaller than typical climate simulator resolution—from short, higher fidelity simulations. The implementation of physics-ML parameterizations has the exciting possibility of resulting in hybrid climate simulations that are both cheaper and more accurate than current state-of-the-art model simulations (Gentine et al., 2018; Eyring et al., 2021).

Traditional Earth system simulators have a typical smallest resolvable scale of 80–200 km in the horizontal direction (Eyring et al., 2016), equivalent to the size of a typical U.S. county. In contrast, the community has achieved 1-10 km resolution, global storm-resolving simulators, though these models are still being tested for their use in long-term climate simulations and are very computationally demanding (e.g., Taylor et al., 2023; Hohenegger et al., 2023; Mooers et al., 2023; Hoefler et al., 2023). Accurately representing cloud formation requires a resolution of 100 m or finer, demanding six orders of magnitude increase in computational power.

ML presents a conceivable solution to sidestep the limitations of classical computing (Eyring et al., 2021, 2024b,a). It enables hybrid-ML climate simulations that integrate traditional numerical methods—which solve the equations governing large-scale fluid motions of Earth’s atmosphere—with ML-based parameterizations that emulate the macro-scale effects of small-scale physics. Instead of relying on heuristic assumptions about these small-scale processes, ML-based parameterizations learn directly from data generated by short-duration, high-resolution simulations (Bretherton et al., 2022; Clark et al., 2022a; Grundner et al., 2022; Sanford et al., 2023b; Gentine et al., 2018; Rasp et al., 2018; Brenowitz et al., 2020; Han et al., 2020; Ott et al., 2020; Mooers et al., 2021; Wang et al., 2022b; Han et al., 2023; Iglesias-Suarez et al., 2023; Yuval and O’Gorman, 2020; Yuval et al., 2021; Heuer et al., 2024; Niu et al., 2024). This task is a nonlinear regression problem: in the climate simulation, a physics-ML parameterization returns the large-scale outputs—changes in wind, moisture,

3. For a brief overview of key climate-science concepts and terminology relevant to this section, see Appendix A.1.

or temperature—that occur due to unresolved small-scale (sub-resolution) physics, given large-scale resolved inputs (e.g., temperature, wind velocity; see Section 4).

While several proofs of concept have emerged in recent years, hybrid-ML climate simulators have yet to be sufficiently stable or well-understood to be ready for operational use. Our initial benchmarking work recognized that obtaining sufficient, complete training data had been a major challenge impeding progress from the ML community. This data must contain all macro-scale variables that regulate the behavior of subgrid-scale physics and be compatible with hybrid-ML climate simulations. Addressing this using training data from uniformly high-resolution simulations has proven to be very expensive and requires coarse-graining the high-resolution data, potentially leading to issues when coupled with a host climate simulation (Ross et al., 2023).

A promising solution is to utilize multi-scale climate simulation methods to generate training data. These simulations embed high-resolution physics solvers within each grid column of a host climate simulator to explicitly resolve small-scale physics (see Appendix A.1 for more details). Crucially, this provides a clean interface between the learned high-resolution physics and the host climate simulator’s macro-scale dynamics (Rasp, 2020). In theory, this makes hybrid simulations approachable and tractable. In practice, the full potential of multi-scale simulations remains largely untapped due to a scarcity of existing datasets, exacerbated by the combination of operational simulation code complexity and the need for domain expertise in choosing variables. To further complicate matters, the absence of a straightforward method for testing learned ML emulators in hybrid settings renders the problem even less approachable.

1.2 The ClimSim-Online Framework: Bridging Offline Training and Online Evaluation

Following our Outstanding Paper Award for the original ClimSim dataset paper at NeurIPS 2023 (Yu et al., 2024), we were invited to provide this extended version. The ClimSim dataset remains the largest and most physically comprehensive dataset for training ML emulators of full subgrid-scale physics (atmospheric storms, clouds, turbulence, rainfall, and radiation) for use in hybrid-ML climate simulations. The ClimSim dataset offers a comprehensive collection of inputs and outputs from multi-scale climate model simulations, offering a foundation for developing robust frameworks that learn subgrid-scale processes related to cloud physics. These data have already led to impact via a Kaggle ML competition at the scale of thousands of machine learning experts (Lin et al., 2024).

A major challenge in hybrid-ML climate simulation is ensuring that ML models trained in an offline setting, using precomputed high-resolution simulation data, also perform stably and accurately in an online setting, where they interact dynamically with the host climate simulator. In this manuscript, we define “offline training” as the traditional supervised learning task, where a regression or generative machine learning (ML) model is trained to map input features to target features. Offline metrics (Section 4.2) assess how well an ML model performs this mapping for samples at each individual location and time step, using a fixed dataset.

In contrast, “online evaluation” has domain-specific meaning in our context, and refers to evaluating the performance of the hybrid climate simulator in which many instances

of its embedded high-resolution physics solver are replaced with copies of a trained ML parameterization that is then allowed to feed back with resolved planetary-scale climate dynamics. That is, the evaluation data changes dynamically. This involves assessing how accurately the hybrid simulation can replicate climate statistics, such as temporally- and spatially-mean atmospheric states, compared to a pure physical climate simulation (see Section 5.2 for more online evaluation metrics).

In this extended version compared to the original NeurIPS version, our main new contribution is presented in Section 5, where we introduce a containerized, cross-platform pipeline for integrating ML models into a host climate simulator, facilitating the evaluation of online performance in hybrid-ML simulations. This containerized workflow ensures reproducibility and ease of use, making it accessible to ML researchers without domain knowledge. Additionally, Section 5 documents stable and skillful hybrid-ML simulations from Hu et al. (2025), providing a benchmark illustrating recommended domain-specific metrics for measuring the online performance of simulated climate despite the presence of intrinsic internal variability. Furthermore, we share in Section 5 experiences and insights on how to improve online performance, and establish an online skill baseline worthy of additional competition.

We refer to the combination of this containerized pipeline and the original ClimSim dataset as ClimSim-Online, which serves as an end-to-end framework for developing hybrid climate simulators. It is intended to be more accessible than the typical simulation workflows that tend to be tailored to specific high-performance computing environments used by the limited community of climate modeling specialists. ClimSim-Online was prepared by atmospheric scientists, climate simulator developers, and ML researchers to lower the entry barrier for ML experts on this important problem, with the ultimate goal of helping improve the performance and accuracy of climate simulators used for long-term projections.

2. Related Work

Several benchmark datasets have been developed to facilitate AI tasks in weather and climate. For example, the European Center for Medium-Range Weather Forecasts (ECMWF) reanalysis v5 (ERA5, Hersbach et al., 2020) is a comprehensive dataset of global weather from 1940 to present. The WeatherBench 2 benchmark dataset provides data specifically designed for training and evaluating data-driven weather forecasting models, focusing on global, medium range (1-15days) prediction (Rasp et al., 2024). ClimateBench (Watson-Parris et al., 2022) was designed for emulators that produce annual mean global predictions of temperature and precipitation given greenhouse gas concentrations and emissions. ClimateBench is limited to data from a single climate simulator. In contrast, ClimateSet (Kaltenborn et al., 2023) expands ClimateBench by offering a large-scale dataset with inputs and outputs from 36 climate simulators. ClimART (Cachay et al., 2021) was designed for the development of radiative energy transfer parameterization emulators for use in weather and climate modeling. Appendix G documents more climate or weather related benchmark datasets.

However, ClimSim is unique for its focus on learning ML parameterizations which can be used in hybrid climate simulations. Unlike other datasets, ClimSim is designed to capture the nonlinear effects of clouds, rain, storms, and radiation at kilometer scales. It provides an end-

to-end framework to emulate an embedded component—the cloud-resolving simulator—in multi-scale climate simulators and to evaluate the resulting hybrid climate simulations.

There have been several recent efforts to produce hybrid-ML models learning from multi-scale climate simulations, analogous to ClimSim (Gentine et al., 2018; Rasp et al., 2018; Han et al., 2020; Ott et al., 2020; Mooers et al., 2021; Wang et al., 2022b; Lin et al., 2023; Iglesias-Suarez et al., 2023; Han et al., 2023). Most of these focused on simple aquaplanets (Gentine et al., 2018; Rasp et al., 2018; Han et al., 2020; Ott et al., 2020; Lin et al., 2023; Iglesias-Suarez et al., 2023), while simulations that included real geography (Mooers et al., 2021; Wang et al., 2022b; Han et al., 2023) did not include enough variables for complete land-surface coupling, to our knowledge. Most examine simple multi-layer perceptrons, except for Han et al. (2020); Wang et al. (2022b); Han et al. (2023), who used a ResNet architecture, Heuer et al. (2024); Hu et al. (2025), who used a U-Net architecture, and Behrens et al. (2025), who used a variational encoder-decoder that accounts for stochasticity. Although hybrid testing in real-geography settings is error-prone, several studies (Wang et al., 2022b; Han et al., 2023; Kochkov et al., 2024) have demonstrated some hybrid stability. Compressing input data to avoid causal confounders may improve online accuracy (Iglesias-Suarez et al., 2023; Kühbacher et al., 2024), and methods have been developed to enforce physical constraints (Beucler et al., 2021; Reed et al., 2023).

Compared to the training data used above, upon its inception, ClimSim’s comprehensive variable coverage was unprecedented, by including all variables needed to be coupled to a land system simulator and enough to begin enforcing physical constraints. Its availability across coarse-resolution, high-resolution, aquaplanet and real-geography use cases was also new to the community.

In non-multi-scale settings, an important body of related work (Bretherton et al., 2022; Clark et al., 2022a; Kwa et al., 2023; Sanford et al., 2023b) has made exciting progress on using analogous hybrid ML approaches to reduce biases in uniform resolution climate simulations, including in an operational climate code with land coupling and online stability (Yuval and O’Gorman, 2020; Yuval et al., 2021). Other related work includes full model emulation (FME) for short-term weather prediction (Pathak et al., 2022; Bonev et al., 2023; Lam et al., 2022) and for long-term climate simulation (Watt-Meyer et al., 2023, 2024). While ClimSim is focused on hybrid-ML climate simulations and we do not demonstrate FME baselines, ClimSim contains full atmospheric state variable samplings well suited for the FME task.

3. ClimSim Dataset

This section provides an overview of the ClimSim dataset. ClimSim is designed to facilitate the development of ML parameterizations for hybrid climate simulations. The dataset includes inputs $x \in \mathbb{R}^{d_i}$ (with $d_i = 124$ for standard inputs and $d_i = 617$ for expanded inputs) representing the local vertical structure of macro-scale state variables and boundary conditions, and targets $y \in \mathbb{R}^{d_o}$ (with $d_o = 128$ for standard targets and $d_o = 368$ for expanded targets) representing tendencies due to unresolved processes and surface fluxes for surface coupling. Generated using the E3SM-MMF multi-scale climate simulator over 10 simulated years, the dataset comprises 5.7 billion high-resolution samples (41.2TB) and 100 million low-resolution samples (744GB). We partition the 10-year dataset into training/validation

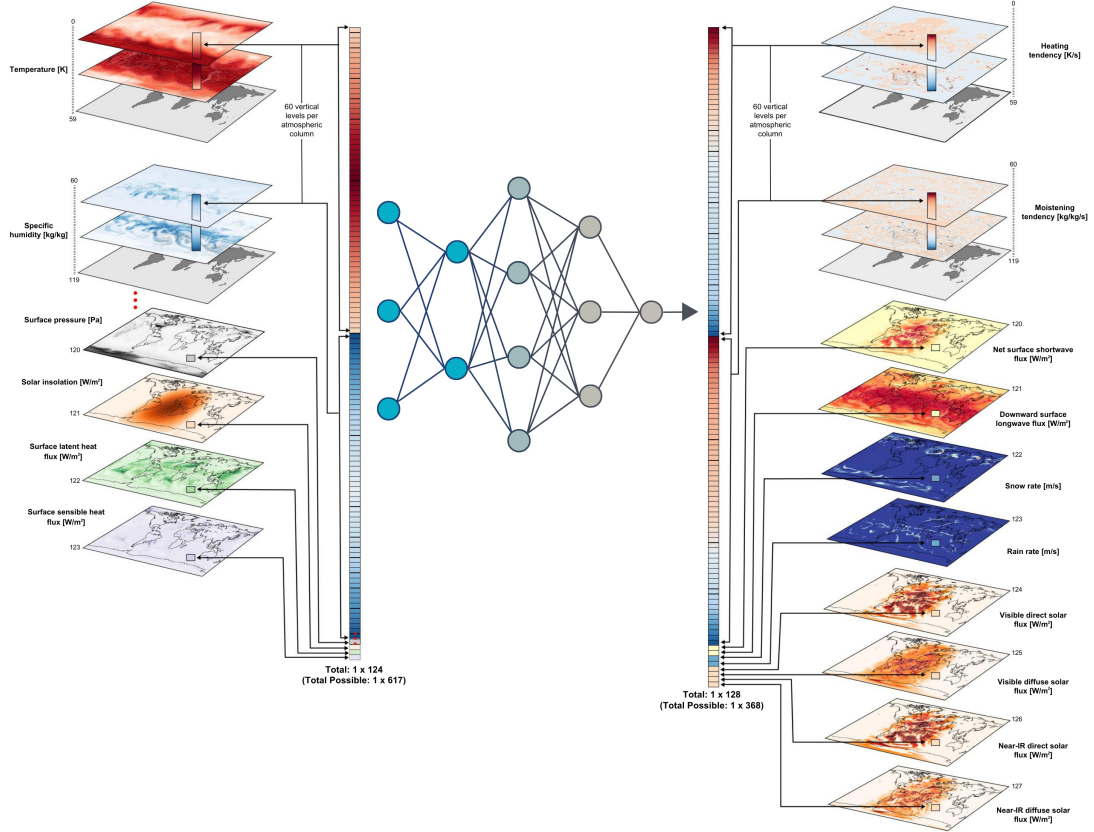


Figure 1: Schematic of the spatially-local version of ClimSim that our baseline architectures are trained with. The inputs x consist of a set of macro-scale state variables. The targets y represent tendencies of unresolved processes and surface fluxes.

(first 8 years: 0001-02 to 0009-01, excluding the initial spin-up month) and test (the remaining 2 years: 0009-03 to 0011-02), with a one-month gap to avoid test contamination via temporal correlation. Offline training involves learning an ML parameterization by mapping inputs to targets for each sample (an atmospheric column at a single timestep). ClimSim-Online provides an accessible end-to-end workflow to integrate a trained ML parameterization into a host climate simulator to perform hybrid simulations. Climate statistics in these hybrid simulations are evaluated against those from pure physical E3SM-MMF simulations.

The rest of this section provides a detailed breakdown of the dataset’s structure, including its experimental design, data collection methodology, spatial characteristics, technical interface, and energy footprint.

Experiment Outline: As shown in Figure 1, the core regression task maps atmospheric column states (inputs) to subgrid tendencies (targets). The input represents the local vertical structure (in horizontal location and time) of macro-scale state variables in a multi-scale physical climate simulator before any adjustments from subgrid-scale convection and radiation are made. The input also includes concatenated scalars containing boundary conditions of incoming radiation at the top of the atmospheric column and land surface model constraints at its base. The target vector contains the tendencies of the same state variables representing the impact of unresolved processes (e.g., redistribution of water, related phase changes, and radiative heating due to convection). The output vector represents the horizontally averaged change in atmospheric state after the computationally demanding subcycling of nested simulators. The ultimate goal is to outsource these physics to ML by mapping inputs to targets at comparable fidelity. The target vector includes scalar fields and fluxes from the bottom of the atmospheric column expected by the land surface model component that it must couple to; land-atmosphere coupling is crucial to predicting regional water cycle dynamics (Fischer et al., 2007; Seneviratne et al., 2010).

Importantly, ClimSim also includes the option for *expanded inputs* $x \in \mathbb{R}^{d_i}$ of size $d_i = 617$ and targets $y \in \mathbb{R}^{d_o}$ of size $d_o = 368$, which we demonstrate in one of our experiments. This configuration is necessary for fully interactive coupling to the host climate simulator.

Dataset Collection: We ran the E3SM-MMF multi-scale climate simulator (Hannah et al., 2020; Norman et al., 2022; Hannah et al., 2022, 2021), using multiple NVIDIA A100 GPUs for a total of $\sim 9,800$ GPU-hours. We saved instantaneous values from every grid column of the atmospheric state before and after high-resolution calculations occurred, isolating state updates due to explicitly-resolved moist convection, boundary layer turbulence, and radiation; details of the E3SM-MMF climate simulator configuration can be found in the Appendix A.2. These data were saved at 20-minute intervals (i.e., the time step of the host climate simulator) for 10 simulated years (excluding one-month spinup), resulting in 5.7 billion samples for the high-resolution simulation that uses an unstructured “cubed-sphere” horizontal grid with 21,600 grid columns spanning the globe. This grid yields an *approximate* horizontal grid spacing of 1.5° , but unlike a traditional climate simulator that maps points across the sphere using two dimensions aligned with cardinal north/south and east/west directions, unstructured grids use a single dimension to organize the horizontal location of points. The unstructured “cubed-sphere” computational mesh used by the climate simulator, which projects a cube onto the sphere, effectively avoiding the polar singularity problems associated with regular Cartesian grids (Ronchi et al., 1996; Hannah et al., 2022). The atmospheric columns at each location and time are treated as independent samples. Thus,

the total number of samples can be understood as 5.7 billion $\approx 21,600$ horizontal locations per time step $\times 72$ -time steps per simulated day $\times 3,650$ simulated days. It is important to note that each sample retains a 1D structure corresponding to the vertical variation across 60 levels.

We also ran two additional E3SM-MMF simulations with approximately ten times less horizontal resolution, with only 384 grid columns spanning the globe, resulting in 100 million samples for each simulation. These low-resolution options allow for fast prototyping of ML models due to smaller training data volumes and less geographic complexity. One low-resolution simulation uses an “aquaplanet” configuration, i.e., a lower boundary condition of specified sea surface temperature, invariant in the longitudinal dimension with no seasonal cycle. This is the simplest prototyping dataset, removing variance associated with continents and time-varying boundary conditions.

The input and target variables in this dataset were selected based on the design of E3SM-MMF. We have included all variables involved in the interface between the host climate simulator and the embedded cloud-resolving simulators.

Locality vs. Nonlocality: A spatially-global version of the problem could be of practical use for improving ML via helpful spatial context (Wang et al., 2022a; Lütjens et al., 2022). In this case, information from other grid columns across the globe is taken into account. Thus, the problem becomes a $2D \rightarrow 2D$ regression task with inputs $x \in \mathbb{R}^{d_i}$ of maximum size $d_i = 617 \times 21,600$ (grid columns) and targets, $y \in \mathbb{R}^{d_o}$, of maximum size $d_o = 368 \times 21,600$.

Dataset Interface: Raw model outputs emerge from the climate simulator as standard NetCDF files, which can be easily parsed. Each timestep yields files containing input and target vectors separately, resulting in a total of 525,600 files for each of the three datasets. To prevent redundancy, variable metadata and grid information were saved separately.

The raw tensors from the climate simulations are initially either 2D or 3D, depending on the variable. For 2D tensors, the dimensions represent time and horizontal location. While these variables actually depend on three physical dimensions (time and 2D space), since each location on the sphere is indexed along a single axis due to the climate simulator’s unstructured horizontal grid, the apparent dimensionality is lower. Such variables include solar insolation, snow depth over land, surface energy fluxes, and surface precipitation rate. 3D tensors include the additional dimension representing altitude relative to the Earth’s surface for height-varying state variables like temperature, humidity, and wind vector components. Separate files are used to store each timestep and variable. ClimSim includes a total of 24 2D variables and 10 3D variables (see Table 4 in the Appendix).

Energy use: The computing and energy costs of generating ClimSim were approximately 9,800 GPU hours. While this could be viewed as wasteful and having a negative consequence for society through associated emissions (Luccioni and Hernandez-Garcia, 2023), we emphasize that the compute used is actually orders of magnitude less than what is consumed by operational climate prediction. For example, producing a 1,000-year high-resolution E3SM-MMF climate simulation would require approximately 960,000 GPU hours—nearly 100 times the compute cost of generating ClimSim. Simulations of this volume are commonly used in climate research to establish baseline climate conditions, such as in preindustrial control experiments conducted within the Coupled Model Intercomparison Project (CMIP6) (Eyring et al., 2016), and to calibrate their performance. Furthermore, emissions associated with ClimSim are minimized given that our E3SM-MMF simulations were performed on

energy-efficient GPU hardware. The cost must also be weighed against the potential social benefit of mitigating future energy consumption by eliminating end users’ need for costly physics-based multi-scale climate simulations. ClimSim’s resource usage is a one-time cost that facilitates ongoing research, which could lead to significant advancements in climate modeling and policy, potentially offsetting its energy footprint.

4. Offline Experiments

This section focuses on the offline scores that accompanied our NeurIPS publication, where we guide ML practitioners using ClimSim. Therein, we provide an example ML workflow using the low-resolution, real-geography dataset to train ML models to predict target outputs from the provided inputs. All but one of our baselines focus on emulating the subset of total available input and target variables illustrated in Figure 1, with the following inputs $x \in \mathbb{R}^{d_i}$ of size $d_i = 124$, and targets $y \in \mathbb{R}^{d_o}$ of size $d_o = 128$ (Figure 1, Table 1), chosen for its similarity to recent attempts in the literature.

Input	Size	Target	Size
Temperature [K]	60	Heating tendency, dT/dt [K/s]	60
Specific humidity [kg/kg]	60	Moistening tendency, dq/dt [kg/kg/s]	60
Surface pressure [Pa]	1	Net surface shortwave flux, NETSW [W/m ²]	1
Insolation [W/m ²]	1	Downward surface longwave flux, FLWDS [W/m ²]	1
Surface latent heat flux [W/m ²]	1	Snow rate, PRECSC [m/s]	1
Surface sensible heat flux [W/m ²]	1	Rain rate, PRECC [m/s]	1
		Visible direct solar flux, SOLS [W/m ²]	1
		Near-IR direct solar flux, SOLL [W/m ²]	1
		Visible diffused solar flux, SOLSD [W/m ²]	1
		Near-IR diffused solar flux, SOLLD [W/m ²]	1

Table 1: The subset of input and target variables used in most of our experiments (Figure 1). Dimension length 60 corresponds to the total number of vertical levels (discretized altitudes) of the climate simulator.

Training/Validation Split: We divide the 8-year training/validation set into the first 7 years (i.e., 0001-02 to 0008-01 in the raw filenames’ “year-month” notation) for training and the subsequent 1 year (0008-02 to 0009-01) for validation. This split was chosen somewhat arbitrarily, and we encourage users of this dataset to consider alternative splits. However, it is crucial to ensure that the validation period is separate from the training period by at least one month to avoid contamination due to temporal autocorrelation in the atmosphere.

Preprocessing Workflow: Our preprocessing steps were (1) downsample in time by using every 7th sample, (2) collapse horizontal location and time into a single sample dimension, (3) normalize variables by subtracting the mean and dividing by the range, with these statistics calculated separately at each of the 60 vertical levels for the four variables with vertical dependence, and (4) concatenate variables into multi-variate input and output vectors for each sample (Figure 1). The heating tendency target dT/dt (i.e., time rate of temperature T) was calculated from the raw climate simulator output as $(T_{after} - T_{before})/\Delta t$,

where Δt ($= 1200$ s) is the climate simulator’s known macro-scale timestep. Likewise, the moisture tendency was calculated via taking the difference of humidity state variables recorded before versus after the convection and radiation calculations. This target variable transformation (i.e., state to tendency) is done to compare our baseline models’ performance to that of previously published models that reported errors of emulated tendencies (Mooers et al., 2021; Behrens et al., 2022). Additionally, this transformation implicitly normalizes the target variables, leading to better convergence properties for ML algorithms. Given the domain-specific nature of the preprocessing workflow, we provide scripts in the GitHub repository for workflow reproduction.

4.1 Baseline Architectures

We evaluate seven baseline models, each chosen for their relevance to climate data emulation tasks. These include a Convolutional Neural Network (CNN), an Encoder-Decoder (ED) model, Heteroskedastic Regression (HSR), a Multi-layer Perceptron (MLP), a Randomized Prior Network (RPN), a Conditional Variational Autoencoder (cVAE), and a U-Net (UNET). The U-Net is an expansion from our original NeurIPS paper, for reasons that will become clear in Section 5. These models represent a diverse range of architectures, from fully connected networks to encoder-decoder structures and ensemble methods, enabling a comprehensive comparison of their emulation capabilities. Further details about each model’s architecture and implementation are provided in Appendix C.

Variable	MAE [W/m ²]							R ²						
	CNN	ED	HSR	MLP	RPN	cVAE	UNET	CNN	ED	HSR	MLP	RPN	cVAE	UNET
dT/dt	2.585	2.864	2.845	2.683	2.685	2.732	2.506	0.627	0.542	0.568	0.589	0.617	0.590	0.647
dq/dt	4.401	4.673	4.784	4.495	4.592	4.680	4.363	–	–	–	–	–	–	–
NETSW	18.85	14.968	19.82	13.36	18.88	19.73	12.34	0.944	0.980	0.959	0.983	0.968	0.957	0.985
FLWDS	8.598	6.894	6.267	5.224	6.018	6.588	4.623	0.828	0.802	0.904	0.924	0.912	0.883	0.939
PRECSC	3.364	3.046	3.511	2.684	3.328	3.322	2.441	–	–	–	–	–	–	–
PRECC	37.83	37.250	42.38	34.33	37.46	38.81	32.57	0.077	-17.909	-68.35	-38.69	-67.94	-0.926	-0.916
SOLS	10.83	8.554	11.31	7.971	10.36	10.94	7.330	0.927	0.960	0.929	0.961	0.943	0.929	0.967
SOLL	13.15	10.924	13.60	10.30	12.96	13.46	9.696	0.916	0.945	0.916	0.948	0.928	0.915	0.953
SOLSD	5.817	5.075	6.331	4.533	5.846	6.159	4.248	0.927	0.951	0.923	0.956	0.940	0.921	0.962
SOLLD	5.679	5.136	6.215	4.806	5.702	6.066	4.608	0.813	0.857	0.797	0.866	0.837	0.796	0.880

Table 2: MAE and R² for target variables averaged globally and temporally (from 0009-03 to 0011-02). Variables include heating tendency (dT/dt), moistening tendency (dq/dt), net surface shortwave flux (NETSW), downward surface longwave flux (FLWDS), snow rate (PRECSC), rain rate (PRECC), visible direct solar flux (SOLS), near-IR direct solar flux (SOLL), visible diffused solar flux (SOLSD), and near-IR diffused solar flux (SOLLD). Units of non-energy flux variables are converted to a common energy unit, W/m² (see Appendix E.2). Best model performance for each variable is bolded. For dq/dt and PRECSC, global mean R² is not an ideal evaluation metric and not reported due to negligible variability in dq/dt in the upper atmosphere and PRECSC in the tropics in the dataset.

4.2 Evaluation Metrics

Our evaluation metrics are computed separately for each variable in the output vector. The mean absolute error (MAE) and the coefficient of determination (R^2) are calculated independently at each horizontal and vertical location and then averaged horizontally and vertically to produce the summary statistics in Figure 2. For the vertically-varying fields, we first form a mass-weighting and then convert moistening and heating tendencies into common energy units in Watts per square meter as in Beucler et al. (2024). The details of unit conversion is documented in Appendix E.2. We also report continuous ranked probability scores (CRPS) for all considered models in Appendix D.2.

4.3 Baseline Model Results

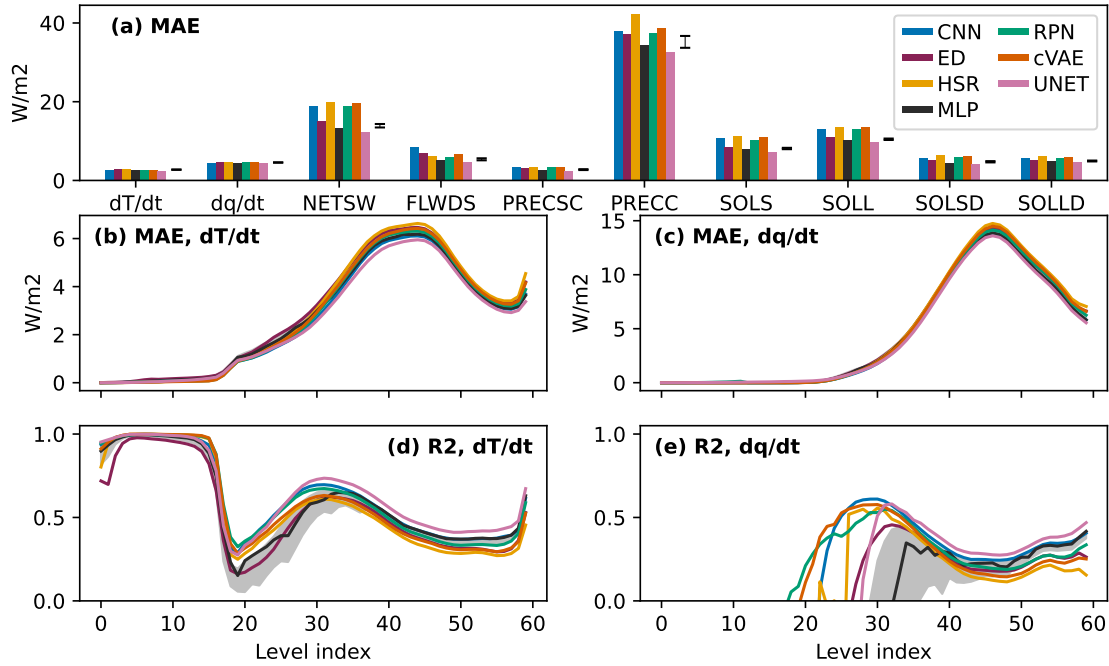


Figure 2: (a) Summary of the MAE scores of all baseline models for the target variables y , where dT/dt and dq/dt are the tendencies of temperature and specific humidity. (b,c) retain the vertical structure of MAE and (d,e) R^2 for dT/dt and dq/dt . Error bars and grey shadings show the 5- to 95-percentile range of MLP. Refer to Table 1 for variable definitions.

Figure 2 summarizes the error characteristics. Whereas heating and moistening rates have a common background vertical structure of global mean MAE (Figure 2 b,c), the coefficient of determination R^2 (d,e) reveals that certain architectures (RPN, HSR, cVAE, CNN) consistently perform better in the upper atmosphere (model level < 30) whereas the

U-Net and the highly optimized MLP model outperform in the lower atmosphere (model level > 30) and therefore the global mean (Table 2). For the global mean MAE and R^2 , the U-Net outperforms other baseline models nearly on all the target variables (Table 2). In terms of global mean R^2 , dT/dt and PRECC show the lowest values (< 0.7). Among them, U-Net achieves the highest R^2 for dT/dt, while CNN leads for PRECC. Other variables exhibit higher R^2 values (about 0.8 or above), suggesting they are easier to deep-learn (Table 2). For dq/dt and PRECSC global mean R^2 is not an ideal evaluation metric due to negligible variability in dq/dt in the upper atmosphere and for PRECSC in the tropics in the dataset (Table 2).

Figure 3 further illustrates the latitude-height spatial structure of R^2 . Heating and moistening tendencies show higher R^2 values in the middle-to-upper troposphere (200–600 hPa) in the lower latitudes. For heating tendency, U-Net performs the best in the lower latitudes, while HSR, RPN, and cVAE perform particularly well for heating tendencies in polar regions (poleward of 50°S and 50°N) above 500 hPa. For moistening tendency, negative R^2 values in polar regions and the stratosphere are likely due to minimal water vapor content and negligible dq/dt variability. Addressing these negative values may require more careful target normalization.

The fit quality can be further revealed in the joint distribution of prediction vs. simulation targets, such as for snow rate (PRECSC) and rain rate (PRECC) (Figure 4). Several architectures (CNN, HSR, RPN, and cVAE) show systematic underestimation of the strong rain and snow events that have a normalized value greater than 1. This suggests potential issues for using these models to simulate extreme precipitation events.

Additional tables and figures that reveal the geographic and vertical structure of errors, fit quality, and analysis of stochastic metrics are included in the appendices (Appendix D.2, Appendix D.3, and Appendix H).

4.4 Offline Skill Boost from Expanding Features and Targets

We performed an ablation of our best-performing MLP baseline to demonstrate the added value of the expanded inputs and targets available in ClimSim, i.e., using inputs x of size $d_i = 617$ and targets $y \in \mathbb{R}^{d_o}$ of size $d_o = 368$. The expanded input features include liquid and ice condensate mixing ratios, zonal and meridional winds, gas concentrations, and several scalars related to surface boundary conditions (see Table 4 in the Appendix for a complete variable list). We use the same transformation described in our preprocessing workflow to compute and add condensate (cloud liquid and cloud ice) and momentum (zonal and meridional winds) tendencies to the target vector. We conducted this ablation study with both the low-resolution and the high-resolution datasets (see Appendix C.1 for further details regarding these MLP variants). For common elements of the target vector, using all available variables leads to a uniform improvement in prediction accuracy, especially for precipitation, in both resolutions (Table 3 in the main text, and Figures 14 and 15 in the Appendix). The larger errors (e.g., MAE and RMSE) observed in the high-resolution emulators are anticipated due to the increased variance of higher-resolution data. Nevertheless, the similarity of their R^2 values to those of the corresponding low-resolution emulators confirms their adequate performance.

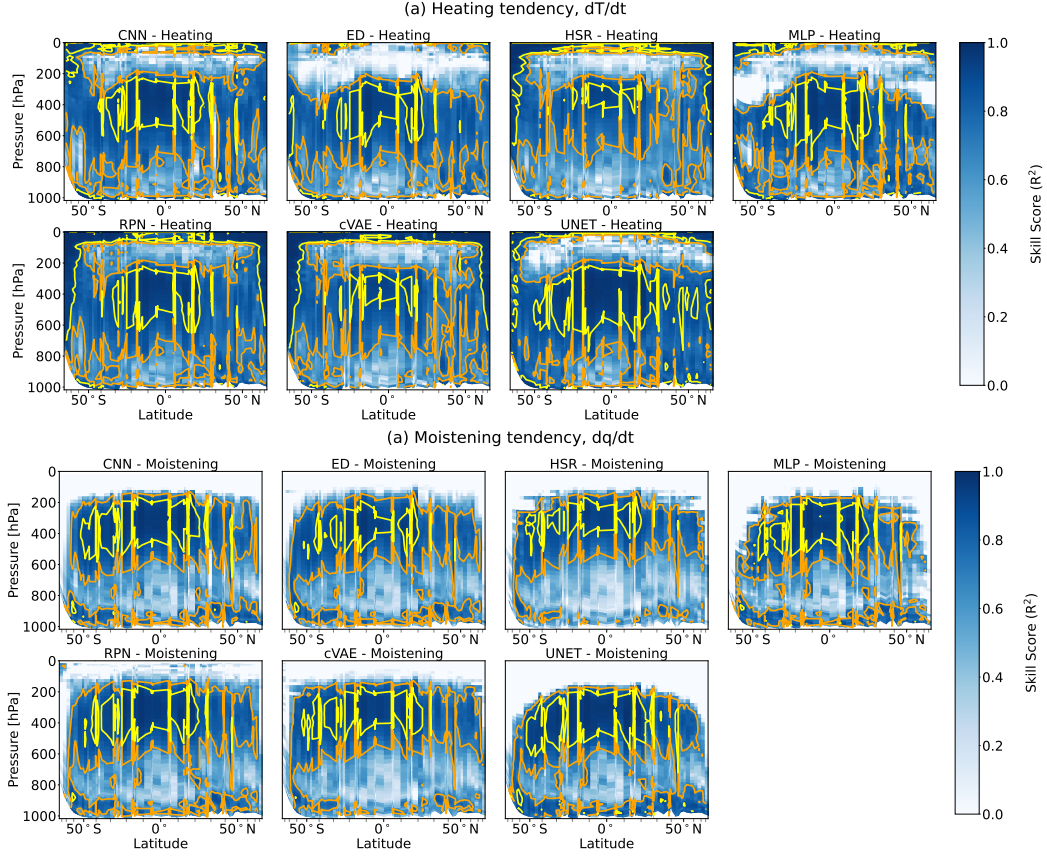


Figure 3: R^2 of daily-mean, zonal-mean (a) heating tendency and (b) moistening tendency. The original tendency data, structured as $(n_{\text{samples}}, n_{\text{col}}, n_{\text{lev}})$ —representing time samples, horizontal grid points, and vertical levels—were averaged by day and within each latitude band, resulting in arrays of shape $(n_{\text{days}}, n_{\text{lats}}, n_{\text{lev}})$, where n_{days} represents unique days, n_{lats} distinct latitude bands, and n_{lev} the vertical levels. R^2 was then calculated across the n_{days} dimension to quantify how well daily variations in heating and moistening tendencies are explained. Yellow contours surround regions of $R^2 > 0.9$ while orange contours surround regions of $R^2 > 0.7$. Larger spatial extents of these high- R^2 regions reflect better model performance. Negative values are not plotted (white). The x-axis uses the sine of latitude ($\sin(\text{latitude})$) instead of a linear scale, as $\Delta(\sin(\text{latitude}))$ corresponds to equal surface area across latitude bands. The y-axis represents approximate pressure values for the hybrid sigma-pressure vertical coordinate levels from the E3SM model.

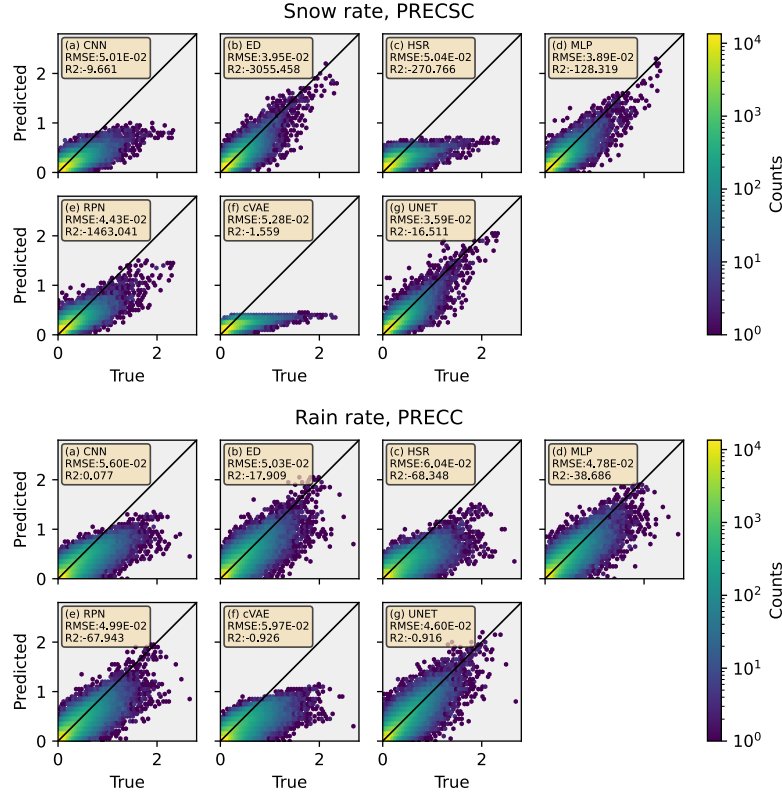


Figure 4: Hexagonally-binned representation of 2D target variables (snow rate and rain rate shown here, with additional variables shown in Appendix D.3) comparing the climate model simulation (“true”; x-axis) with the ML model prediction (“predicted”; y-axis). The color of each hexagonal bin corresponds to the number of data points enclosed.

5. ClimSim-Online: Hybrid Testing and Online Performance Evaluation

The primary objective of evaluating a machine learning model within hybrid climate simulations is to measure the online error (Rasp et al., 2018; Wang et al., 2022b; Kochkov et al., 2024; Sanford et al., 2023a). This error assesses how well the hybrid simulation, which integrates the ML model with the rest of the climate simulator, reproduces the statistics of the original high-fidelity climate simulation. Optimizing offline metrics does not necessarily lead to optimized online performance (Ott et al., 2020; Wang et al., 2022b), as small prediction errors at each time step can accumulate over year-long climate simulations (26,280 timesteps per simulated year). In this section, we describe how to integrate the ML model into the climate simulator and the process for evaluating the online performance of the hybrid physics-ML climate simulations. We also provide a case study from the recent work of Hu et al. (2025) illustrating progress in improving the online performance of the hybrid simulation. In this online task, the ML models predict the expanded targets $y \in \mathbb{R}^{d_o}$ of size $d_o = 368$, similar to baseline models with expanded features and target (Section 4.4) (tendencies of temperature,

	(Variables)	MLPv1	MLPv2	MLPv1-ne30	MLPv2-ne30
MAE	dT/dt	2.688	2.305	2.799	2.886
	dq/dt	4.503	4.030	4.231	4.068
	dq _l /dt	N/A	0.689	N/A	0.697
	dq _i /dt	N/A	0.384	N/A	0.330
	du/dt	N/A	1.34E-04	N/A	2.68E-04
	dv/dt	N/A	1.09E-04	N/A	2.66E-04
	NETSW	13.47	8.339	15.47	11.04
	FLWDS	5.118	4.134	5.318	4.891
	PRECSC	2.645	1.539	3.115	3.009
	PRECC	33.89	23.74	42.49	29.62
	SOLS	7.942	5.774	8.484	6.866
	SOLL	10.30	8.190	10.582	8.993
	SOLSD	4.587	3.230	5.056	4.360
	SOLLD	4.834	3.977	4.963	4.553
R2	dT/dt	0.590	0.663	0.626	0.536
	dq/dt	-	-	-	-
	dq _l /dt	N/A	-	N/A	-
	dq _i /dt	N/A	-	N/A	-
	du/dt	N/A	-	N/A	-
	dv/dt	N/A	-	N/A	-
	NETSW	0.982	0.993	0.977	0.988
	FLWDS	0.927	0.945	0.914	0.924
	PRECSC	-	-	-0.117	-0.117
	PRECC	-1.494	0.833	-0.115	-0.115
	SOLS	0.962	0.978	0.963	0.976
	SOLL	0.948	0.964	0.953	0.965
	SOLSD	0.955	0.976	0.950	0.965
	SOLLD	0.866	0.905	0.874	0.899
RMSE	dT/dt	4.437	3.756	5.199	4.958
	dq/dt	7.337	6.521	7.550	7.135
	dq _l /dt	N/A	1.192	N/A	1.489
	dq _i /dt	N/A	0.812	N/A	0.940
	du/dt	N/A	2.80E-04	N/A	6.45E-04
	dv/dt	N/A	2.25E-04	N/A	6.72E-04
	NETSW	26.95	17.24	30.48	21.18
	FLWDS	6.803	5.532	7.136	6.540
	PRECSC	4.656	2.955	7.791	7.509
	PRECC	73.16	53.47	119.8	83.22
	SOLS	17.39	12.84	18.51	14.74
	SOLL	21.96	17.89	22.71	19.27
	SOLSD	9.474	6.837	10.42	8.724
	SOLLD	10.14	8.486	10.62	9.526

Table 3: Similar to Table 2 but for comparing MAE, R2, and RMSE of different MLP models: MLP v1 (subset emulation) and the MLP v2 (full vector emulation) built with the low-resolution (ne4) and the high-resolution datasets (ne30). dq_l/dt, dq_i/dt, du/dt, and dv/dt correspond to the tendencies of state_q0002, state_q0003, state_u, and state_v, respectively, in Table 4 in the Appendix.

moisture, cloud water, cloud ice, zonal wind and meridional wind, in addition to precipitation and radiative fluxes at the surface; see supplementary Table 4 in the Appendix). These

expanded targets ensure that the ML model predicts all the necessary variables to update the atmospheric state and drive the rest of the climate simulator, thereby enabling complete coupling.

5.1 Software to Integrate ML Models into Physical Climate Simulations

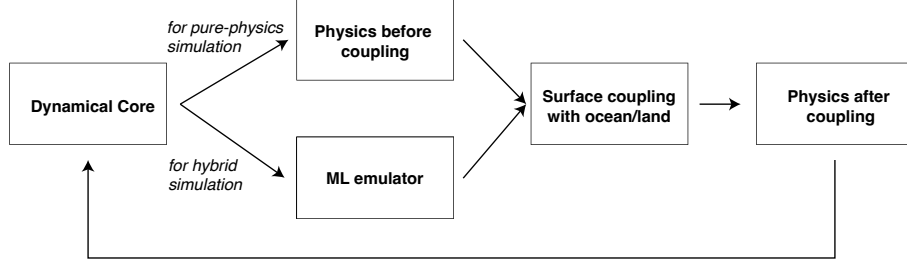


Figure 5: Schematic flowchart of E3SM-MMF climate simulator workflow. Each block represents a module executed during one model time step. In a standard reference pure-physics simulation, the physics-before-coupling module handles parameterization of subgrid processes (convection and radiation), involving the calculations of cloud-resolving simulators embedded in each atmosphere column. In a hybrid simulation, the "ML emulator" module replaces the physics-before-coupling module while computations in other modules remain unchanged. This figure is adapted from the Figure 3 in Wang et al. (2022b), which described the flowchart of a similar climate simulator.

Figure 5 illustrates the time-stepping workflow of the E3SM-MMF multi-scale climate simulator, highlighting how an ML emulator is integrated into its simulation pipeline. In the reference pure-physics simulation, the dynamical core solves large-scale atmospheric dynamics, capturing how advection modifies atmospheric fields, on planetary scales. The physics-before-coupling module calculates radiative transfer and employs cloud-resolving simulators within each atmospheric column to represent subgrid-scale processes, including storm dynamics, cloud formation, and their impacts on the atmosphere states. Next, the surface coupling module exchanges atmospheric states with the surface modules. Finally, the physics-after-coupling module parameterizes vertical diffusion and gravity wave drag effects on the atmospheric state.

In the hybrid physics-ML simulation, the ML emulator replaces the entire physics-before-coupling module, i.e. completely absorbing the computationally costly cloud-resolving calculations that dominate MMF expense, while the other modules remain unchanged. Below, we describe the key components enabling this integration: the PyTorch-Fortran coupling, the use of TorchScript, and a cross-platform containerized workflow.

Pytorch-Fortran Coupling: The original climate simulator, the E3SM-MMF multi-scale climate simulator (see Appendix A.2 for more details), is written in object-oriented, MPI-decomposed Fortran. To integrate a Python-based ML model into the climate simulator and replace the learned code subregion, we implemented a coupling workflow using an open-source library called Pytorch-Fortran (Alexeev, 2023). This library simplifies the integration of

PyTorch models with Fortran-based climate simulators and specifically supports TorchScript models. It provides straightforward interfaces for loading ML models, processing Fortran tensors in a zero-copy fashion, and performing efficient batch inference. An alternative open-source library with similar functionality is FTorch (Cambridge-ICCS, 2025), although it is not used in our current implementation.

TorchScript: To utilize the PyTorch-Fortran bindings, it is necessary to first serialize PyTorch models using TorchScript (PyTorch Contributors, 2024). TorchScript models can operate independently of Python and support flexible architecture design. Converting a PyTorch model into TorchScript is straightforward, as TorchScript is compatible with most PyTorch functions and many Python built-ins. Appendix F.1 provides detailed instructions on writing PyTorch models that can be converted into TorchScript. We also include example code for converting a PyTorch model into TorchScript. Although we use the TorchScript interface in PyTorch-Fortran for best performance, PyTorch-Fortran also supports spawning a Python interpreter and can run arbitrary Python code using other ML packages (e.g., JAX, scikit-learn, and TensorFlow), provided the input and output interface of the Python code is `torch.Tensor`.

Cross-Platform Containerized Hybrid Testing Workflow: Building flexible couplers to foster the progress from skillful ML parameterizations into skillful hybrid physics-ML climate simulators is vital for the ML and climate community. Unfortunately, the complexity and nuance involved in performing climate simulations has meant many wasted graduate student hours and a dearth of online error results in the hybrid simulation literature (Lin et al., 2023). We have implemented the first end-to-end containerized workflow for this purpose, enabling ML models to be integrated into our climate simulator for online testing. This container can be deployed on multiple platforms, including Linux-based laptops or workstations, high-performance computing (HPC) clusters, and cloud-based virtual machines. Once the container is set up, users can easily launch hybrid simulations by providing the trained ML model in TorchScript format and reproduce the results shown in Figure 6.

5.2 Metrics for Evaluating Online Errors in Hybrid Climate Simulations

The primary objective of evaluating hybrid climate simulations is to assess their ability to reproduce long-term climate statistics, such as temporally and spatially averaged atmospheric states. This requires a different validation approach than that needed for scoring short-term predictions of instantaneous atmospheric patterns, as in weather forecasting. In this section, we introduce two climatologically appropriate error metrics – root mean square error (RMSE) and zonal mean bias of the monthly mean – which serve as a minimal and preliminary evaluation of hybrid model performance. These metrics provide a quick and accessible overview for assessing the effectiveness of different modeling approaches.

However, it is important to note that many other detailed analyses—examining diverse aspects of hybrid simulations, such as seasonal and spatial variability, statistics of extreme events, and the diurnal cycle of rainfall—could be conducted to achieve a more comprehensive understanding of model behavior. Such in-depth analyses are explored in several existing studies on hybrid climate simulators (Kochkov et al., 2024; Hu et al., 2025; Han et al., 2023; Behrens et al., 2025; Sanford et al., 2023a; Yuval et al., 2021; Rasp et al., 2018). We also discuss more evaluation frameworks in Section 6.

Root Mean Square Error: To evaluate the online error growth within the first simulation year, we compute the root mean square error (RMSE) separately for each variable in the hybrid simulations. For a given month, the RMSE for each variable is calculated as follows:

$$\text{RMSE} = \sqrt{\sum_{i=1}^{S_m} w_i (\hat{y}_m - y_m)^2} \quad (1)$$

where:

- S_m is the number of samples (each horizontal grid cell at a given time is one sample) across the entire globe,
- \hat{y}_m represents the values from the hybrid simulation averaged over the entire month,
- y_m represents the values from the reference simulation averaged over the entire month,
- w_1, w_2, \dots, w_{S_m} are weights that sum to 1 and are proportional to the air mass in each grid cell.

Zonal Mean Bias: Additionally, for stable hybrid simulations where online errors remain controlled in time, we evaluate the multi-year (26,280 timesteps per year) zonal mean bias, which measures the average difference between the hybrid simulation and the reference simulation across key atmospheric variables, such as temperature, moisture, wind, and cloud liquid and ice water. The zonal mean bias is derived by comparing variables averaged over time and longitude.

5.3 Experiment Setup for Hybrid Online Testing

Here, we use the experiments and results from Hu et al. (2025) to illustrate the online evaluation process and highlight experiences and key factors for optimizing online performance. Following the offline experiments in Section 4, we compare two architectures, the MLP model and U-Net model (our best-performing offline model), using the same architecture structures as in the offline experiments.

Three configurations are employed for online testing: a baseline MLP model, a baseline U-Net model, and the best-performing U-Net model from Hu et al. (2025). The baseline MLP model and the baseline U-Net use the same expanded features described in Section 4.4, with one modification: specific humidity is replaced with relative humidity. This adjustment follows the recommendation from Beucler et al. (2024), which suggests that relative humidity remains more invariant across different climate states, potentially improving the ML emulator’s ability to generalize to unseen climate regimes.

The best-performing U-Net model from Hu et al. (2025), referred to as U-Net-expanded-constrained, incorporates additional input features, including temporal information from previous time steps and cloud physics constraints. These input features are derived from existing ClimSim data and are documented in detail in Appendix F.3.3. The cloud physics constraints are designed to prevent unrealistic cloud formation. For example, no ice-phase clouds are permitted when temperatures exceed 0°C , and no liquid-phase clouds are allowed for

conditions colder than -20°C . Additionally, Hu et al. (2025) imposed a constraint prohibiting ice-phase clouds in the stratosphere, an approximation that helps prevent unrealistic cloud accumulation in the stratosphere. Further details on the implementation of these cloud physics constraints can be found in Appendix F.3.4.

In training these MLP and U-Net models, Hu et al. (2025) adopted a modified input/output normalization strategy relative to the baseline ClimSim models described in Section 4. Specifically, they used a per-level standard deviation to normalize the targets, rather than applying a single scaling factor across all vertical levels for a given variable.

It is important to note that the ML models are trained on the low-resolution tier of the ClimSim data, and the hybrid simulations are conducted at consistent horizontal resolution. Conducting hybrid simulations at high resolution would require training the ML emulator on high-resolution data. Input features often exhibit systematic distribution shifts between low- and high-resolution data, and directly applying an ML emulator trained on low-resolution data to high-resolution simulations should be expected to lead to out-of-distribution issues.

To account for the variability in online performance not fully captured by offline skill, we tested three different checkpoints for each model. These checkpoints were obtained using varying loss functions and learning rate schedules, as different configurations were found to lead to differing online stability and error, even with similar offline performance (Lin et al., 2023).

Each checkpoint was used to run a one-year hybrid simulation. All hybrid simulations use the same initial conditions. We evaluated the monthly RMSE evolution throughout the year compared to the reference E3SM-MMF simulation. Additionally, to estimate the inherent unpredictability of the atmospheric system, we ran three additional pure physical simulations with the same initial conditions. These pure physical simulations were implemented using parallel reductions and atomic operations that prevent bitwise reproducibility (see Appendix F.3.5). The accumulation of these rounding errors over time can lead to variations in the climate simulator outcomes, mimicking the chaotic nature of the atmosphere. These simulations serve as a baseline for the atmospheric unpredictability. This recognizes that some chaotic interval variability exists even for monthly mean climatological statistics, albeit much less than on weather timescales.

For more details on model architectures, hyperparameters, input variables, and cloud physics constraints, please refer to Appendix F.3.

5.4 Results of Online Performance Testing

Figure 6 summarizes the online error for the one-year hybrid simulations along with the offline skill changes across our model choices. The hybrid simulations with the baseline MLP models were unstable, with all three instances crashing within the first two months of the simulations. In contrast, the more expressive U-Net architecture improved the R^2 score across all vertical levels and variables. This R^2 difference aligns with the findings from Section 4, despite differences in the input/output variable sets and normalization strategies used in this section.

This enhanced offline skill also translated to better online performance. The U-Net architecture allowed for more stable hybrid simulations, with all the U-Net simulations completing the full year. During the first month before the MLP simulations crashed, these

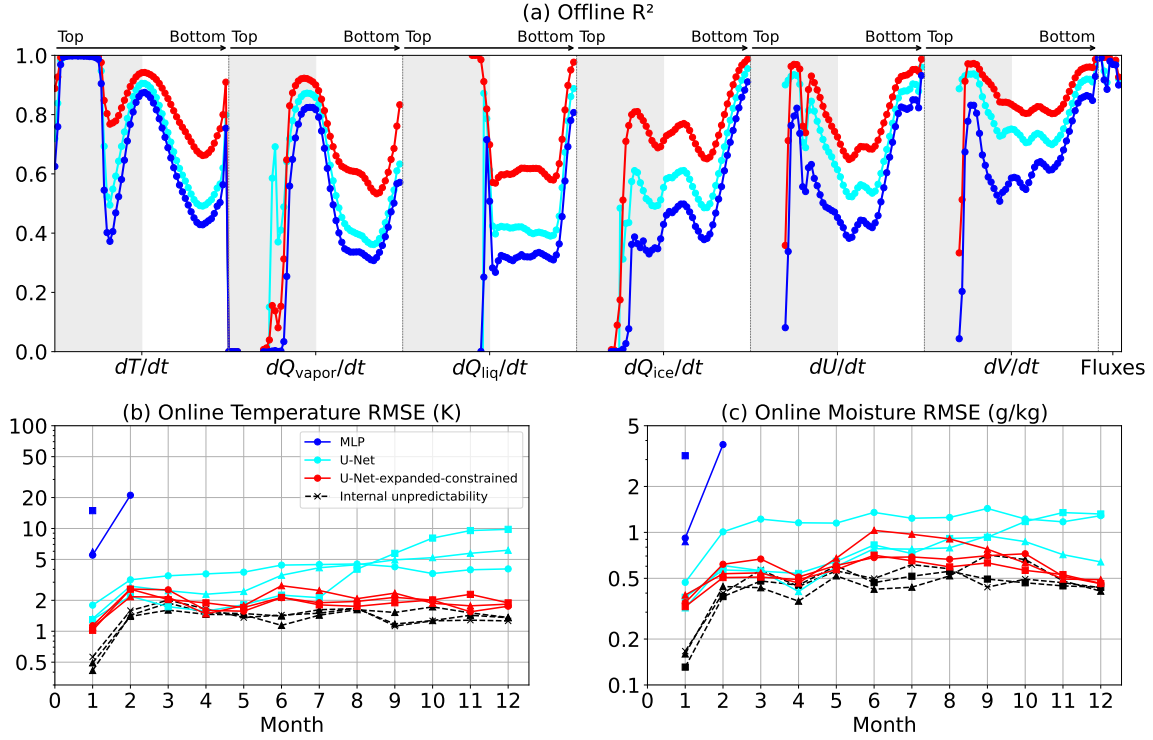


Figure 6: This Figure is adapted from Figures 3 and 5 from Hu et al. (2025). (a) Offline R^2 scores across various variables for MLP, U-Net, and U-Net-expanded-constrained models. Variables are the full target variables listed in Table 4 in the Appendix, including temperature tendency ($\frac{dT}{dt}$), water vapor tendency ($\frac{dQ_v}{dt}$), liquid cloud mixing ratio tendency ($\frac{dQ_c}{dt}$), ice cloud mixing ratio tendency ($\frac{dQ_i}{dt}$), zonal wind tendency ($\frac{dU}{dt}$), meridional wind tendency ($\frac{dV}{dt}$), and eight flux variables. (b,c) Online monthly and globally averaged (both horizontally and vertically and weighted by mass in each grid) RMSE of temperature (K) and moisture (g/kg) over a one-year period, comparing MLP, U-Net, and U-Net-expanded-constrained models against the reference E3SM-MMF simulation. Atmospheric unpredictability (black dashed lines) is estimated by running the reference E3SM-MMF simulations multiple times with the same initial condition while allowing for the chaotic growth of the random rounding errors.

U-Net simulations demonstrated significantly lower RMSE for climatological temperature and moisture compared to the hybrid simulations that used the MLP models.

Incorporating cloud physics constraints significantly improved stability and reduced error growth in the hybrid simulations. Without these constraints, the U-Net models developed increasing errors after a few months, leading to unrealistic cloud formations not represented in the training data, which potentially contributed to higher error growth (see Hu et al. (2025) for more details). The cloud physics constraints mitigated this issue by ensuring

clouds formed appropriately relative to temperature, such as preventing liquid clouds at very low temperatures where condensate should be frozen. With these constraints, the online RMSE stabilized after an initial rise within the first two months. The global temperature RMSE remained around 2K, and the global moisture RMSE stayed below 1 g/kg, during the entire span of the one-year simulations (red lines in Figure 6).

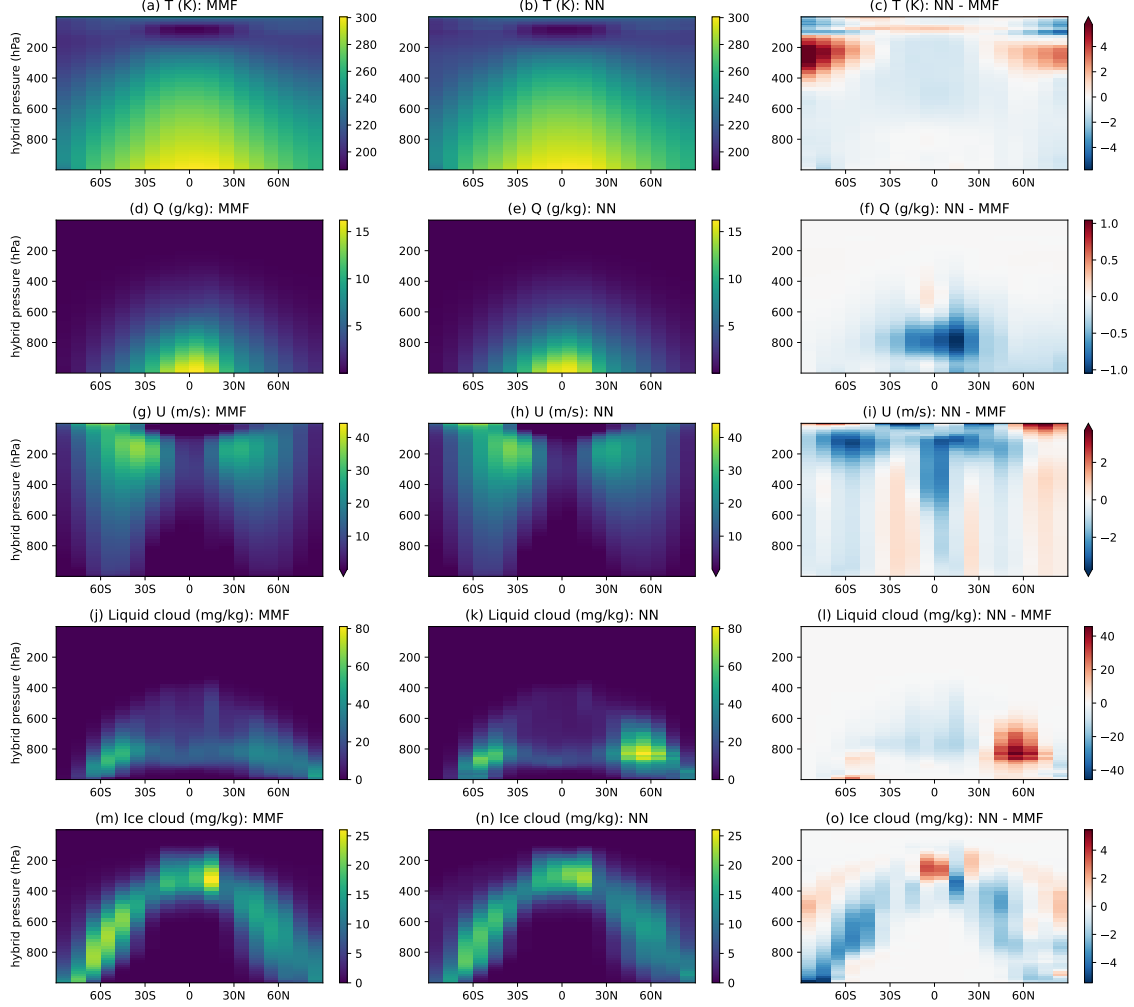


Figure 7: Five-year zonal mean atmospheric state in the reference E3SM-MMF simulation (left) and in the hybrid simulation (middle). The right column shows the zonal mean bias as the mean state from the hybrid simulation minus that of the reference simulation. The five rows show temperature, water vapor, zonal wind, liquid cloud, and ice cloud. This figure is a replication of Figure 9 in Hu et al. (2025).

Upon attaining online simulations that demonstrate stabilized error growth, it becomes meaningful to evaluate the multi-year statistical properties of the simulated climate. To

achieve this, we extended one of the U-Net-expanded-constrained models to a five-year simulation. At this temporal scale, the geographic patterns of the simulated climate become statistically robust, allowing us to analyze the pressure-latitude structure of the zonal mean bias in the five-year mean state. For comparison, we also ran a reference 5-year E3SM-MMF simulation with the same initial conditions. In the lower atmosphere, the zonal mean temperature bias was approximately within 2K, and the moisture bias was around 1 g/kg (Figure 7c and f). The zonal mean structures of wind and cloud distribution also compared favorably with the reference simulation.

While there is still room for improvement, these magnitudes outperform the previous benchmark results of Han et al. (2023) within the context of analogous multi-scale hybrid climate simulations, despite our having included the full complexity of interactive condensate coupling and inclusion of radiative transfer within the full-physics ML parameterization, which was sidestepped in that work. A caveat in this comparison is that the work of Han et al. (2023) used a higher resolution host climate simulator that has higher intrinsic variance, as well as a different software version for the multi-scale climate simulator.

Beyond the context of the multiscale modeling framework, other state-of-the-art hybrid physics-ML climate simulators include those by Kochkov et al. (2024) and Sanford et al. (2023a) demonstrate additional metrics of hybrid model performance. For example, Sanford et al. (2023a) reported a pattern RMSE of 1.2K for the annual mean temperature climatology at 200 hPa and 850 hPa and 2 mm for precipitable water compared to their reference dataset using a coarse-grained high-resolution global storm-resolving model. Sanford et al. (2023a) also showed an annual-mean zonal mean temperature bias below 1K over most of the troposphere and a zonal mean moisture bias within 0.8 g/kg. Kochkov et al. (2024) reported an annual-mean temperature RMSE of 0.61K at 850 hPa and 1.05K at 200 hPa, and an RMSE of 1.09 mm for annual precipitable water against their reference ERA5 dataset. It is also worth noting that such error metrics tend to be a function of climate simulator resolution and thus cannot be directly compared between these studies; the resolution in our hybrid model is approximately 10° , which is much lower than the 2° used by Sanford et al. (2023a) and the 1.4° used by Kochkov et al. (2024).

Further optimizing the remaining non-differentiable online bias is challenging and worthy of community effort. We discuss potential methods to optimize these online bias in Appendix F.4.

5.5 Physics-Informed Guidance to Improve Generalizability and Online Performance

We demonstrated in Section 5.4 that implementing cloud physics constraints can optimize online error and improve the stability of hybrid simulations.

Incorporating additional physics into the ML emulator could further improve the generalizability and online performance. Here we discuss some aspects of physics that are important to consider and examine, including the physical constraints, stochasticity and memory, and causal pruning. In Appendix E.3, we provide further discussion on the normalization strategy and other ML approaches that may be beneficial for generalizability and online performance.

Physical Constraints: Mass and energy conservation are important criteria for Earth system simulation. If these terms are not conserved, errors in estimating sea level rise or

temperature change over time may become as large as the signals we hope to measure. Enforcing conservation on the learned quantities helps constrain results to be physically plausible and reduce the potential for errors accumulating over long time scales. Appendix E.1 discusses how we can evaluate approximate water conservation. However, the current ClimSim dataset omits a few variables required to evaluate the exact conservation of water or energy. Future versions of the ClimSim dataset from E3SM-MMF with augmented output could address this limitation, allowing for precise conservation evaluation. We discuss how to implement a range of approximate conservation and cloud physics constraints, as well as enforce additional constraints, such as non-negativity for precipitation, condensate, and moisture variables, in Appendix E.1.

Stochasticity and Memory: The goal of the emulation task is to replace cloud-resolving simulators embedded within each atmospheric column using a machine learning model. These cloud-resolving simulators operate within their own high-resolution nested domains, but only the horizontally averaged outputs from these domains are synchronized with the coarser grid of the host E3SM simulator. As a result, the ClimSim dataset captures only the averaged information, omitting finer details of the internal cloud structures and convective processes within the nested domain. This loss of fine-scale spatial information inherently limits the ability of an ML model to make perfect deterministic predictions. To address this challenge, stochastic architectures—such as our RPN, HSR, and cVAE baselines—are particularly valuable, as they can account for the inherent uncertainty arising from unresolved internal variability.

An alternative strategy to partially compensate for this missing fine-scale information is to incorporate temporal information into the ML model (Kuang, 2024). By including features or targets from previous time steps in the input vector, the model can capture aspects of convection memory and exploit temporal autocorrelation that are naturally present in atmospheric data. This approach has been explored in previous studies (Han et al., 2020, 2023; Behrens et al., 2025; Lin et al., 2023; Hu et al., 2025) and has been integrated into our model for online testing. However, the effectiveness of this strategy in reducing online errors and enhancing hybrid stability remains an area for further investigation.

Causal Pruning: A systematic and quantitative pruning of the input vector based on objectively assessed causal relationships to subsets of the target vector has been proposed as an attractive preprocessing strategy, as it helps remove spurious correlations due to confounding variables and optimize the ML algorithm (Iglesias-Suarez et al., 2023; Kühbacher et al., 2024).

6. Limitations and Other Applications

This section discusses the limitations of the ClimSim-Online framework, open questions, and potential future extensions.

Idealizations: A limitation of the multi-scale climate simulator used to produce ClimSim (E3SM-MMF) is that it assumes scale separation, i.e., that convection can be represented as laterally periodic within the grid size of the host simulator, and neglects subgrid-scale representations of topographic and land-surface variability. The configuration of the multi-scale climate simulator used to make ClimSim also has no atmosphere-ocean coupling and ignores the radiative effects of aerosols. These are essential for simulating important climate

phenomena like El Niño and the influence of aerosols on cloud properties, which are critical for realistic future climate projections. Despite these simplifications, the data adequately capture many historically challenging aspects of the ML parameterization problem, such as stochasticity, and complex nonlinear interactions across radiation, microphysics, and turbulence.

Hybrid testing: To maximize simplicity and scalability, our containerized pipeline for evaluating hybrid error uses a very low resolution hybrid climate simulation that can run on just a single cloud compute node and even a personal laptop, and our evaluation protocol contains only minimum viable integrative statistics of hybrid climate simulation errors. As methods to reliably achieve hybrid skill mature, this pipeline should be expanded. First, in its computational ambition, towards multi-node cloud-compatible configurations compatible with a full-resolution hybrid simulation. Second, to more fully evaluate a resulting historical simulation or a simulation under Atmospheric Modelling Intercomparison Project conditions (AMIP, Gates et al., 1999) with a hybrid model with Earth observations. Testing large ensembles launched from multiple initial conditions as in Kochkov et al. (2024) would be beneficial. Implementing diagnostics of the tendencies predicted by the ML versus physics model, while each is alternately coupled to the host dynamics, would be strategic as was found useful for making progress on microphysics ML parameterization in Perkins et al. (2024). Finally, as hybrid simulators stabilize and begin to produce reasonable time-mean climate statistics, their variability behind the mean state becomes important to validate, such as by measuring intrinsic cyclogenesis frequency (Kochkov et al., 2024). Community-developed open-source diagnostic tools such as the Earth System Model Evaluation Tool (Eyring et al., 2020) and the Model Diagnostics Task Force Framework (Neelin et al., 2023) facilitate the evaluation of climate simulations compared to observations and traditional climate simulators.

Stochasticity: One open problem that the dataset may allow assessing is understanding the role of stochasticity in hybrid-ML simulation. While primarily used as a dataset for regression it would be also interesting to assess and understand the degree to which different variables are better modeled as stochastic or deterministic, or if the dataset gives rise to heavy-tailed or even multi-modal conditional distributions that are important to capture. To date, these questions have been raised based on physical conjectures (e.g., Lin and Neelin, 2003) but remain to be addressed in the ML-based parameterization literature. For instance, precipitation distributions have long tails that are projected to lengthen under global climate change (O’Gorman, 2015; Neelin et al., 2022)—and will thus tend to generate out-of-distribution extremes. ClimSim could help construct optimal architectures to capture precipitation tails and other impactful climate variables such as surface temperature, and could be easily extended to a distributional regression benchmark.

Interpretability: This dataset could also be utilized to discover physically interpretable models for atmospheric convection, radiation, boundary layer turbulence, and microphysics. A possible workflow would apply dimensionality reduction techniques to identify dominant predictors and vertical variations, followed by symbolic regression to recover analytic expressions (Zanna and Bolton, 2020; Grundner et al., 2023).

Generalizability: Although the impacts of global climate change and inter-annual variability are absent in this initial version of ClimSim, important questions surrounding climate-convection interactions can begin to be addressed. One strategy would involve partitioning the data such that the emulator is trained on cold columns, but validated on

warm columns, where warmth could be measured by surface temperatures, as in Beucler et al. (2024). However, the results from this approach may also reflect the dependence of convection on the geographical distribution of surface temperatures in the current climate and should be interpreted with caution. To optimally engage ML researchers in solving the climate generalization problem, a multi-climate extension of ClimSim should be developed that includes physical simulations that samples future climate states and more internal variability (Clark et al., 2022b; Bhouri et al., 2023b).

7. Conclusion

We introduce ClimSim-Online, the most physically comprehensive dataset and framework yet published for training and testing ML-based parameterizations of atmospheric storms, clouds, turbulence, rainfall, and radiation for use in hybrid-ML climate simulations. It contains all inputs and outputs necessary for online coupling in a full-complexity multi-scale climate simulator. We conduct a series of experiments on a subset of these variables that demonstrate the degree to which climate data scientists have been able to fit the deterministic and stochastic components in the dataset.

In this extension of our original NeurIPS benchmark, we have introduced a containerized pipeline to integrate ML models into climate simulators, and demonstrated the procedure for how to evaluate online performance in hybrid-ML climate model simulations. This containerized approach ensures reproducibility and accessibility, making it user-friendly for ML researchers without domain expertise. Unlike typical climate simulations, ClimSim-Online is compatible with commonly available cloud and local computing environments.

We also provide a hybrid-ML baseline model to showcase one example of improving the hybrid stability and online error, along with initial metrics for assessing its climatological performance. This demonstrates how ClimSim-Online can be an operational pipeline to explore the capabilities of novel models from the ML community in climate science.

We hope ML community engagement in ClimSim and ClimSim-Online will advance fundamental ML methodology and clarify the path to producing increasingly skillful subgrid-scale physics parameterizations that can be reliably used for operational climate simulation (Eyring et al., 2024b). To facilitate two-way communication between ML practitioners and climate scientists, we incorporate many desired characteristics for an ideal benchmark dataset suggested in Ebert-Uphoff et al. (2017) and Dueben et al. (2022). Such interdisciplinary collaboration will open up an exciting future in which the computational limits that currently constrain climate simulation can be reconsidered. We are already encouraged by several thousand global participants in a Kaggle ML competition based on the ClimSim that has attracted users from diverse domains and fostered innovation in the offline problem Lin et al. (2024). We are especially excited to see the benefits of such ML research at scale on the downstream hybrid simulation problem that ClimSim-Online makes accessible.

We hope the lessons learned from our focus on multi-scale atmospheric simulations will have applicability in other sub-fields of Earth System Science, where computational constraints currently hinder explicit representations of more complex systems.

Acknowledgments

This work is broadly supported across countries and agencies. Primary support is by NVIDIA, the National Science Foundation (NSF) Science and Technology Center (STC) Learning the Earth with Artificial Intelligence and Physics (LEAP; Award # 2019625-STC), and the Exascale Computing Project (17-SC-20-SC), a collaborative effort of the U.S. Department of Energy (DOE) Office of Science (SC), the National Nuclear Security Administration, and the Energy Exascale Earth System Model project, funded by DOE grant DE-SC0022331. M.S.P, S.Y., L.P., A.M.J., J.L., N.L., and G.M. further acknowledge support from the DOE (DE-SC0023368) and NSF (AGS-1912134). R.Y, S.M, P.G, M.P. acknowledge funding from the DOE Advanced Scientific Computing Research (ASCR) program (DE-SC0022255). C.B. acknowledges the Paul G. Allen Family Foundation’s funding of AI2. V.E., P.G., H.H., G.B., and F.I.-S. acknowledge funding from the European Research Council Synergy Grant (Agreement No. 855187) under the Horizon 2020 Research and Innovation Programme. E.A.B. was supported, in part, by NSF grant AGS-2210068. S.J. acknowledges funding from DOE ASRC under an Amalie Emmy Noether Fellowship Award in Applied Mathematics (B&R #KJ0401010). M.A.B acknowledges NSF funding from an AGS-PRF Fellowship Award (AGS-2218197). R.G. acknowledges funding from the NSF (DGE-2125913) and the U.S. Department of Defense (DOD). S.M. acknowledges support from an NSF CAREER Award and NSF grant IIS-2007719. P.-L. M. acknowledges support from the Enabling Aerosol–cloud interactions at GLobal convection-permitting scales (EAGLES) project (No. 74358) sponsored by DOE SC, Office of Biological and Environmental Research (BER), Earth System Model Development (ESMD) program area. L.Z. and N.L. received M²LInES research funding by the generosity of Eric and Wendy Schmidt by recommendation of the Schmidt Futures program. This research used resources of the National Energy Research Scientific Computing Center (NERSC), a DOE SC User Facility operated under Contract No. DE-AC02-05CH11231. The Pacific Northwest National Laboratory is operated by Battelle for the DOE under Contract DE-AC05-76RL01830. This work was performed under the auspices of the DOE by Lawrence Livermore National Laboratory under Contract DE-AC52-07NA27344. This work used Bridges2 at the Pittsburgh Supercomputing Center through allocation ATM190002 from the Advanced Cyberinfrastructure Coordination Ecosystem: Services & Support (ACCESS) program, which is supported by NSF grants #2138259, #2138286, #2138307, #2137603, and #2138296. This work also utilized the DOD High Performance Computing Modernization Program (HPCMP). We recognize the contributions of Anima Anandkumar, David C Bader, Peter Caldwell, Nicholas Geneva, Yilun Han, Karthik Kashinath, Marat Khairoutdinov, Thorsten Kurth, Griffin Mooers, Jaideep Pathak, David Randall, Mark A Taylor, and Carl Vondrick to the earlier work that formed the basis of this updated manuscript.

ClimSim-Online: Appendix

Contents

A	Climate Simulations	28
A.1	Concepts and Terminology from Earth Science	28
A.2	Model Description	29
A.3	Model Configurations	31
B	Dataset and Code Access	31
B.1	Code Access	31
B.2	Variable List	32
B.3	Dataset Statistics	32
B.4	Dataset Applications	32
B.5	Target Audiences	34
C	Baseline Models	34
C.1	Multilayer Perceptron (MLP)	34
C.2	Randomized Prior Network (RPN)	37
C.3	Convolutional Neural Network (CNN)	37
C.4	Heteroskedastic Regression (HSR)	38
C.5	Conditional Variational Autoencoder (cVAE)	40
C.6	Encoder-Decoder (ED)	41
C.7	U-Net (UNET)	42
C.8	Inference Cost	42
D	Baseline Model Evaluations	43
D.1	Metrics	43
D.1.1	Deterministic Metrics	43
D.1.2	Stochastic Metric (CRPS)	43
D.2	Results	44
D.3	Fit Quality	44
E	Guidance	44
E.1	Physical Constraints	44
E.2	Unit Conversion and Weighting for Interpretable Evaluation	48
E.3	Additional Guidance	49
F	Online Evaluation Pipeline and Experiment Details	50
F.1	Converting PyTorch Models to TorchScript	50
F.2	Metrics for Evaluating Hybrid Climate Simulators	51
F.3	Experiment Setup for Online Testing	52
F.3.1	Multilayer Perceptron (MLP)	52

F.3.2	U-Net	52
F.3.3	Additional Inputs for the U-Net-expanded-constrained Model	52
F.3.4	Implementing Cloud Physics Constraints	53
F.3.5	Sources of Online Uncertainty in Hybrid Simulations	54
F.4	Challenges and Future Directions in Online Error Optimization	56
G	Other Related Work	56
H	Extra Figures and Tables	58
H.1	MLP with Expanded Target Variables	58
H.2	Scatter Plots	60
H.3	Global Maps of R^2	67
I	Datasheet	71

Appendix A. Climate Simulations

Climate models divide the Earth’s atmosphere, land surface, and ocean into a 3D grid, creating a discretized representation of the planet. Somewhat like a virtual Lego construction of Earth, with each brick representing a small region (grid cell). Earth system models are made up of independent component models for the atmosphere, land surface, rivers, ocean, sea ice, and glaciers. Each of these component models is developed independently and can run by itself when provided with the appropriate input data. When running as a fully coupled system the “component coupler” handles the flow of data between the components.

Within each grid cell of the component models, a series of complex calculations are performed to account for various physical processes, such as phase changes of water, radiative heat transfer, and dynamic transport (referred to as “advection”). Each component model uses the discretized values of many quantities (such as temperature, humidity, and wind speed) as inputs to parameterizations and fluid solvers to output those same values for a future point in time.

The atmosphere and ocean components are the most expensive pieces of an Earth system model, which is largely due to the computation and inter-process communication associated with their fluid dynamics solvers. Furthermore, a significant portion of the overall cost is attributed to the atmospheric physics calculations that are performed locally within each grid column. It is important to note that atmospheric physics serves as a major source of uncertainty in climate projections, primarily stemming from the challenges associated with accurately representing cloud and aerosol processes.

A.1 Concepts and Terminology from Earth Science

Convection Parameterization: In atmospheric science, “convection” refers to storm cloud and rain development, as well as the associated small-scale (100s m to <10km) turbulent air motions. Convective parameterizations represent the integrated effects of these processes, such as the vertical transport of heat, moisture, and momentum within the atmosphere, and condensational heating and drying, on the temporal and spatial scale of the host climate simulator (Emanuel, 1994; Randall, 2012; Siebesma et al., 2020). Stochastic parameterizations

represent sub-resolution (“subgrid-scale” in the terminology of Earth science) effects as stochastic processes, dependent on grid-scale variable inputs (Lin and Neelin, 2000; Neelin et al., 2008) to capture variations arising from subgrid-scale dynamics.

Multi-Scale Climate Simulators: Multi-scale climate simulation is a technique that represents convection without a convective parameterization by deploying a smaller-scale, high-resolution cloud-resolving simulator nested within each host grid column of a climate simulator (Grabowski and Smolarkiewicz, 1999; Benedict and Randall, 2009; Randall, 2013; Hannah et al., 2020; Norman et al., 2022). The smaller-scale simulator explicitly resolves the detailed behavior of clouds and their turbulent motions at both a higher spatial and temporal resolution than the host simulator. This improves the accuracy of the host simulations but comes at a high computational cost (Randall et al., 2003; Khairoutdinov et al., 2008). The time-integrated and horizontally averaged influence of the resolved convection is fed upscale to the host climate simulator and is the target of hybrid-ML climate simulation approaches.

Significance of Precipitation Processes for Climate Impacts: In climate simulations, changes in precipitation with climate change are a particularly important issue. The frequency of extreme precipitation events increases with climate change (Pall et al., 2007; Guerreiro et al., 2018; Neelin et al., 2022; Seneviratne et al., 2021; Mooers et al., 2022), with corresponding societal impacts (Davenport et al., 2021). Current climate simulators agree on the direction of this change but exhibit a large spread in the quantitative rate of increase with climate change (Pendergrass and Hartmann, 2014; Martinez-Villalobos and Neelin, 2023; Seneviratne et al., 2021).

A.2 Model Description

The data that comprise ClimSim are from simulations with the Energy Exascale Earth System Model-Multiscale Modeling Framework version 2.1.0 (E3SM-MMF v2) (E3SM Project, 2023). Traditionally, global atmospheric models parameterize clouds and turbulence using crude, low-order models that attempt to represent the aggregate effects of these processes on larger scales. However, the complexity and nonlinearity of cloud and rainfall processes make them particularly challenging to represent accurately with parameterizations. The MMF approach replaces these conventional parameterizations with a cloud resolving model (CRM) in each cell of the global grid, so that cloud and turbulence can be explicitly represented. Each of these independent CRMs is spatially fixed and exchange coupling tendencies with a parent global grid column. This novel approach to representing clouds and turbulence can improve various aspects of the simulated climate, such as rainfall patterns (Kooperman et al., 2016).

The configuration of E3SM-MMF used here shares some details with E3SMv2. The dynamical code of E3SM uses a spectral element approach on a cubed-sphere geometry. Physics calculations are performed on an unstructured, finite-volume grid that is slightly coarser than the dynamics grid, following Hannah et al. (2021), which is better aligned with the effective resolution of the dynamics grid. Cases with realistic topography include an active land model component that responds to atmospheric conditions with the appropriate fluxes of heat and momentum.

The embedded CRM in E3SM-MMF is adapted from the System for Atmospheric Modeling (SAM) described by Khairoutdinov and Randall (2003). While the CRM does explicitly represent clouds and turbulence, it still cannot represent the smallest scales of turbulence

and microphysics, and, therefore, these processes still need to be parameterized within each CRM grid cell. Microphysical processes are parameterized with a single-moment scheme, and subgrid-scale turbulent fluxes are parameterized using a diagnostic Smagorinsky-type closure. Convective momentum transport in the nested CRM is handled using the scalar momentum tracer approach of Tulich (2015). The CRM uses an internal timestep of 10 seconds, while the global calculations use a timestep of 20 minutes.

Despite recent efforts to accelerate E3SM-MMF with GPUs and algorithmic techniques (Norman et al., 2022), the CRM domain size strongly affects the computational throughput and limits the type of experiments that can be conducted. However, the MMF approach is quite flexible in how the CRM size is specified. E3SM-MMF is typically run with a 2D CRM that neglects one of the horizontal dimensions, and employs relatively coarse grid spacing that cannot represent small clouds. Increasing the size of this 2D domain by adding further columns (more CRM cells) generally improves the realism of the model solution. Reducing the model grid spacing can also improve the model to a certain degree, although the number of columns often needs to be increased to avoid the degradation associated with a small CRM. Ideally, the CRM would always be used in a 3D configuration to fully capture the complex, chaotic turbulence that dictates the life cycle of each individual cloud, but this approach is generally limited to special experiments that can justify the extra computational cost. The simulations for ClimSim utilize a 2D CRM with 64 columns and 2 km horizontal grid spacing within each grid cell.

The atmospheric component of E3SM uses a hybrid vertical grid that is “terrain-following” near the surface, and transitions to be equivalent to pressure levels near the top (e.g., <https://www2.cesm.ucar.edu/models/atm-cam/docs/usersguide/node25.html>). The vertical levels are specified to be thin near the surface to help capture turbulent boundary layer processes, and are gradually stretched to be very coarse in the stratosphere. E3SM-MMF uses 60 levels for the global dynamics with a top level around 65 km. The CRM used for atmospheric physics uses 50 levels, ignoring the upper 10 levels, to avoid problems that arise from using the anelastic approximation with very low densities. This does not create any issues, because cloud processes are generally confined to the troposphere where the anelastic approach is valid. The hybrid grid can be converted to pressure levels using Equation 2, where $P_0 = 100,000$ Pa is a reference pressure, and $P_s(\mathbf{x}, t)$ is the surface pressure which varies in location \mathbf{x} and time t :

$$P_k = A_k P_0 + B_k P_s \quad (2)$$

A_k and B_k —where the subscript k denotes the index of vertical coordinate—are the fixed, prescribed coefficients that define how the “terrain-following” and “pure pressure” coordinates are blended to define the hybrid coordinate at each vertical level. A_k and B_k are provided as a part of the dataset with variable names of `hyam` and `hyai` or `hybm` and `hybi`, depending on whether mid-level or interface values are needed. The third character of the variable names (“a” and “b”) in Equation 2 denotes A_k and B_k coefficients, respectively. Note that the indexing of the vertical coordinate starts from the top of the atmosphere due to the construct of A_k and B_k coefficients, e.g., $k = 0$ for the top and $k = 59$ for the surface in E3SM-MMF.

In the E3SM-MMF framework, the sequencing of atmospheric processes can be conceptualized as follows. It starts with a surface coupling step that receives fluxes from the surface component models (i.e., land, ocean, and sea ice). This is followed by a set of relatively

inexpensive physics parameterizations that handle processes such as airplane emissions, boundary layer mixing, and unresolved gravity waves. The global dynamics then takes over to evolve the winds and advect tracers on the global grid. Finally, there is another set of physics calculations to handle clouds, chemistry, and radiation, which are relatively expensive. This final physics section is where the embedded CRM of E3SM-MMF is used, and is the ideal target for surrogate model emulation due to its outsized computational expense. Accordingly, this step represents the target of ClimSim.

One area where E3SM-MMF significantly differs from E3SMv2 is in the treatment of aerosols and chemistry. The embedded CRM in E3SM-MMF predicts the mass of water species (i.e., cloud and rain droplet mass mixing ratios) but does not predict the number concentration (i.e., number of drops per mass of air). One consequence of this limitation is that E3SM-MMF cannot represent complex cloud aerosol interactions that can impact droplet number concentrations and cloud radiative feedbacks. Therefore, E3SM-MMF cannot use the more sophisticated aerosol and chemistry package used by E3SMv2, and instead uses prescribed aerosol and ozone amounts to account for the direct radiative impact of these tracers. Current efforts are addressing this limitation for future versions of E3SM-MMF.

A.3 Model Configurations

The simulations used for ClimSim were performed on the NERSC Perlmutter machine. E3SM-MMF is unique among climate models in that it can leverage hybrid CPU/GPU architectures on machines such as NERSC Perlmutter (<https://www.nersc.gov/systems/perlmutter>), which has 4 NVIDIA A100 GPUs per node. All simulations were configured to run with 4 MPI ranks and 16 OpenMP threads per node. The low-resolution (real geography and aquaplanet) cases used 2 nodes, and the high-resolution (real geography) case used 32 nodes. The throughput of these configurations was roughly 11.5 simulated years per day (sypd) for low-resolution cases and 3.3 sypd for the high-resolution case, averaged over multiple batch submissions. The total simulation length in all cases was 10 model years and 2 model months.

Boundary conditions over maritime regions are constrained by prescribed sea surface temperatures and sea ice amount. Various input data are needed for the cases with realistic topography, such as ozone concentrations and sea surface temperatures, which have been generated to reflect a climatological average of the 2005-2014 period. The aquaplanet configuration does not have a land component, but otherwise has similar input requirements using idealized data to produce a climate that is symmetric along lines of constant latitude.

Appendix B. Dataset and Code Access

B.1 Code Access

Following NeurIPS Dataset and Benchmark Track guidelines, we have uploaded our datasets to Hugging Face:

- E3SM-MMF High-Resolution Real Geography dataset:
https://huggingface.co/datasets/LEAP/ClimSim_high-res

- E3SM-MMF Low-Resolution Real Geography dataset:
https://huggingface.co/datasets/LEAP/ClimSim_low-res
- E3SM-MMF Low-Resolution Aquaplanet dataset:
https://huggingface.co/datasets/LEAP/ClimSim_low-res_aqua-planet

For the Low-Resolution Real Geography dataset, we also updated an expanded version that contains additional features (see Appendix F.3.3 for more details) that can be retrieved from the original dataset and are explored in a recent study (Hu et al., 2025):

- E3SM-MMF Low-Resolution Real Geography dataset (expanded):
https://huggingface.co/datasets/LEAP/ClimSim_low-res-expanded

We have documented all code (including the code to preprocess the data, create, train, and evaluate the baseline models, and visualize data and metrics) in an openly available GitHub repository: <https://leap-stc.github.io/ClimSim>. The containerized workflow of running hybrid simulations can be found at <https://github.com/leap-stc/climsim-online/>.

B.2 Variable List

All variables included in our dataset are listed in Table 4.

B.3 Dataset Statistics

Here, we present some distribution statistics to aid in understanding the dataset. Detailed distributions for all variables are provided in https://github.com/leap-stc/ClimSim/tree/main/dataset_statistics. These statistics are calculated for each vertical level individually for the vertically-resolved variables (e.g., `state_t` and `state_q0001`). For each variable (additionally, at each level for the vertically-resolved variables), a histogram is provided to visualize the distribution using 100 bins. Additionally, a text file accompanies each histogram, containing key statistical measures such as the mean, standard deviation, skewness, kurtosis, median, deciles, quartiles, minimum, maximum, and mode. The text file also includes the bin edges and the corresponding frequency values used to generate the histogram figures. This comprehensive approach allows for a detailed analysis of the dataset’s distributions.

B.4 Dataset Applications

Our data can benefit a broader audience beyond climate modelers wishing to explore ML for subgrid parameterization. For climate studies, while high-frequency timestep-level outputs from simulations are rarely archived, they offer insights into convective extremes and diurnal variability. Such data opens the path to explore multi-scale interactions between rapid dynamics and broader weather and climate fluctuations. This includes a detailed examination of variables needed to constrain vertically resolved energy and water budgets and understand their variability. For the machine learning community, this dataset addresses the scarcity of large-scale regression benchmarks, common in the sciences. Such benchmarks are less common compared to prevalent industrial datasets that emphasize classification, computer vision, and NLP tasks.

In	Out	Variable	Dimensions	Units	Description
×		pbuf_SOLIN	ncol	W/m ²	Solar insolation
×		pbuf_COSZRS	ncol		Cosine of solar zenith angle
×		pbuf_LHFLX	ncol	W/m ²	Surface latent heat flux
×		pbuf_SHFLX	ncol	W/m ²	Surface sensible heat flux
×		pbuf_TAUZ	ncol	W/m ²	Zonal surface stress
×		pbuf_TAUY	ncol	W/m ²	Meridional surface stress
×		pbuf_ozone	lev, ncol	mol/mol	Ozone volume mixing ratio
×		pbuf_N2O	lev, ncol	mol/mol	Nitrous oxide volume mixing ratio
×		pbuf_CH4	lev, ncol	mol/mol	Methane volume mixing ratio
×		state_ps	ncol	Pa	Surface pressure
×	×	state_q0001	lev, ncol	kg/kg	Specific humidity
×	×	state_q0002	lev, ncol	kg/kg	Cloud liquid mixing ratio
×	×	state_q0003	lev, ncol	kg/kg	Cloud ice mixing ratio
×	×	state_t	lev, ncol	K	Air temperature
×	×	state_u	lev, ncol	m/s	Zonal wind speed
×	×	state_v	lev, ncol	m/s	Meridional wind speed
×		state_pmid	lev, ncol	Pa	Mid-level pressure
×		cam_in_AS DIR	ncol		Albedo for direct shortwave radiation
×		cam_in_AS DIF	ncol		Albedo for diffuse shortwave radiation
×		cam_in_AL DIR	ncol		Albedo for direct longwave radiation
×		cam_in_AL DIF	ncol		Albedo for diffuse longwave radiation
×		cam_in_LWUP	ncol	W/m ²	Upward longwave flux
×		cam_in_SNOWHLAND	ncol	m	Snow depth over land (liquid water equivalent)
×		cam_in_SNOWHICE	ncol	m	Snow depth over ice
×		cam_in_LANDFRAC	ncol		Land area fraction
×		cam_in_ICEFRAC	ncol		Sea-ice area fraction
	×	cam_out_NETSW	ncol	W/m ²	Net shortwave flux at surface
	×	cam_out_FLWDS	ncol	W/m ²	Downward longwave flux at surface
	×	cam_out_PRECSC	ncol	m/s	Snow rate (liquid water equivalent)
	×	cam_out_PRECC	ncol	m/s	Rain rate
	×	cam_out_SOLS	ncol	W/m ²	Downward visible direct solar flux to surface
	×	cam_out_SOLL	ncol	W/m ²	Downward near-IR direct solar flux to surface
	×	cam_out_SOLSD	ncol	W/m ²	Downward visible diffuse solar flux to surface
	×	cam_out_SOLL D	ncol	W/m ²	Downward near-IR diffuse solar flux to surface

Table 4: Overview of input variables (first column) and output variables (second column) of the E3SM-MMF physics calculations (including the CRM) that are stored in ClimSim. The other columns indicate the variable name, dimensions, units, and a brief description. IR is short for infrared, which is also often referred to as “longwave” radiation among atmospheric scientists.

B.5 Target Audiences

In essence, this benchmark aims to democratize and expand access to advanced climate modeling. High-potential architectures will undergo testing in the superparameterized version of the DOE’s primary climate model, E3SM. Successful integration would substantially reduce computational costs for the DOE when contemplating the deployment of MMF technology in climate prediction. E3SM’s external user community, typically deterred by the extensive computational demands of superparameterized simulators, also stands to benefit. Currently, only a minority with substantial computing resources can engage with such models. A successful recipe for ClimSim could thus democratize the use of explicit convection for a broader user base. If performant architectures also prove effective in the NCAR Community Earth System Model (CESM) - the world’s most widely used open-source climate simulator - the user base could expand significantly. Given its software similarities to E3SM, it is logical to expect that ClimSim’s learnt parameterizations will be readily adaptable to CESM. Moreover, we anticipate that a successful hybrid machine learning climate simulator will bring benefits to a diverse range of industry sectors, including those vulnerable to climate risks (such as agriculture, energy, and tourism), as well as the climate risk industry itself (such as insurance and risk assessment).

Appendix C. Baseline Models

This section offers a detailed depiction of seven baseline models. Every facet of model designs, excluding the dimensions of the input and output layers, differs among the models. We recognize that while this approach maximizes the differentiation among baseline models, such extensive degrees of freedom complicate the complete isolation of the effects arising from optimization parameter choices and those originating from the model architecture itself. In future ClimSim releases, baseline models will share more constraints (including optimization parameters) to highlight the performance difference due to model architectures.

C.1 Multilayer Perceptron (MLP)

A multilayer perceptron (MLP) is a basic, densely connected artificial neural network. We used KerasTuner (O’Malley et al., 2019) with a random search algorithm for hyperparameter optimization. The following hyperparameters were optimized: the number of hidden layers (N_{layers}), the number of nodes per layer (N_{nodes}), activation function, and batch size. The search domains were:

- N_{layers} : [3, 4, 5, 6, 7, 8, 9, 10, 11, 12, 13]
- N_{nodes} : [128, 256, 384, 512, 640, 768, 896, 1024]
- Activation function: [ReLU, LeakyReLU ($\alpha = 0.15$), eLU ($\alpha = 1.0$)]
- Batch size: [48, 96, 192, 384, 768, 1152, 1536, 2304, 3072]
- Optimizer: [Adam, RAdam, RMSprop, SGD]

Note that N_{nodes} was selected independently for each hidden layer. For example, for $N_{\text{layers}} = k$, N_{nodes} was drawn from the search domain k times. The width of the last hidden

layer was fixed at 128. The output layer utilized the linear activation function for the first 120 outputs (corresponding to the heating and moistening tendencies), and ReLU for the remaining 8 variables (corresponding positive-definite surface variables). The loss function was taken as the mean squared error (MSE), and the learning rate was defined using a cyclic scheduler, with an initial learning rate of 2.5×10^{-4} , maximum of 2.5×10^{-3} , and step size of 4 epochs.

Following Yu et al. (2023, *Under Review*), we conducted the hyperparameter search in two stages. In the first stage, a total of 8,257 randomly-drawn hyperparameter configurations were trained and evaluated with a tiny subset of the full training set, sub-sampled in the time dimension with a stride of 37. In the second stage, the top 0.2% candidates (160 hyperparameter configurations) were re-trained with a larger fraction of the full training set (sub-sampled with a stride of 7), and then evaluated for our MLP baseline. After this two-step search process, the best hyperparameter configuration was identified as: $N_{\text{layers}} = 5$, $N_{\text{nodes}} = [768, 640, 512, 640, 640]$, LeakyReLU activation, a batch size of 3,072, and RAdam optimizer. The MLP baseline has approximately 1.75 million parameters and executes 3.50 MFlops on one data point, the architecture of which is summarized in Figure 8.

To provide some context on the amount of variance in model performance that can be attributed to random effects of optimization, the top 160 models were selected from our pool of 8,257 trials and scored on the validation set; the 5th to 95th percentile range of this ensemble is shown by the error bars in Figure 2a in the main text and Figure 11 in the Appendix, and by the grey shading in Figures 2b-e in the main text and Figures 12 and 13 in the Appendix.

MLP with expanded features and targets: We built MLP with an expanded set of input and output variables, as elaborated in Section 4.4 of the main text. For the sake of clarity, we designate an MLP model employing the subset of available variables (outlined in Section 4 of the main text) as "MLPv1," while an MLP model utilizing the expanded variables is referred to as "MLPv2." The hyperparameter optimization for MLPv2 followed a similar process as MLPv1, with the exception that the search domain of batch size was defined as [2700, 5400, 10800, 21600, 43200, 64800, 86400, 129600, 172800]. After 11,851 search trials, the best hyperparameter configuration was identified as: $N_{\text{layers}} = 3$, $N_{\text{nodes}} = [384, 1024, 640]$, ReLU activation, a batch size of 2,304, and Adam optimizer. The MLPv2 baseline has approximately 1.59 million parameters and executes 3.17 MFlops on one data point.

MLP with the high-resolution dataset: In conjunction with the MLP featuring expanded features and targets, we also constructed MLP models using the high-resolution dataset for both MLPv1 and MLPv2. To differentiate these models from those constructed with the low-resolution dataset, we add the suffix "-ne30" to their names. The hyperparameters for MLPv1-ne30 and MLPv2-ne30 were optimized using the same methodology as was applied to their low-resolution counterparts. For MLPv1-ne30, after 10,296 search trials, the best hyperparameter configuration was identified as: $N_{\text{layers}} = 4$, $N_{\text{nodes}} = [1024, 128, 128, 768]$, leaky ReLU activation, a batch size of 5,400, and Adam optimizer. The MLPv1-ne30 baseline has approximately 0.49 million parameters and executes 0.98 MFlops on one data point. For MLPv2-ne30, after 10,440 search trials, the best hyperparameter configuration was identified as: $N_{\text{layers}} = 3$, $N_{\text{nodes}} = [640, 128, 1024]$, ReLU activation, a batch size

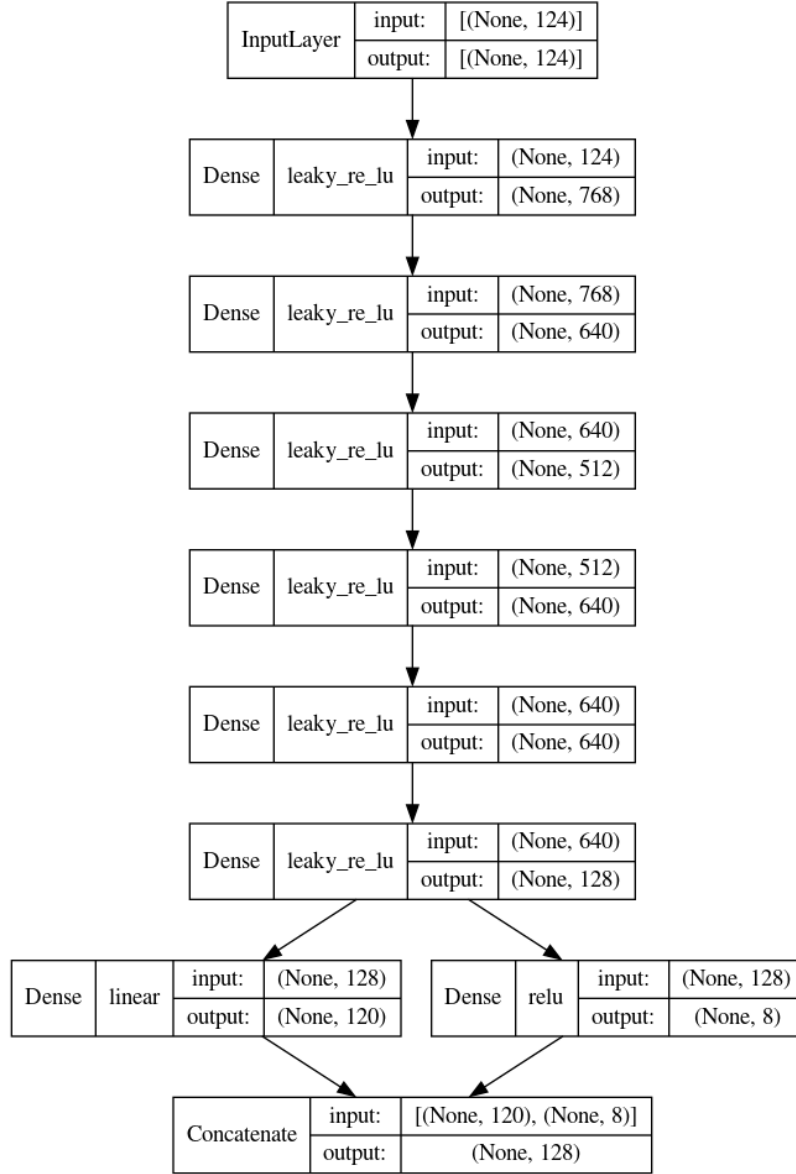


Figure 8: The architecture of the MLP baseline model.

of 2,700, and Adam optimizer. The MLPv2-ne30 baseline has approximately 1.00 million parameters and executes 2.00 MFlops on one data point.

The model performance comparison between MLPv1, MLPv2, MLPv1-ne30, and MLPv2-ne30 is presented in Appendix H.1.

C.2 Randomized Prior Network (RPN)

A randomized prior network (RPN) is an ensemble model (Osband et al., 2018). Each member of the RPN is built as the sum of a trainable and a non-trainable (so-called “prior”) surrogate model; we used MLP for simplicity. Multiple replicas of the networks are constructed by independent and random sampling of both trainable and non-trainable parameters (Yang et al., 2022; Bhouri et al., 2023a). RPNs also resort to data bootstrapping in order to mitigate the uncertainty collapse of the ensemble method when tested beyond the training data points (Bhouri et al., 2023a). Data bootstrapping consists of sub-sampling and randomization of the data each network in the ensemble sees during training. Hyperparameters of individual MLPs (i.e., N_{layers} , N_{nodes} , batch size) did not need to be tuned from scratch and were instead chosen based on the hyperparameter search mentioned in Section C.1. RPN ensembles of 128 networks were considered justified (Yang et al., 2022).

In particular, individual MLPs forming the RPN were considered as fully connected neural networks with $N_{\text{layers}} = 5$, $N_{\text{nodes}} = [768, 640, 512, 640, 640]$, and a batch size of 3,072, as in Section C.1. We utilized ReLU activation (with a negative slope of 0.15) for all layers except for the output layer, where the linear activation function was used.

The MLPs were trained for a total of 13,140 stochastic gradient descent (SGD) steps using the Adam optimizer. The learning rate was initialized at 5×10^{-4} with an exponential decay at a rate of 0.99 for every 1,000 steps. The RPN baseline has approximately 222.3 million parameters (~ 1.74 million per MLP) and executes 0.89 GFlops on one data point.

C.3 Convolutional Neural Network (CNN)

The convolutional neural network (CNN) used is a modified version of a residual network (ResNet). Each ResNet block is composed of two, 1D convolutions (Conv1D) with a 3×3 kernel using “same” padding, and an output feature map size of 406. Each Conv1D is followed by ReLU activation and dropout (with rate = 0.175). Residuals were also 1D convolved using a 1×1 kernel, and added back to the output of the main ResNet block.

The CNN composes 12 such ResNet blocks, followed by “flattening” of the feature map via a 1×1 convolution and eLU activation. Two separate Dense layers (and their corresponding activations) map the output feature map to their respective co-domains: one to $(-\infty, \infty)$ assuming that vertically-resolved variables have no defined range, and another to $[0, \infty)$ for all globally-resolved variables. These were concatenated as the output of the network.

A hyperparameter search was conducted on depth, width, kernel size, activation functions, loss functions, and normalization types using the Hyperband (Li et al., 2018) strategy with the KerasTuner (O’Malley et al., 2019) framework. The search domains were:

- Model depth/number of ResNet blocks: [2, 15]
- Model width: [32, 512]

- Kernel width: [3, 5, 7, 9]
- Activation function: [GeLU, eLU, ReLU, Swish]
- Layer normalization: [True, False]
- Dropout: [0.0, 0.5]
- Optimizer: [SGD, Adam]

The CNN was trained for 10 epochs with an Adam optimizer with standard hyperparameters ($\beta_1 = 0.9$, $\beta_2 = 0.999$, $\epsilon = 1 \times 10^{-7}$). The learning rate was defined using a cyclic scheduler, with an initial learning rate of 1×10^{-4} , a maximum of 1×10^{-3} , and a step size of $2 \times \lfloor \frac{10,091,520}{12} \rfloor$. A scaling function of $\frac{1}{2.0^{x-1}}$ was applied to the scheduler per step x .

The hyperparameter search was conducted for 12 hours on 8 NVIDIA Tesla V100 32GB cards, with one model executing on each card. A weighted mean absolute error (MAE) was used as the loss function for optimization. We down-weighted the standard MAE loss to de-emphasize repeated scalar values provided to the network as input. The weighted MAE function is defined below:

```
def mae_adjusted(y_true, y_pred):
    abs_error = K.abs(y_pred - y_true)
    vertical_weights = K.mean(abs_error[:, :, 0:2]) * (120/128)
    scalar_weights = K.mean(abs_error[:, :, 2:10]) * (8/128)
    return vertical_weights + scalar_weights
```

The CNN baseline has approximately 13.2 million parameters and executes 1.59 GFlops on one data point. The architecture is visualized below in Figure 9.

C.4 Heteroskedastic Regression (HSR)

We quantified the inherent stochasticity in the data $\mathcal{D} = \{(\mathbf{x}_1, \mathbf{y}_1), \dots, (\mathbf{x}_n, \mathbf{y}_n)\}$, and the uncertainty in our prediction by providing a distributional prediction instead of a point estimate. In heteroskedastic regression (HSR), this predictive distribution is modeled explicitly; here as independent Gaussians with unique mean μ_k and precision (inverse variance) τ_k for each variable. We assumed

$$\mathbf{y}_i | \mathbf{x}_i \sim \mathcal{N}(\mu(\mathbf{x}_i), \text{Diag}(\tau(\mathbf{x}_i)^{-1})),$$

and parameterized both μ and τ as over-parameterized feed-forward neural networks (i.e., MLPs) $\hat{\mu}_\theta(\mathbf{x})$ and $\hat{\tau}_\phi(\mathbf{x})$, respectively. This yielded the corresponding predictive distribution

$$\hat{\mathbf{y}}_i | \mathbf{x}_i \sim \mathcal{N}(\hat{\mu}_\theta(\mathbf{x}_i), \text{Diag}(\hat{\tau}_\phi(\mathbf{x}_i)^{-1})),$$

which was fitted with maximum likelihood estimation (MLE) by minimizing the objective

$$\mathcal{L}(\theta, \phi) = \frac{1}{2n} \sum_{i=1}^n \left[\|\hat{\tau}_\phi(\mathbf{x}_i) (\mathbf{y}_i - \hat{\mu}_\theta(\mathbf{x}_i))\|_2^2 - \mathbf{1}^T \log(\hat{\mu}_\theta(\mathbf{x}_i)) \right].$$

Note that, due to the flexibility of the neural networks, this formulation is ill-posed. It may lead to cases of extreme overfitting where $\hat{\tau}_\phi(\mathbf{x}_i) \approx \mathbf{y}_i$, $\hat{\tau}_\phi(\mathbf{x}_i) \approx \mathbf{0}$, thus making $\mathcal{L}(\theta, \phi)$

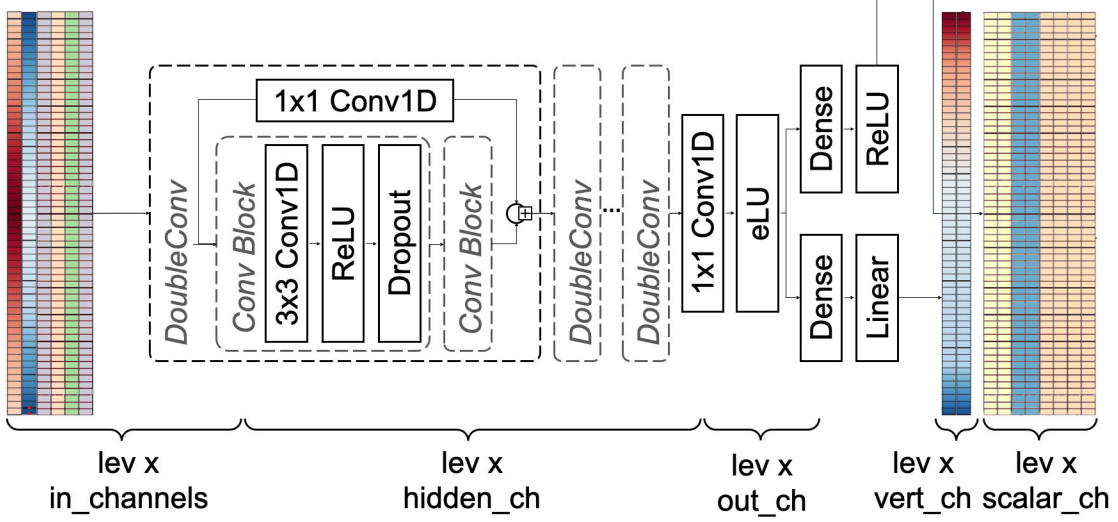


Figure 9: The ResNet-style CNN baseline is comprised of multiple ResNet blocks (i.e., DoubleConv), and applies different activation to the outputs for vertically-resolved and global variables. The channel dimensions are $[\text{in_channels}, \text{hidden_ch}, \text{out_ch}, \text{vert_ch}, \text{scalar_ch}] = [6, 406, 10, 8, 2]$.

completely unstable. Hence, we instead minimized a modified objective that included L2-regularization via

$$\mathcal{L}_{\rho, \gamma}(\theta, \phi) := \rho \mathcal{L}(\theta, \phi) + (1 - \rho) \left[\gamma \|\theta\|_2^2 + (1 - \gamma) \|\phi\|_2^2 \right],$$

where $\rho, \gamma \in (0, 1)$ determines the trade-off between MLE estimation, mean regularization, and precision regularization. We follow Wong-Toi et al. (2023) and set $\rho = 1 - \gamma$ to reduce the hyperparameter search domain.

Specifically, we used two MLPs with layer normalization and ReLU activation, and trained them with gradient-based stochastic optimization. To improve stability, the first third of training was spent on exclusively training $\hat{\mu}_\theta(\mathbf{x}_i)$ with an MSE loss. To optimize hyperparameters, we selected a configuration from 300 trials with a random number of $N_{\text{layers}} = [2, 3, 4]$, $N_{\text{nodes}} = [256, 512, 1,024, 2,048]$, γ (log-uniform in $[0.001, 0.1]$), optimizer = [SGD, Adam] with hyperparameters ($\beta_1 = 0.9$, $\beta_2 = 0.999$), learning rate λ (log-uniform in $[10^{-6}, 10^{-3}]$), and batch size = [1024, 2048, 4096, 8192, 16384]. Each run was trained for 12 epochs total on one NVIDIA GeForce RTX 4080 16GB. We chose the run with the lowest CRPS on the validation data, yielding $N_{\text{layers}} = 4$, $N_{\text{nodes}} = 1,024$, $\gamma = 2.2 \times 10^{-2}$, $\lambda = 7 \times 10^{-6}$, and a batch size of 16,384, trained with Adam. The HSR baseline has approximately 6.63 million parameters and executes 6.85 MFlops per data point.

C.5 Conditional Variational Autoencoder (cVAE)

A conditional generative latent variable model first samples—from a prior $p(\mathbf{z})$ —a point \mathbf{z} in a low-dimensional latent space, which then informs a conditional distribution $p_\theta(\mathbf{y}|\mathbf{z}, \mathbf{x})$ over the target domain. This allows for a complex and flexible predictive distribution. In our case, we used feed-forward neural networks (i.e., MLPs) $\mu_\theta(\mathbf{z}, \mathbf{x})$ and $\sigma_\theta(\mathbf{z}, \mathbf{x})$ with combined parameters θ and model:

$$\begin{aligned}\mathbf{z} &\sim \mathcal{N}(\mathbf{0}, \mathcal{I}) \\ \mathbf{y}|\mathbf{z}, \mathbf{x} &\sim \mathcal{N}(\mu_\theta(\mathbf{z}, \mathbf{x}), \text{Diag}(\sigma_\theta(\mathbf{x})^2))\end{aligned}\tag{3}$$

To fit the model to data $\mathcal{D} = \{(\mathbf{x}_1, \mathbf{y}_1), \dots, (\mathbf{x}_n, \mathbf{y}_n)\}$, we minimized the negative evidence lower bound (NELBO) $\mathcal{L}_\theta(\mathbf{q})$ that bounds the intractable negative marginal likelihood from above via

$$\mathcal{L}_\theta(q) := -\mathbb{E}_{\mathbf{z}_i \sim q} \left[\log \frac{p_\theta(\mathbf{y}_i, \mathbf{z}_i | \mathbf{x}_i)}{q(\mathbf{z}_i | \mathbf{x}_i)} \right] = -\log p_\theta(\mathbf{y}_i | \mathbf{x}_i) + \underbrace{\text{KL}(q \| p_\theta(\mathbf{z}_i | \mathbf{y}_i, \mathbf{x}_i))}_{\geq 0},$$

using an approximation q to the posterior $p_\theta(\mathbf{z}_i | \mathbf{y}_i, \mathbf{x}_i)$. The conditional variational autoencoder (cVAE) (Kingma and Welling, 2014) uses amortized variational inference to optimize θ and q jointly by approximating the latter with e.g., $q_\psi(\mathbf{z}_i) = \mathcal{N}(g_\psi(\mathbf{x}_i), \text{Diag}(h_\psi(\mathbf{x}_i)^2))$, where we again chose $g_\psi(\mathbf{x}_i)$ and $h_\psi(\mathbf{x}_i)$ to be MLPs. This allowed us to optimize for θ and ψ by minimizing

$$\mathcal{L}_\theta(q) \stackrel{\beta=1}{=} \mathbb{E}_{\mathbf{z}_i \sim q_\psi} \left[\frac{1}{2} \left\| \frac{\mathbf{y}_i - \mu_\theta(\mathbf{z}_i, \mathbf{x}_i)}{\sigma_\theta(\mathbf{z}_i, \mathbf{x}_i)} \right\|_2^2 + \mathbf{1}^T \log(\sigma_\theta(\mathbf{z}_i, \mathbf{x}_i)) \right] + \beta \text{KL}(q_\psi(\mathbf{z}_i) \| p(\mathbf{z}_i)) + \text{const}$$

with a Monte Carlo approximation by first sampling \mathbf{z}_i (once) from the variational encoder $q_\psi(\mathbf{z}_i)$. After which, we decoded the predictive mean and standard deviation with the variational decoder $\mu_\theta(\mathbf{z}, \mathbf{x})$ and $\sigma_\theta(\mathbf{z}, \mathbf{x})$. We then computed NELBO as a sum of a reconstruction term and a KL term that regularizes the latent space, averaged over all samples, and back-propagated the gradients. By letting β be a hyperparameter, we manually determined the trade-off between reconstruction quality and latent space structure. Finally, at inference time, we used Equation 3 to sample from the predictive distribution

$$p_\theta(\hat{\mathbf{y}}|\mathbf{x}) = \int p_\theta(\hat{\mathbf{y}}|\mathbf{x}, \mathbf{z}) p(\mathbf{z}) d\mathbf{z}.$$

For both the variational encoder and decoder, we used an MLP with layer normalization, ReLU activation, dropout with $p = 0.05$, and two branching final layers that produced the mean and standard deviation, respectively. We trained both MLPs jointly—with gradient-based stochastic optimization—on the objective described above.

To optimize hyperparameters, we ran 300 trials with a random number of hidden layers $N_{\text{layers}} = [2, 3, 4]$, $N_{\text{nodes}} = [256, 512, 1024, 2048]$, size of the latent space $= [4, 8, 16, 32]$, β (log-uniform in $[0.01, 10]$), optimizer $= [\text{SGD}, \text{Adam}]$ with $(\beta_1 = 0.9, \beta_2 = 0.0999)$, learning rate λ (log-uniform in $[10^{-6}, 10^{-3}]$), L2 regularization α (log-uniform in $[10^{-6}, 10^{-3}]$), and batch size $= [1024, 2048, 4096, 8192, 16384]$. Each run was trained for 5 epochs total on

one NVIDIA GeForce RTX 4080 16GB. The run with the lowest CRPS on the validation data yielded $N_{\text{layers}} = 3$, $N_{\text{nodes}} = 1,024$, and a batch size of 4,096, trained with Adam. In a second step, we fixed these hyperparameters and further fine-tuned β , λ , and α by training for 20 epochs every time, for 10 trials. We found the best model with $\beta = 0.5$, $\lambda = 5 \times 10^{-5}$, $\alpha = 10^{-3}$. The cVAE baseline has approximately 4.9 million parameters and executes 4.88 MFlops per data point.

C.6 Encoder-Decoder (ED)

The Encoder-Decoder (ED) is an adjusted version of the ED presented in Behrens et al. (2022). We keep all tuneable hyperparameters except for the learning rate and the node sizes of input and output layer of ED fixed to the original values that were optimized with a detailed hyperparameter search for the superparameterization of the Community Atmosphere Model version 3 in an aquaplanet setup (Behrens et al., 2022). The Encoder consists of 6 hidden fully-connected layers. The Encoder decreases progressively the dimensionality of the input variables down to 5 nodes in the latent space of the network. These 5 latent nodes are the only input to the decoding part of ED. The Decoder maps the information from the latent space back to 128 nodes in the output layer through 6 progressively wider fully-connected hidden layers (Behrens et al., 2022). We train ED over 40 epochs with a learning rate step after each 7th epoch, which reduces the learning rate by factor 5 (Behrens et al., 2022). The adjusted initial learning rate has a value of 1×10^{-4} . The batch size has a value of 714 samples. As activation functions of all hidden layers we use ReLU and the output layer of the Decoder is ELU-activated (Behrens et al., 2022). As an optimizer during training we use Adam. As a loss function of ED we use a MSE loss and as additional metric the MAE during training. The following list summarizes the key hyperparameters of ED:

- Learning rate: 1×10^{-4} , learning rate decrease after every 7th epoch
- Batch size: 714
- Latent space width: 5 Nodes
- Encoder node size: [124, 463, 463, 232, 116, 58, 29, 5]
- Decoder node size: [5, 29, 58, 116, 232, 463, 463, 128]
- Encoder activation functions: [Input, ReLU, ReLU, ReLU, ReLU, ReLU, ReLU, ReLU]
- Decoder activation functions: [Input, ReLU, ReLU, ReLU, ReLU, ReLU, ReLU, ELU]
- Optimizer: Adam

To prevent overfitting we shuffle the training data set before each epoch. ED baseline has approximately 832,000 parameters, with 415,000 parameters in the Encoder and 417,000 parameters in the Decoder. In total, ED executes 1.66 MFlops per data point, with 829 kFlops per data point for the Encoder and 832 kFlops per data point for the Decoder.

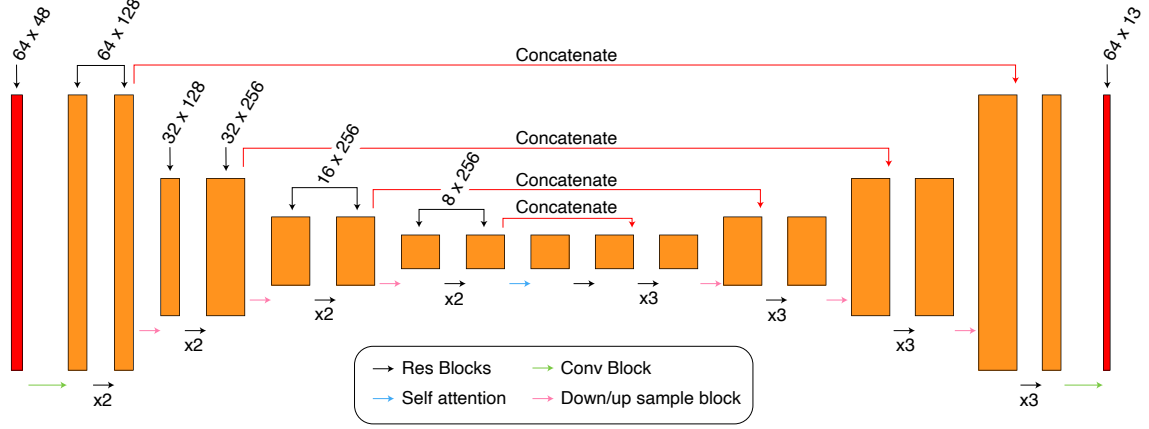


Figure 10: The schematic of the U-Net architecture. This is a replication of Figure 1 from Hu et al. (2025). The U-Net architecture is comprised of multiple ResBlocks, with a depth of 4 and feature dimension sizes of [128, 256, 256, 256]. The model requires preparing the input and output as sequence data, with different features as the channels of the sequence and the sequence as the vertical dimension.

C.7 U-Net (UNET)

The U-Net model is the same architecture used in Hu et al. (2025). Hu et al. (2025) adapted the 2D U-Net model from Song and Ermon (2019) into a 1D version for column-to-column prediction. A U-Net model can efficiently learn and use the vertical structures in the atmosphere. The architecture schematic is shown in Figure 10. Each ResBlock consists of the following operations:

$$y = \text{Conv1D}(\text{GM}(\text{Conv1D}(\text{silu}(\text{GM}(x)))) + x$$

This series of operations includes group normalization (GM), sigmoid linear unit (silu) activation function, 1D convolution (Conv1D) with a kernel size of 3, and a residual connection. The U-Net has a depth of 4, corresponding to 3 downsampling and 3 upsampling stages (pink arrows in Figure 10), with the feature dimensions at each stage given by $N_{\text{latent}} = [128, 256, 256, 256]$.

The U-Net model is trained with a batch size of 512 using the Adam optimizer on 4 GPUs. The learning rate has an initial value of 1×10^{-3} with a reduced-on-plateau scheduler which automatically reduces the learning rate by 0.3162 when validation loss has not decreased for 2 epochs. The UNET baseline has approximately 13 million parameters and executes 224 KFlops per data point.

C.8 Inference Cost

Table 5 documents the inference cost for each of the seven baseline models.

	CNN	ED	HSR	MLP	RPN	cVAE	UNET
Number of Parameters (M)	13.2	0.832	6.63	1.75	222.3	4.9	13.0
MFlops Per Data Point	1590	1.66	6.85	3.50	890	4.88	0.224

Table 5: The number of learnable parameters (in millions) and Megaflops (MFlops) per data point for each of the seven baseline models.

Appendix D. Baseline Model Evaluations

D.1 Metrics

D.1.1 DETERMINISTIC METRICS

Mean Absolute Error (MAE):

$$\text{MAE} = \frac{1}{n} \sum_{i=1}^n |X_i - y| \quad (4)$$

Root Mean Squared Error (RMSE):

$$\text{RMSE} = \sqrt{\frac{1}{n} \sum_{i=1}^n (X_i - y)^2} \quad (5)$$

Coefficient of Determination (R^2):

$$R^2 = 1 - \frac{\sum_{i=1}^n (X_i - y)^2}{\sum_{i=1}^n (X_i - \bar{X})^2} \quad (6)$$

In Equations 4–6, X_i and y represent the true and predicted values, respectively. The mean of the true values of the dependent variable is denoted by \bar{X} .

D.1.2 STOCHASTIC METRIC (CRPS)

The continuous ranked probability score (CRPS) is a generalization of the MAE for distributional predictions. CRPS penalizes over-confidence in addition to inaccuracy in ensemble predictions—a lower CRPS is better. For each variable, it compares the ground truth target y with the cumulative distribution function (CDF) F of the prediction via

$$\begin{aligned} \text{CRPS}(F, y) &:= \int (F(x) - \mathbf{1}_{\{x \geq y\}})^2 dx \\ &= \mathbb{E}[|X - y|] - \frac{1}{2} \mathbb{E}[|X - X'|], \end{aligned}$$

where $X, X' \sim F$ are independent and identically distributed (*iid*) samples from the distributional prediction. We use the non-parametric “fair estimate to the CRPS” (Ferro, 2014),

estimating F with the empirical CDF of $n = 32$ *iid* samples $X_i \sim F$:

$$\text{CRPS}(\mathbf{X}, y) := \frac{1}{n} \sum_{i=1}^n |X_i - y| - \frac{1}{2n(n-1)} \sum_{i=1}^n \sum_{j=1}^n |X_i - X_j| \quad (7)$$

The first term in Equation 7 is the MAE between the target and samples of the predictive distribution, while the second term is small for small predictive variances, vanishing completely for point estimates. Note that this definition extends to ensemble models, where we take the prediction of each ensemble member as a sample of an implicit predictive distribution.

Variable	RMSE [W/m ²]							CRPS [W/m ²]						
	CNN	ED	HSR	MLP	RPN	cVAE	UNET	CNN	ED	HSR	MLP	RPN	cVAE	UNET
dT/dt	4.369	4.696	4.825	4.421	4.482	4.721	4.189	–	–	2.158	–	2.305	2.708	–
dq/dt	7.284	7.643	7.896	7.322	7.518	7.780	7.173	–	–	3.645	–	4.100	4.565	–
NETSW	36.91	28.537	37.77	26.71	33.60	38.36	25.130	–	–	14.62	–	14.82	20.53	–
FLWDS	10.86	9.070	8.220	6.969	7.914	8.530	6.164	–	–	4.561	–	4.430	6.732	–
PRECSC	6.001	5.078	6.095	4.734	5.511	6.182	4.384	–	–	2.905	–	2.729	3.513	–
PRECC	85.31	76.682	90.64	72.88	76.58	88.71	69.363	–	–	34.30	–	30.08	40.17	–
SOLS	22.92	17.999	23.61	17.40	20.61	23.27	16.165	–	–	8.369	–	8.309	11.91	–
SOLL	27.25	22.540	27.78	21.95	25.22	27.81	20.794	–	–	10.14	–	10.49	14.42	–
SOLSD	12.13	9.917	12.40	9.420	11.00	12.64	8.713	–	–	4.773	–	4.649	5.945	–
SOLLD	12.10	10.417	12.47	10.12	11.25	12.63	9.591	–	–	4.599	–	4.682	5.925	–

Table 6: Globally-averaged RMSE and CRPS. Each metric is calculated at each grid point, then horizontally-averaged and (for dT/dt and dq/dt) vertically-averaged. The units of non-energy flux variables are converted to a common energy unit, W/m², following Section E.2. Best model performance for each variable is highlighted in bold.

D.2 Results

MAE and R² of the baseline models are presented in the main text (e.g., Table 2 and Figure 2 in the main text). Here, we show RMSE and CRPS in Table 6 and Figures 11, 12, and 13.

D.3 Fit Quality

Scatter plots of truth versus prediction are shown in this section (supplementary Figures 16 to 22 in Appendix H). While many variables exhibit consistent fit quality, some show notable variability between baselines, as seen with snow precipitation rate predictions (Figure 4 in the main text). The performance of the U-Net baseline and our optimized deterministic baseline (MLP) suggest these issues are avoidable. However, note that our prediction problem has a multi-variate and multi-dimensional nature.

Appendix E. Guidance

E.1 Physical Constraints

Mass and energy conservation are important criteria for Earth system modeling. If these terms are not conserved, errors in estimating sea level rise or temperature change over time

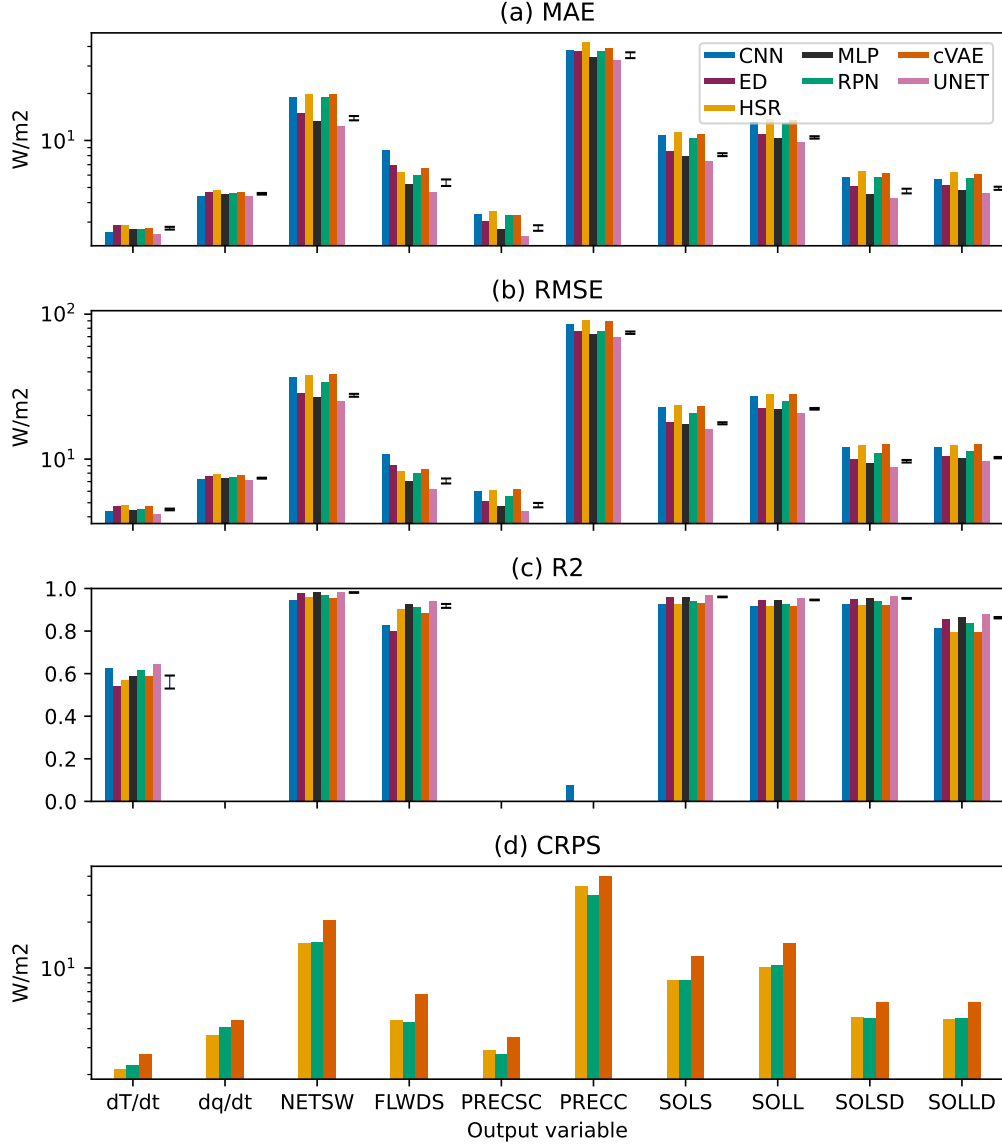


Figure 11: Averaged (a) MAE, (b) RMSE, (c) R^2 , and (d) CRPS. Each metric is calculated at each grid point, then horizontally-averaged and (for dT/dt and dq/dt) vertically-averaged. For MAE, RMSE, and CRPS, the units of non-energy flux variables are converted to a common energy unit, W/m^2 , following Section E.2. Negative values are not shown for R^2 . Error bars show the 5- to 95-percentile range of MLP.

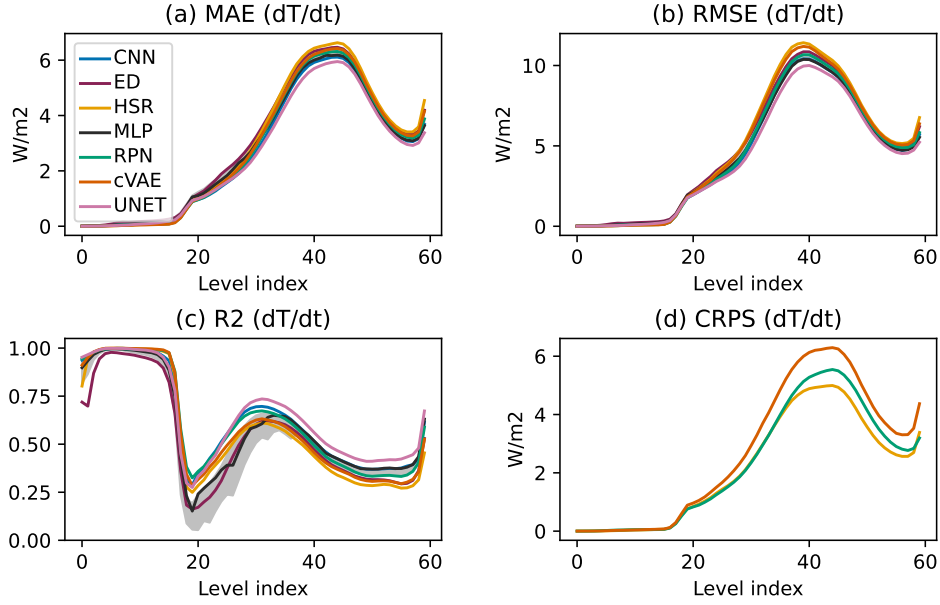


Figure 12: Vertical structures of horizontally-averaged (a) MAE, (b) RMSE, (c) R^2 , and (d) CRPS of dT/dt . For MAE, RMSE, and CRPS, the units of non-energy flux variables are converted to a common energy unit, W/m^2 , following Section E.2. Negative values are not shown for R^2 . Grey shadings show the 5- to 95-percentile range of MLP.

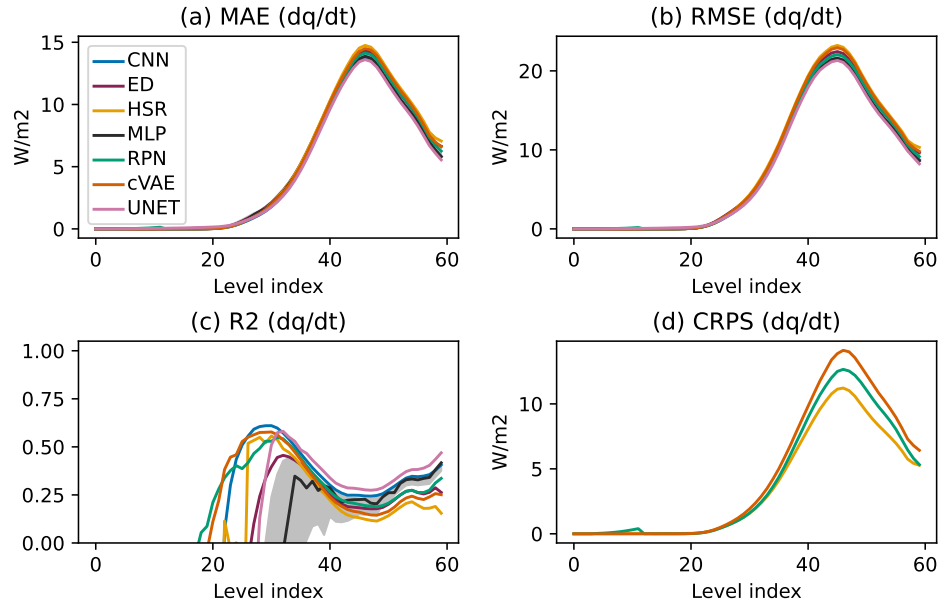


Figure 13: Similar to Figure 12, but for dq/dt .

may become as large as the signals we hope to measure. Enforcing conservation on emulated results helps constrain results to be physically plausible and reduce the potential for errors accumulating over long time scales.

In the atmospheric component of the E3SM climate model, mass is composed of “dry air” (i.e., well-mixed gases such as molecular nitrogen and oxygen) and water vapor. During the physics parameterizations we seek to emulate, there is no lateral exchange of mass across columns of the host model, and the model assumes that the total mass in each column and level remains unchanged. Thus, while surface pressure (`state_ps`) is part of the state structure we seek to emulate, that surface pressure component must be held fixed. The water mass, however, is not held fixed, requiring fictitious sources and sinks of dry air, which are corrected later in the model—outside of the “emulated” part of the code—and is not addressed within the emulator.

Changes in column water mass should balance the sources and sinks of water into and out of the column through surface fluxes. The surface source of water is an input to the emulator via the `cam_in` structure. The surface sink of water is generated by the model, and hence emulated in our case. The net surface water flux (source minus sink) should be equal to the tendency of water mass within the column (8). The mass of water is held in five separate terms within the `state` structure: water vapor (q_v), cloud liquid condensate (q_l), cloud ice (q_i), rain (q_r), and snow (q_s). These terms are held as ratios of their mass to the sum of dry air plus water vapor (referred to as specific humidity). The “ δ ” refers to the difference (after minus before computation) in each quantity owing to the CRM physics. The layer mass (sum of dry air and water vapor) of level k is equal to the pressure thickness of that layer Δp_i (the difference between top and bottom interface pressure for level i) divided by the gravitational acceleration g (assumed constant). The timestep length is δt . In addition to conserving water mass, we required each individual water constituent to remain greater than or equal to zero in every layer within the column. In Equation 8, E is the surface source of water (evapotranspiration) and P is the surface sink of water (precipitation):

$$\sum_i (\delta q_v + \delta q_l + \delta q_i + \delta q_r + \delta q_s) \frac{\Delta p_i}{g \delta t} = E - P \quad (8)$$

For the portion of the code that we try to emulate, the water source E is not applied such that the only surface flux to account for when constraining water conservation is the precipitation flux (P , `cam_out_PRECC`). Unfortunately, only the input and output state variables for water vapor (`state_q0001`), cloud liquid (`state_q0002`), and cloud ice (`state_q0003`) are available. Additional storage terms related to precipitating water that have not exited the column over the course of a model timestep are unavailable in the current output. Therefore, we are unable to exactly enforce water conservation. Estimates show relative errors of a couple percent resulting from the lack of these precipitation mixing ratios. We can still require that the relative error be small. To accomplish this, we compared the “expected” total water, based on the combination of the input and surface fluxes, to the predicted total water. In

the equations below, superscript o denotes output and superscript i denotes input:

$$\begin{aligned}\text{Total Water (Actual)} &= \sum_i (\delta q_v^o + \delta q_l^o + \delta q_i^o) \frac{\Delta p_i}{g} \\ \text{Total Water (Expected)} &= \sum_i (\delta q_v^i + \delta q_l^i + \delta q_i^i) \frac{\Delta p_i}{g} - P\delta t \\ \text{Relative Error} &= \frac{\text{Total Water (Expected)} - \text{Total Water (Actual)}}{\text{Total Water (Actual)}}\end{aligned}$$

We required the model to keep the relative error small (e.g., below 5%). Anything further is beyond the limit of the current data.

Like mass conservation, energy conservation can generally be enforced by requiring that the total change within the column is exactly balanced by the fluxes into and out of that column. Because the emulator does not predict upwelling radiative fluxes at the model top (a sink term for energy), we do not have the boundary conditions necessary to constrain column energy tendencies. However, we still required certain criteria be met for physical consistency. First, the downwelling surface shortwave radiative flux cannot exceed the downwelling shortwave flux at the model top (prescribed input `pbuf_SOLIN`). Likewise, the net surface shortwave flux should also be bounded between zero (100% reflection) and the surface downwelling shortwave flux (100% absorption). Additionally, the downwelling longwave flux should not exceed the blackbody radiative flux from the warmest temperature in the column.

In addition to conservation laws, cloud physics are found to be useful to constrain model predictions in ways that significantly benefit online error and stability in hybrid ML-physics climate simulations. Cloud formation is partially governed by the thermal state of the atmosphere. See Appendix F.3.4 for discussions and implementations of some cloud physics constraints and approximations that are beneficial.

E.2 Unit Conversion and Weighting for Interpretable Evaluation

To facilitate the objective evaluation of the model’s prediction, we provided a weight tensor of shape $(d_o, N_{\mathbf{x}})$ to convert raw outputs to area-weighted outputs with consistent energy flux units $[\text{W}/\text{m}^2]$. More details are given below.

To ensure that our evaluation takes the Earth’s spherical geometry into account, we designed an area weighting factor a that depends on the horizontal position \mathbf{x} :

$$a(\mathbf{x}) = \mathcal{A}_{\text{col}}(\mathbf{x}) / \langle \mathcal{A}_{\text{col}} \rangle_{\mathbf{x}}$$

where \mathcal{A}_{col} is the area of an atmospheric column and $\langle \mathcal{A}_{\text{col}} \rangle_{\mathbf{x}}$ the horizontal average of all atmospheric columns’ areas. This formula gives more weight to outputs if their grid cell has a larger horizontal area. To ensure that our evaluation is physically-consistent, we convert all predicted variables to energy flux units $[\text{W}/\text{m}^2]$ (power per unit area). This has to be done for each variable separately.

- For the heating tendency \dot{T} $[\text{K}/\text{s}]$, which depends on the horizontal position \mathbf{x} and vertical level lev , this was done using the specific heat capacity at constant pressure

$c_p [1004.64 \text{ J}/(\text{K} \times \text{kg})]$, where $\Delta p_i [\text{Pa}]$ is the layer's pressure thickness, calculated as the difference between the pressure at the layer's top and bottom interfaces:

$$\dot{T} [\text{W}/\text{m}^2] = \frac{c_p}{g} \times a(\mathbf{x}) \times \Delta p_i(\text{lev}) \times \dot{T} [\text{K}/\text{s}]$$

- For the water concentration tendency $\dot{q} [\text{s}^{-1}]$, which also depends on \mathbf{x} and lev, this was done using the latent heat of vaporization of water vapor at constant pressure $L_v [2.50 \times 10^6 \text{ J}/\text{kg}]$:

$$\dot{q} [\text{W}/\text{m}^2] = \frac{L_v}{g} \times a(\mathbf{x}) \times \Delta p_i(\text{lev}) \times \dot{q} [\text{s}^{-1}]$$

Note that there is some level of arbitrariness, as the exact latent heat depends on which water phase is assumed to calculate the energy transfer. Here, we chose to weigh all phases using L_v to give them comparable weights in the evaluation metrics.

- For momentum tendencies $\dot{u} [\text{m}/\text{s}^2]$, which also depend on \mathbf{x} and lev, we used a characteristic wind magnitude $|\mathbf{U}| [\text{m}/\text{s}]$ to convert these tendencies into turbulent kinetic energy fluxes, in units W/m^2 , making them comparable to $\dot{T} [\text{W}/\text{m}^2]$ and $\dot{q} [\text{W}/\text{m}^2]$:

$$\dot{u} [\text{W}/\text{m}^2] = \frac{|\mathbf{U}|}{g} \times a(\mathbf{x}) \times \Delta p_i(\text{lev}) \times \dot{u} [\text{m}/\text{s}^2]$$

Note that there is some level of arbitrariness in the choice of $|\mathbf{U}| [\text{m}/\text{s}]$, which could e.g., be chosen so that the variances of $\dot{u} [\text{W}/\text{m}^2]$ and $\dot{T} [\text{W}/\text{m}^2]$ are comparable.

- Precipitation rate variables $P [\text{m}/\text{s}]$ were also be converted to energy fluxes using L_v and the density of liquid water $\rho_w [\text{kg}/\text{m}^3]$ (or the density of snow/ice for solid precipitation), though they do not require vertical integration:

$$P [\text{W}/\text{m}^2] = L_v \times \rho_w \times a(\mathbf{x}) \times P [\text{m}/\text{s}]$$

- Finally, surface energy fluxes $\mathcal{F} [\text{W}/\text{m}^2]$ were simply multiplied by $a(\mathbf{x})$ to account for area-weighting.

Note that while these choices ensured unit consistency, facilitating the physical interpretation of our evaluation metrics, we recommend tailoring the exact choice of physical constants to the application of interest.

E.3 Additional Guidance

Normalization: Normalization that goes beyond removing vertical structure could be strategic, such as removing the geographical mean (e.g., latitudinal, land/sea structure) or composite seasonal variances (e.g., local smoothed annual cycle) present in the data. For variables exhibiting exponential variation and approaching zero at the highest level (e.g., metrics of moisture), log-normalization might be beneficial.

Further ML Approaches: Recent methods to capture multi-scale processes using neural operators that learn in a discretization-invariant manner and can predict at higher resolutions than available during training time (Li et al., 2021) may be attractive. Their performance can be further enhanced by incorporating physics-informed losses at a higher resolution than available training data (Li et al., 2023). Ideas on ML modeling for subgrid closures from adjacent fields like turbulent flow physics and reactive flows can also be leveraged for developing architectures with an inductive bias for known priors (Ling et al., 2016), easing prediction of stiff non-linear behavior (MacArt et al., 2021; Xing et al., 2021; Brenner et al., 2019), generative modeling with physical constraints (Subramaniam et al., 2020; Kim et al., 2019) and for interpretability of the final trained models (MacArt et al., 2021).

Appendix F. Online Evaluation Pipeline and Experiment Details

This section provides a detailed example of the online evaluation pipeline for hybrid simulations. First, we describe the integration of the Python-based machine learning (ML) model into the Fortran-based climate simulator using the Pytorch-Fortran bindings library (Alexeev, 2023). This integration requires the ML model to be in the TorchScript format, which we will explain in the following subsection, including examples and notes on converting a PyTorch model into TorchScript. Next, we present online results, citing our work in Hu et al. (2025) to illustrate methods for evaluating online errors, share insights for optimizing stability and performance, and showcase the best online errors we have achieved so far along with potential pathways for further improvements.

F.1 Converting PyTorch Models to TorchScript

Converting a PyTorch model to TorchScript is straightforward. However, it is essential to ensure that the model does not use operations unsupported by TorchScript. Most standard PyTorch operations are supported, but some advanced or less common operations may not be. Documentation for supported operations can be found at https://pytorch.org/docs/stable/jit_builtin_functions.html#builtin-functions, and unsupported constructs are listed at https://pytorch.org/docs/stable/jit_unsupported.html#jit-unsupported.

TorchScript requires more static typing compared to regular Python. Ensure your functions have clear type annotations and avoid using Python-only constructs unsupported by TorchScript. For detailed instructions, refer to the official TorchScript documentation: <https://pytorch.org/docs/stable/jit.html>.

Below is an example of how to convert a PyTorch MLP model to TorchScript:

```
import torch
import torch.nn as nn
import torch.jit

# Define the MLP model
class MLP(nn.Module):
    def __init__(self, in_dims: int = 512, out_dims: int = 368):
        super(MLP, self).__init__()
        self.linear1 = nn.Sequential(
            nn.Linear(in_dims, 512),
```

```

        nn.ReLU()
    )
    self.final_linear = nn.Linear(512, out_dims)

    def forward(self, x: torch.Tensor) -> torch.Tensor:
        x = self.linear1(x)
        x = self.final_linear(x)
        return x

# Create an instance of the model
model = MLP()

# Convert the model to TorchScript using scripting
scripted_model = torch.jit.script(model)

# Set the model to evaluation mode
scripted_model = scripted_model.eval()

# Save the TorchScript model to a file
scripted_model.save('model.pt')

```

F.2 Metrics for Evaluating Hybrid Climate Simulators

Root Mean Square Error: Our online evaluation metrics are computed separately for each variable in the hybrid simulations. The goal is to measure the error in simulated climate by analyzing state variables that are sufficiently averaged in space and time. For a given month, RMSE for each variable is calculated as follows:

$$\text{RMSE} = \sqrt{\sum_{i=1}^{S_m} w_i (\hat{y}_m - y_m)^2}$$

where:

- S_m is the number of samples (each grid cell is one sample) across the entire globe, both horizontally and vertically.
- \hat{y}_m represents the values from the hybrid simulation averaged over the entire month.
- y_m represents the values from the reference simulation averaged over the entire month.
- w_1, w_2, \dots, w_{S_m} are mass-weights that sum to 1, proportional to the air mass in each grid cell.

Zonal Mean Bias: Additionally, we evaluate the long-term zonal mean bias, which measures the average difference between the hybrid simulation and the reference simulation across various atmospheric variables, such as temperature, moisture, wind, cloud water, and cloud ice. The zonal mean bias is derived by comparing variables averaged over time and longitudes. The E3SM-MMF climate simulator outputs variables on unstructured grids instead of regular latitude-longitude grids. To average a variable over all longitudes, we first define latitude bins. For the low-resolution version of the ClimSim dataset, we choose

10-degree intervals from 90°S to 90°N. Within each bin, we count all the grid columns that fall into the bin and calculate the horizontal average of those columns weighted by their area.

F.3 Experiment Setup for Online Testing

F.3.1 MULTILAYER PERCEPTRON (MLP)

We used the architecture parameters recommended from the hyperparameter search in Appendix C.1, with $N_{\text{layers}} = 3$, $N_{\text{nodes}} = [384, 1024, 640]$, and ReLU activation. We trained these MLP models with a batch size of 1024 using the Adam optimizer on 4 GPUs. The training utilized the full low-resolution training data without subsampling.

F.3.2 U-NET

We use the same U-Net architecture parameters as in Hu et al. (2025), which are documented in Appendix C.7. Similar to the MLP models, we trained these U-Net models with a batch size of 1024 using the Adam optimizer on 4 GPUs, utilizing the full low-resolution training data without subsampling.

F.3.3 ADDITIONAL INPUTS FOR THE U-NET-EXPANDED-CONSTRAINED MODEL

The U-Net-expanded-constrained, the best-performing online benchmark model from Hu et al. (2025), utilized additional input variables listed in Table 7. These inputs include large-scale forcing at the current and previous time steps, and the convection memory (i.e., the target) at two previous time steps. Large-scale forcing and convection memory are also used in Han et al. (2020); Wang et al. (2022b); Han et al. (2023). Cosine and sine of latitudes are included as well. When cloud physics constraints are enabled (see Appendix F.3.4), liquid cloud and ice cloud inputs are replaced with the corresponding total cloud condensate inputs (liquid plus ice), along with a diagnosed fraction of liquid cloud based on temperature. All these inputs can be retrieved from the existing ClimSim dataset. Retrieving large-scale forcing and convection memory requires using continuous time series data without gaps.

Dynamical Forcing: Dynamical forcing can be calculated as follows:

```
state_t_dyn(t=0) = (state_t_in(t=0) - state_t_out(t=-1)) / 1200
state_q0001_dyn(t=0) = (state_q0001_in(t=0) - state_q0001_out(t=-1)) / 1200
state_q0002_dyn(t=0) = (state_q0002_in(t=0) - state_q0002_out(t=-1)) / 1200
state_q0003_dyn(t=0) = (state_q0003_in(t=0) - state_q0003_out(t=-1)) / 1200
state_q0_dyn = state_q0001_dyn + state_q0002_dyn + state_q0003_dyn
state_u_dyn(t=0) = (state_u_in(t=0) - state_u_out(t=-1)) / 1200
```

Here, the subscripts ‘_in’ and ‘_out’ refer to the variables in the input and output files, respectively. The current model time step is denoted as $t = 0$, and $t = -1$ represents the previous time step. Dynamical forcing represents the rate of change of a variable between two time checkpoints over one time step (1200 seconds). The first checkpoint is before the call to the embedded cloud resolving model (CRM) in the multi-scale climate simulator (see Section A.2) at the current time step, and the second is immediately after the call to the CRM at the previous time step. The changes in temperature, water, and wind fields during this period are due to model physics outside the CRM, primarily advection from the host

dynamical model’s planetary scale fluid solver. These dynamical tendencies of temperature, total water (vapor plus cloud), and zonal winds are applied to the CRM grids during the CRM calculation, making them useful input features for training.

Convection Memory: Convection memory refers to the residual effects of convective processes in the CRM model that might not be fully captured by the values in the coarser grids of the host climate simulator. We utilize the CRM tendencies from two previous time steps to represent this convection memory, as suggested by Han et al. (2020); Wang et al. (2022b); Han et al. (2023). At each time step, the CRM tendencies can be retrieved as follows:

```
state_t_prvphy = (state_t_out - state_t_in) / 1200
state_q0001_prvphy = (state_q0001_out - state_q0001_in) / 1200
state_q0002_prvphy = (state_q0002_out - state_q0002_in) / 1200
state_q0003_prvphy = (state_q0003_out - state_q0003_in) / 1200
state_u_prvphy = (state_u_out - state_u_in) / 1200
```

Hu et al. (2025) shows that these additional features can boost the offline R^2 skill, but their effects for online performance remain an open research question. We encourage curious readers to explore using these additional features and test their effects.

During the hybrid simulation where an ML emulator replaces the CRM, the previous steps’ ML predictions are used as the convection memory. Because this simulation requires information from previous steps as input features, the hybrid simulation must start by calling the CRM for during the initial a few host simulator’s time steps before switching to using only the ML emulator. When launching a brand new hybrid simulation, the atmospheric fields in the CRM typically start from an unrealistic initial condition and require some host-model time steps to form realistic clouds and storms that are consistent with the training data. It is important to fully spin up the CRMs before switching to using only the ML emulator. For a brand new simulation, we recommend a spin-up period of at least one simulation day. In our container workflow, we can launch the hybrid simulation by restarting from the previous simulation where the atmosphere is already spun up. When this restarting configuration is used, we only need to run the CRM for a few steps, depending on how many previous step input features are required.

F.3.4 IMPLEMENTING CLOUD PHYSICS CONSTRAINTS

In this and the following section we describe two physical constraints used in Hu et al. (2025) that are helpful to achieve reasonable performance on the online task related to cloud condensate.

Liquid-Ice Cloud Partition: The formulation of cloud microphysics in the CRM uses temperature to determine the mass of liquid and ice clouds on each grid, as a function of a more fundamental total non-precipitating water prognostic variable. Liquid clouds are only allowed to exist when the temperature is above 273.16K, and ice clouds are only allowed below 253.16K. In between these temperatures, the fraction of liquid cloud over the total cloud mixing ratio follows a linear function of temperature. Hu et al. (2025) demonstrates that this temperature-based partition relationship between liquid and ice clouds holds well on the grid of the host E3SM model. To incorporate this constraint, the constrained U-Net

In	Out	Variable	Dimensions	Units	Description
×		state_t_dyn	lev, ncol, t=0,-1	K/s	Large-scale forcing of temperature
×		state_q0_dyn	lev, ncol, t=0,-1	kg/kg/s	Large-scale forcing of total water
×		state_u_dyn	lev, ncol, t=0,-1	m/s ²	Large-scale forcing of zonal wind
×		state_t_prvphy	lev, ncol, t=-1,-2	K/s	Temperature tendency at previous steps
×		state_q0001_prvphy	lev, ncol, t=-1,-2	kg/kg/s	Water vapor tendency at previous steps
×		state_q0002_prvphy	lev, ncol, t=-1,-2	kg/kg/s	Liquid cloud tendency at previous steps
×		state_q0003_prvphy	lev, ncol, t=-1,-2	kg/kg/s	Ice cloud tendency at previous steps
×		state_u_prvphy	lev, ncol, t=-1,-2	m/s ²	Zonal wind tendency at previous steps
×		clat	ncol		Cosine of latitude
×		slat	ncol		Sine of latitude
×		liq_partition	lev, ncol		Fraction of liquid cloud

Table 7: Additional input variables used in the U-Net model

model predicts only the total cloud (liquid plus ice) change and then diagnoses the liquid and ice clouds based on the updated temperature.

Cloud Top Capped by the Tropopause Layer: The tropopause is the boundary between the lower atmosphere (troposphere) and the upper atmosphere (stratosphere). It acts like a ceiling for weather systems. When a storm’s rising air reaches this boundary, it encounters a very stable layer that prevents further upward movement, effectively capping cloud formation below a dynamical barrier. To identify the tropopause, we look for the lowest altitude where the pressure is below 400 hPa and the potential temperature vertical gradient is steep (greater than 10 K/km). In our simulations, any clouds that form above the tropopause (either from strong storms or being moved up by other atmospheric processes) are quickly removed by falling back down or evaporating. Hu et al. (2025) showed that residual clouds above the tropopause after CRM are rare (but not zero) and have low water content (less than 10^{-3} g/kg). The empirical conditions and thresholds used to detect the tropopause could be refined further. To improve the stability of the hybrid simulator, we include an approximate constraint that removes all clouds above the tropopause. This helps prevent unrealistic cloud accumulation in the upper atmosphere and reduces error growth in hybrid simulations. This constraint is implemented directly in the hybrid simulator and does not alter the model architecture and training.

F.3.5 SOURCES OF ONLINE UNCERTAINTY IN HYBRID SIMULATIONS

Uncertainty from Sampling Model Checkpoints: Previous studies, such as Ott et al. (2020); Wang et al. (2022b), have shown that improved offline skill can benefit online error, but the online error is not fully constrained by offline skill. This means different checkpoints with very similar offline skill can exhibit varying online stability and error. A trial-and-error approach is often used to identify the checkpoint with the best online performance. For

subtle sensitivities, hundreds of trials can become important to detect downstream signals of hybrid climate error from upstream ML noise (Lin et al., 2023).

To account for some of this online uncertainty, we trained three MLP models with different loss functions and learning rate schedules:

- The first model used Mean Absolute Error (MAE) loss, with an initial learning rate of 1×10^{-3} , reduced by a factor of 0.3162 every 7 epochs for a total of 28 epochs.
- The second model used the same learning rate schedule but a standard Huber loss with $\delta = 1$.
- The third model also used Huber loss but with a different learning rate schedule: starting at 1×10^{-3} , using a ReduceOnPlateau scheduler with a patience of 3 epochs and a reduction factor of 0.3162 for a total of 20 epochs. This was followed by manually reducing the learning rate to 1×10^{-4} for fine-tuning over 12 more epochs with a patience of 0 epochs and a reduction factor of 0.5.

Similarly, we trained three versions of the baseline U-Net model and three versions of the U-Net-expanded-constrained models:

- The first used MAE loss, with an initial learning rate of 1×10^{-4} , reduced by a factor of 0.5 every 3 epochs for a total of 16 epochs.
- The second model used the same learning rate schedule but a standard Huber loss with $\delta = 1$.
- The third used Huber loss with a different learning rate schedule: starting at 1×10^{-4} with a ReduceOnPlateau scheduler with a patience of 3 epochs and a reduction factor of 0.3162 for a total of 20 epochs. For the U-Net-expanded-constrained model, where validation loss had not yet converged after 20 epochs, we manually reduced the learning rate to 5×10^{-5} and perform fine-tuning over 8 more epochs with a patience of 0 epochs and a reduction factor of 0.5.

Uncertainty Due to Atmospheric Stochasticity: The atmosphere is a chaotic system where small random perturbations can grow over time and lead to different weather patterns at weekly timescale. For online evaluation, we do not expect our ML emulator hybrid simulations to reproduce daily patterns but rather to match monthly or yearly mean patterns – i.e. climate, not weather. However, the reference E3SM-MMF simulation’s climate also contains some inherent uncertainty due to the way it is implemented and its stochastic nature. The E3SM-MMF simulator is not bit-for-bit reproducible due to the use of atomic operations, particularly during dimension reductions such as horizontal summation. These operations add numbers in a different random order each time, resulting in round-off errors that lead to non-reproducible outcomes. Tiny numerical differences in the calculations can grow, contributing to small but non-zero uncertainty in monthly atmospheric states. To estimate this atmospheric unpredictability, we ran the climate model three additional times with the same initial conditions and compared their differences to the reference simulation as a baseline uncertainty, which can be viewed as an error floor that the ML emulator simulations should not be expected to ever overcome.

F.4 Challenges and Future Directions in Online Error Optimization

Checkpoint Sensitivity and Persistent Error Patterns: Optimizing the online error, as shown in the Section 5.4 of the main text, presents significant challenges. Unlike offline errors, online errors are non-differentiable and cannot be optimized directly using gradient descent. While we have identified some methods for improving offline error, such as enhancing model architecture and adding physics constraints, can help reduce online errors, these methods are not sufficient on their own. Once the architecture is fixed, we currently rely on checkpoint searches to identify the checkpoint that yields the best online performance. Some error patterns, such as zonal-mean cloud bias at latitudes greater than 30N or 30S, are sensitive to the choice of checkpoint. For example, we observed checkpoints that do not exhibit the significant positive liquid cloud bias near 60N seen in Figure 7l in the main text. However, other error patterns, such as the stratospheric dipole temperature bias in high latitudes (Figure 7c in the main text) and drying vapor and liquid cloud biases in the tropics (Figures 7f and 7l in the main text), are persistent and seem so far immune to checkpoint search.

Exploring Gradient-Free and Differentiable Methods: Fully optimizing these online errors remains an open question and an important challenge for the community. Promising approaches might include gradient-free methods, such as imitation learning and online learning, and it would be interesting to explore whether these could further optimize these bias patterns (Ross et al., 2011; Rasp, 2020; Kelp et al., 2022; Lopez-Gomez et al., 2022; Pahlavan et al., 2024; Christopoulos et al., 2024). Another approach involves making the online error differentiable by either training a differentiable emulator for all the physics outside the CRM or rewriting the entire numerical climate simulator in a differentiable manner, as demonstrated by Kochkov et al. (2024). With a model that can be integrated in time in a differentiable way, it would be possible to optimize multi-step losses using gradient descent. However this is a nontrivial effort for a fully-featured climate simulator.

Appendix G. Other Related Work

Several benchmark datasets have been developed to facilitate AI tasks in weather and climate. ClimateNet (Prabhat et al., 2021) and Extremeweather (Racah et al., 2017) were both designed for AI-based feature detection of extreme weather events in forecasts of Earth’s future climate made using conventional climate models. WeatherBench 2 (Rasp et al., 2024) provides data specifically designed for data-driven weather forecasting, focusing on periods ranging from 3 to 5 days into the future. PDEBench (Takamoto et al., 2023) provides data from numerical simulations of several partial differential equations (PDEs) for benchmarking AI PDE emulators. ClimateBench (Watson-Parris et al., 2022) was designed for emulators that produce annual mean global predictions of temperature and precipitation given greenhouse gas concentrations and emissions. The ClimateBench provides data from only one climate model, while ClimateSet (Kaltenborn et al., 2023) expands on the ML tasks in ClimateBench by providing a large-scale dataset with inputs and outputs from 36 climate models. ClimART (Cachay et al., 2021) was designed for the development of radiative energy transfer parameterization emulators for use in weather and climate modeling. These benchmark datasets play a vital role in advancing AI and ML research within the weather and climate domains.

ClimSim, a dataset for parameterization emulators trained on high-resolution data from small-scale embedded models, is unique compared to other benchmark datasets designed for emulators in climate simulation (ClimateBench, ClimateSet, ClimART, and PDEBench). While PDEBench provides data for developing AI emulators of the same PDEs commonly used in climate simulation, ClimSim is uniquely tailored to address the challenging task of replacing a sophisticated parameterization for the combined effects of clouds, rain, radiation, and storms. Specifically, models trained using ClimSim will learn to emulate the nonlinear effect of clouds, rain, and storms resolved on the 1 km (20 s) space (time) scale, which is a collection of hundreds of equations rather than one, to represent their upscale impacts on the 100 km (30 min) scale. Hybrid simulation is also the goal of ClimART, which is designed specifically for the narrower and less computationally costly task of radiative energy transfer parameterization, rather than cloud and rain emulators. ClimateBench, on the other hand, is not an attempt at hybrid simulation, but rather for “whole-model” emulators that reproduce the annual mean global predictions of climate that a conventional climate model would simulate given unseen greenhouse gas concentrations and emissions. This does not attempt to sidestep Moore’s Law or admit previously unattainable resolution, i.e., any error or bias related to the parameterizations used to create the training data are part of what is learned by the emulator.

In contrast, the goal of ClimSim is to develop an emulator for the *explicitly resolved* effect of clouds and storms on climate, so that, down the road, the emulator can be used to replace parameterizations in a climate model, enabling more realistic climate simulation without the typical computational overhead. ClimSim builds off work by a few climate scientists who have been exploring since 2017 to apply ML for hybrid multi-scale climate modeling. Gentine et al. (2018) first demonstrated that using simple ML models, and a simple atmosphere test-bed, certain atmospheric patterns of convective heating and moistening could be effectively predicted, particularly in the tropics and mid-latitude storm tracks. However, when these models were integrated into broader climate simulations, except for lucky fits that demonstrated the exciting potential for success (Rasp et al., 2018), issues related to stability arose, a common problem when constructing hybrid climate models. Various methods were tried to improve the stability, such as coupling multiple models together and searching for better model architectures (Brenowitz et al., 2020; Ott et al., 2020). These efforts led to improved error rates in the predictions. More recently, researchers have expanded this work into real-world settings, using more advanced ML architectures (Han et al., 2020; Mooers et al., 2021; Wang et al., 2022b; Han et al., 2023). Wang et al. (2022a) and Han et al. (2023) even managed to create a deep-learning model that showed hybrid stability over 5 years to a decade under real-world conditions. While these hybrid models had a few biases, they were successful in capturing some aspects of climate variability. Additionally, work has been done to compress input data to avoid causal confounders while maintaining accuracy (Iglesias-Suarez et al., 2023), use latent representations that account for stochasticity (Behrens et al., 2022), and enforce physical constraints within these models (Beucler et al., 2021), all of which could potentially improve their reliability.

Appendix H. Extra Figures and Tables

H.1 MLP with Expanded Target Variables

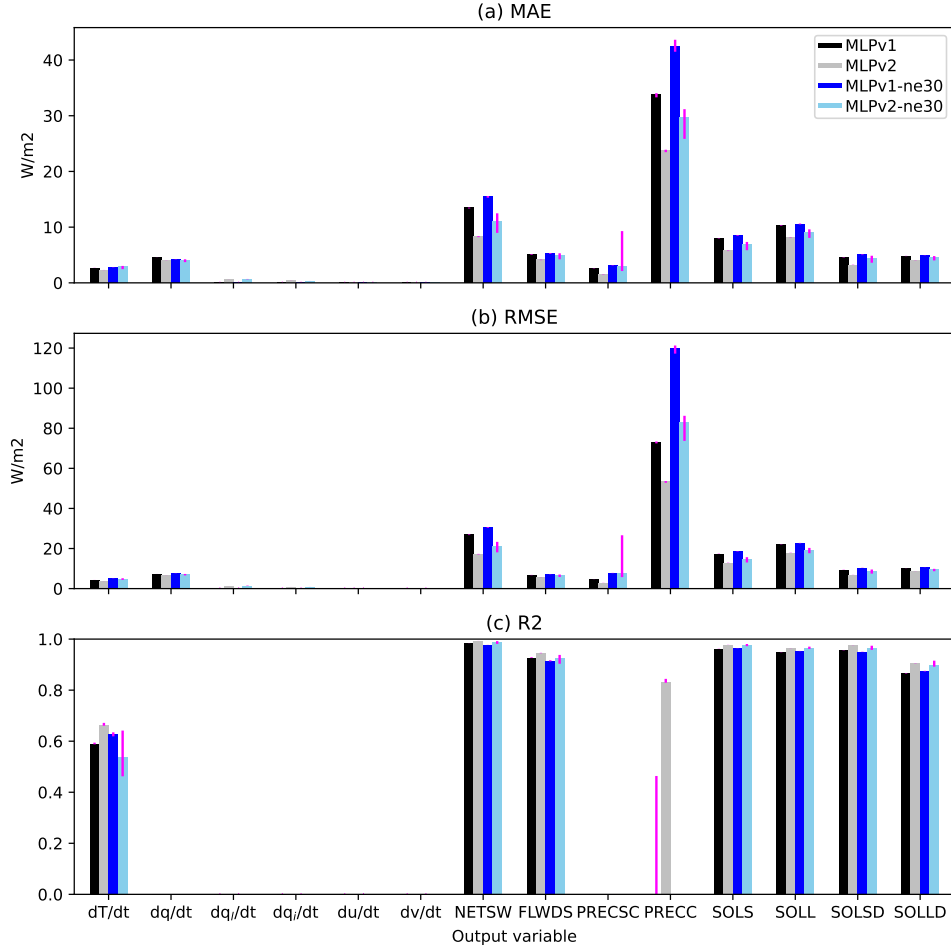


Figure 14: Equivalent to the supplementary Figure 11 in the Appendix, but for comparing the MLPv1 (subset emulation) and the MLPv2 (full vector emulation). In addition, MLP models trained with the high-resolution dataset (ne30) are shown here: MLPv1-ne30 and MLPv2-ne30. Bars show the median of the performance of top-20 models selected from the hyperparamter search ($>8,000$ trials), and magenta error bars show the range of the top-20 model performance.

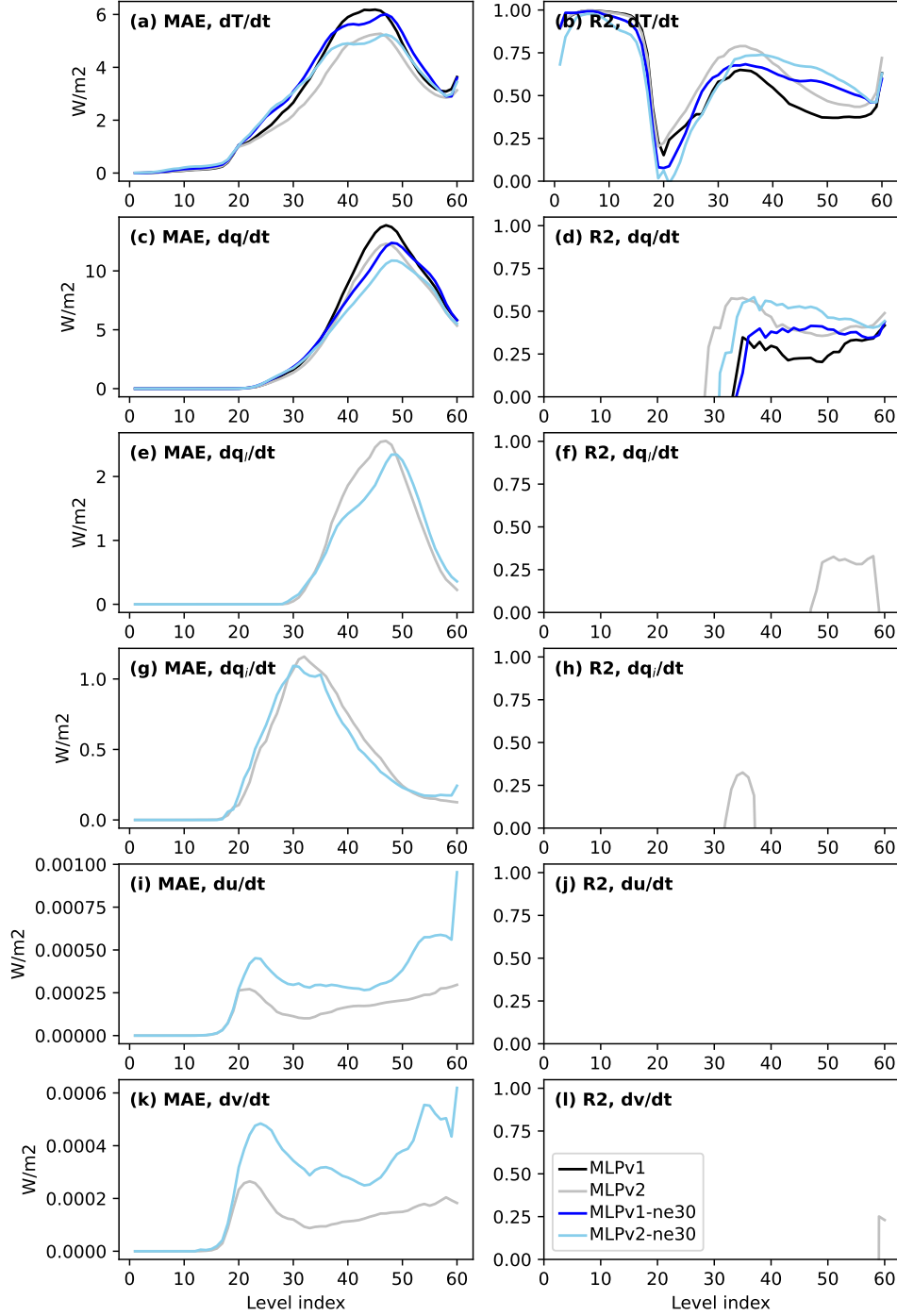


Figure 15: Equivalent to Figure 2, but for comparing the MLP v1 (subset emulation) and the MLP v2 (full vector emulation). In addition, MLP models trained with the high-resolution dataset (ne30) are shown here: MLPv1-ne30 and MLPv2-ne30. Out of the top model pools, MLP models shown in this figure are randomly chosen for visualization.

H.2 Scatter Plots

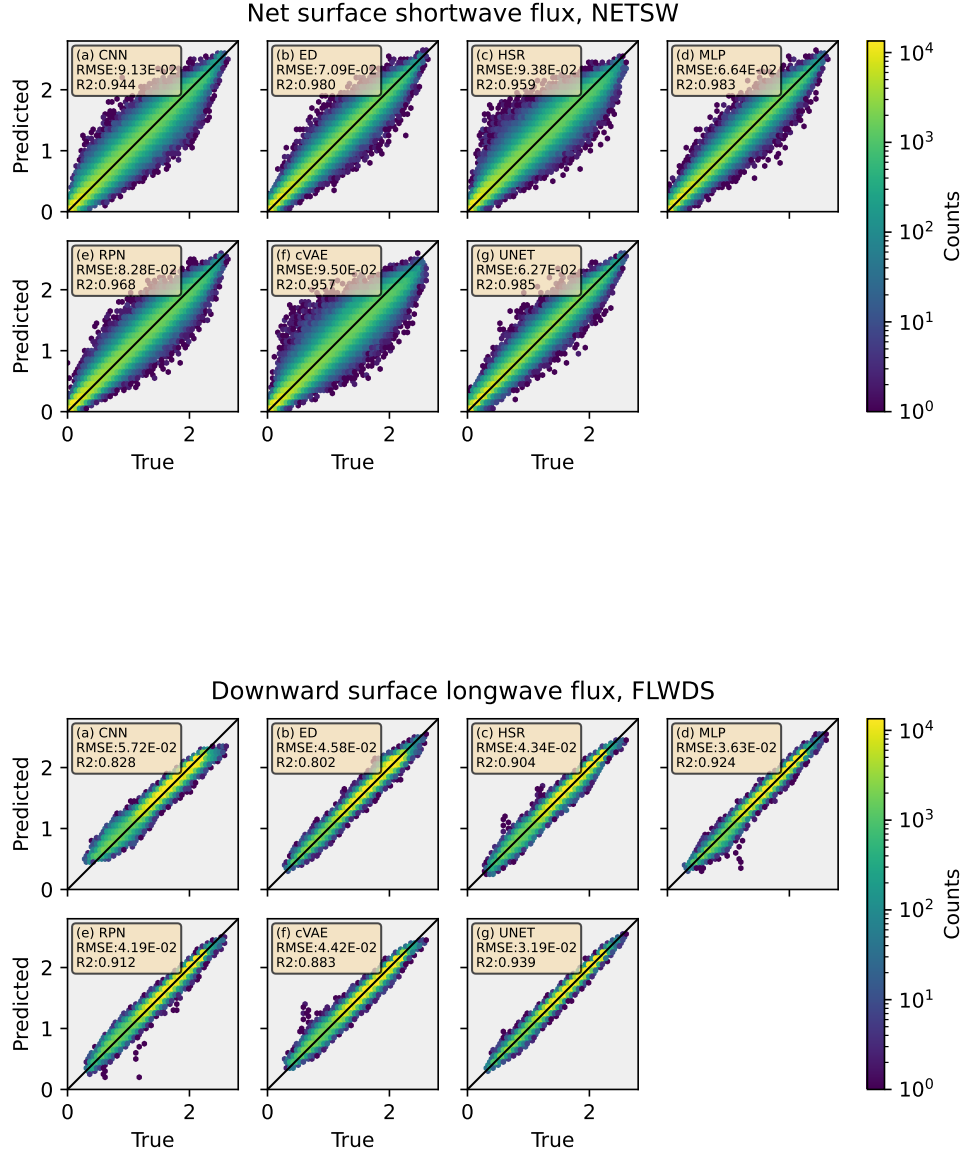


Figure 16: Hexagonally-binned representation of 2D target variables comparing the climate model simulation (“true”; x-axis) with the ML model prediction (“predicted”; y-axis). The color of each hexagonal bin corresponds to the number of data points enclosed.

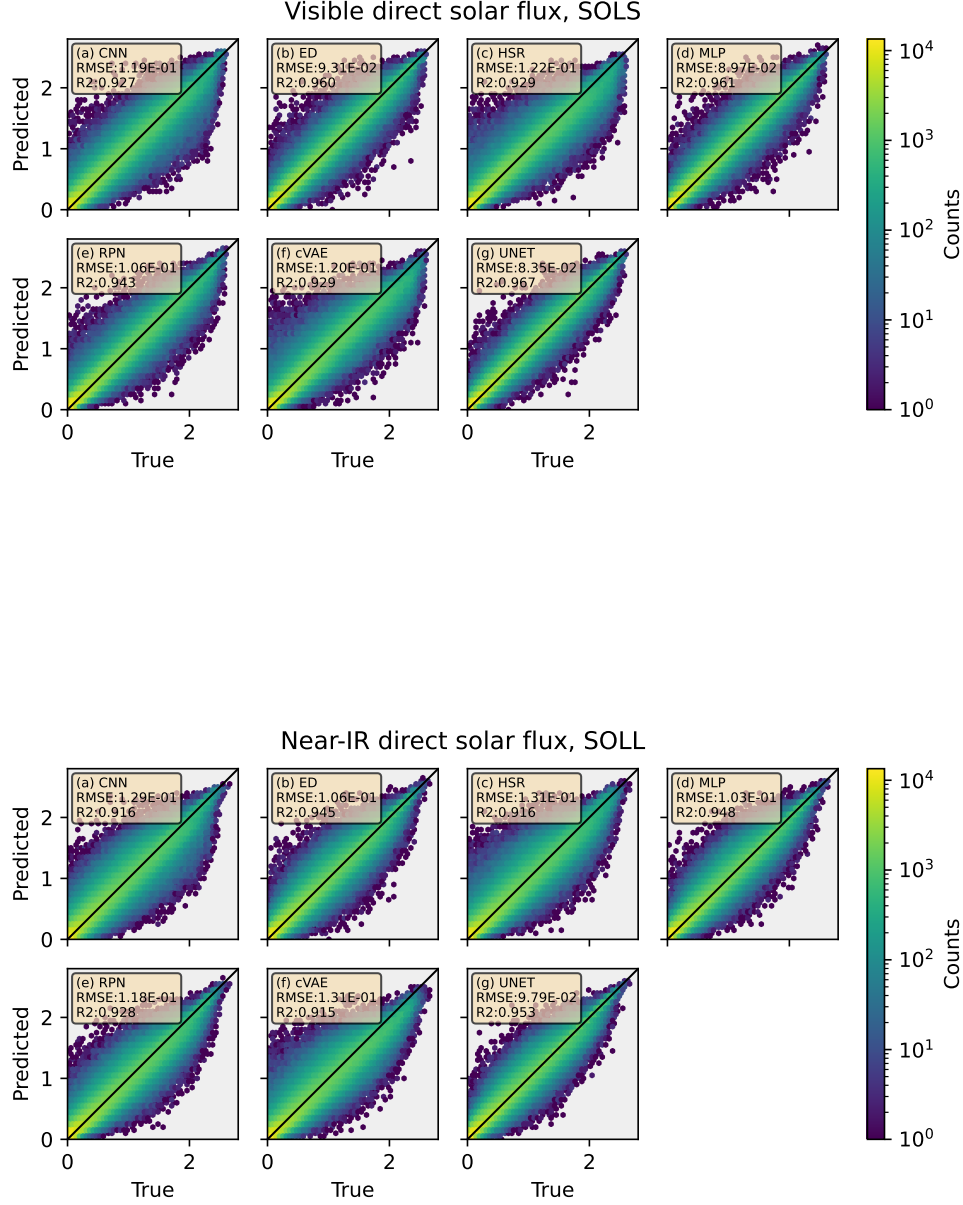


Figure 17: Hexagonally-binned representation of 2D target variables comparing the climate model simulation (“true”; x-axis) with the ML model prediction (“predicted”; y-axis). The color of each hexagonal bin corresponds to the number of data points enclosed.

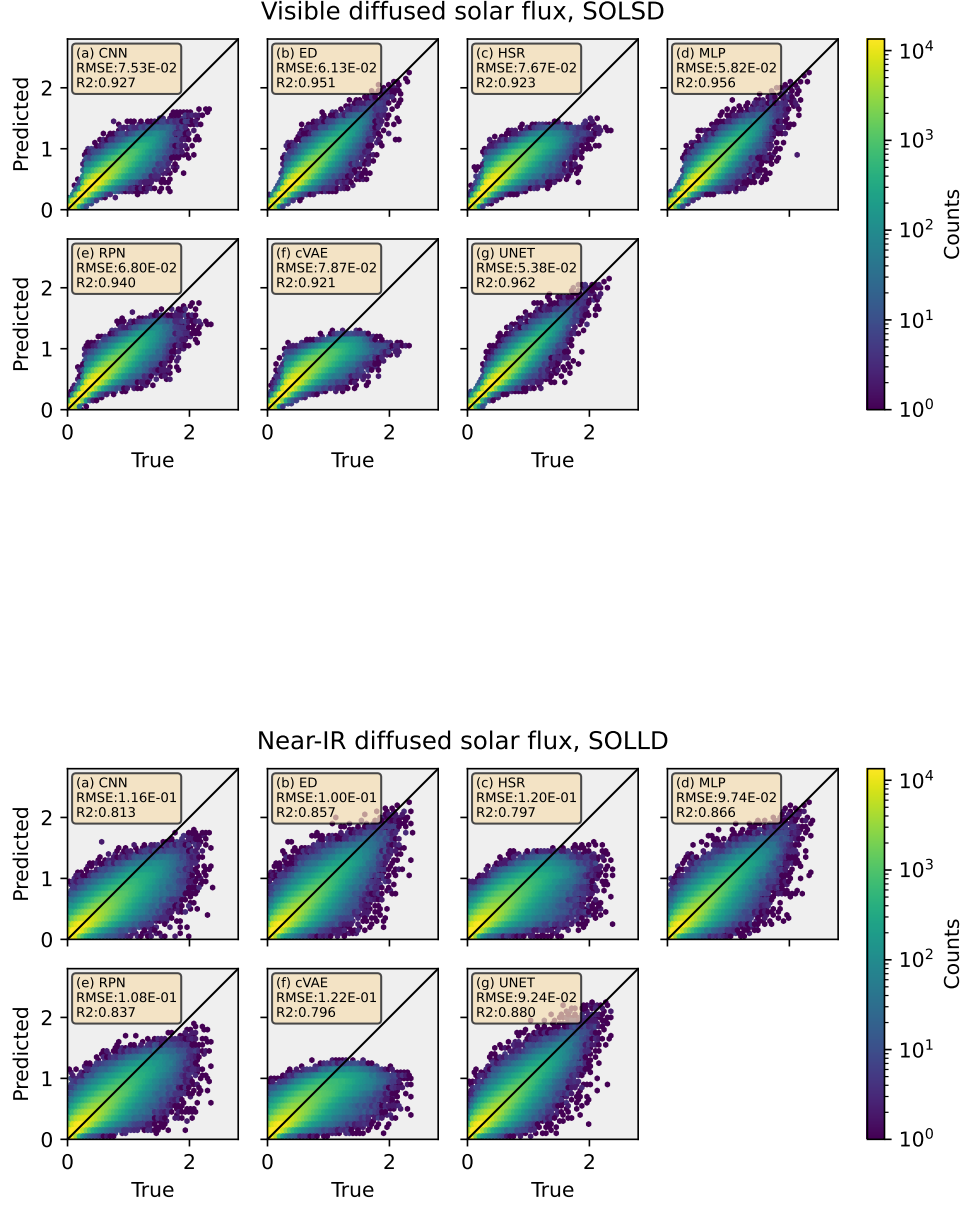


Figure 18: Hexagonally-binned representation of 2D target variables comparing the climate model simulation (“true”; x-axis) with the ML model prediction (“predicted”; y-axis). The color of each hexagonal bin corresponds to the number of data points enclosed.

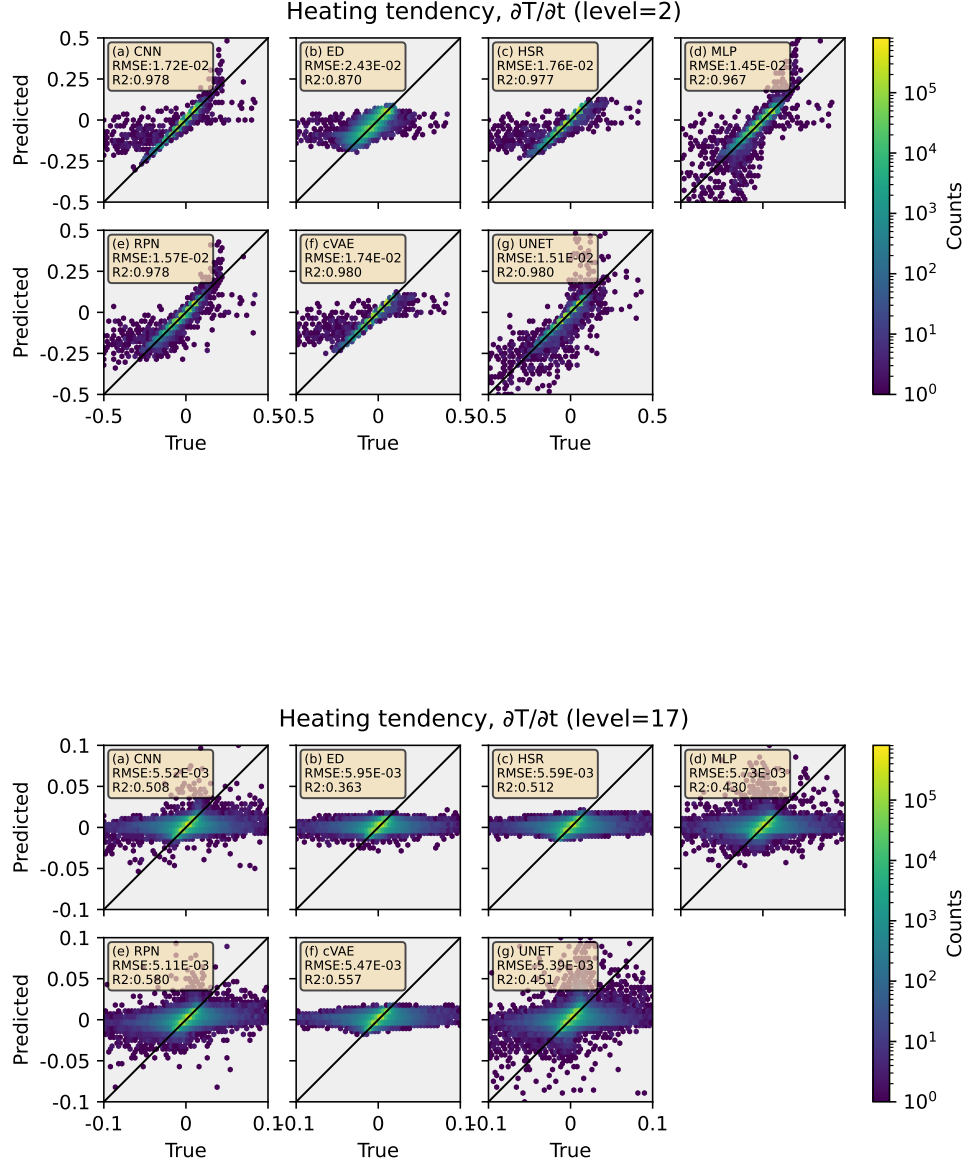


Figure 19: Hexagonally-binned representation of 3D (vertically-resolved) target variables comparing the climate model simulation ("true"; x-axis) with the ML model prediction ("predicted"; y-axis) at four different vertical levels. The color of each hexagonal bin corresponds to the number of data points enclosed.

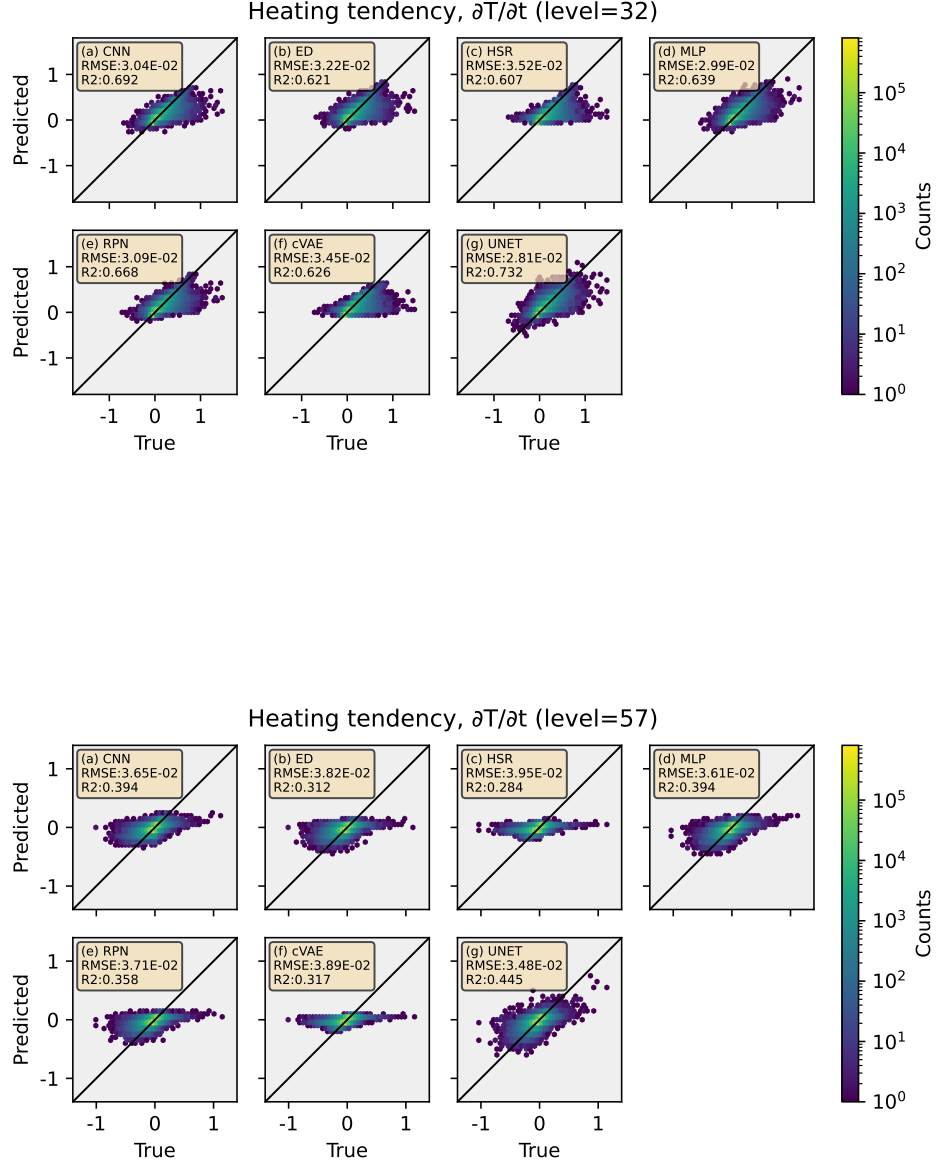


Figure 20: Hexagonally-binned representation of 3D (vertically-resolved) target variables comparing the climate model simulation (“true”; x-axis) with the ML model prediction (“predicted”; y-axis) at four different vertical levels. The color of each hexagonal bin corresponds to the number of data points enclosed.

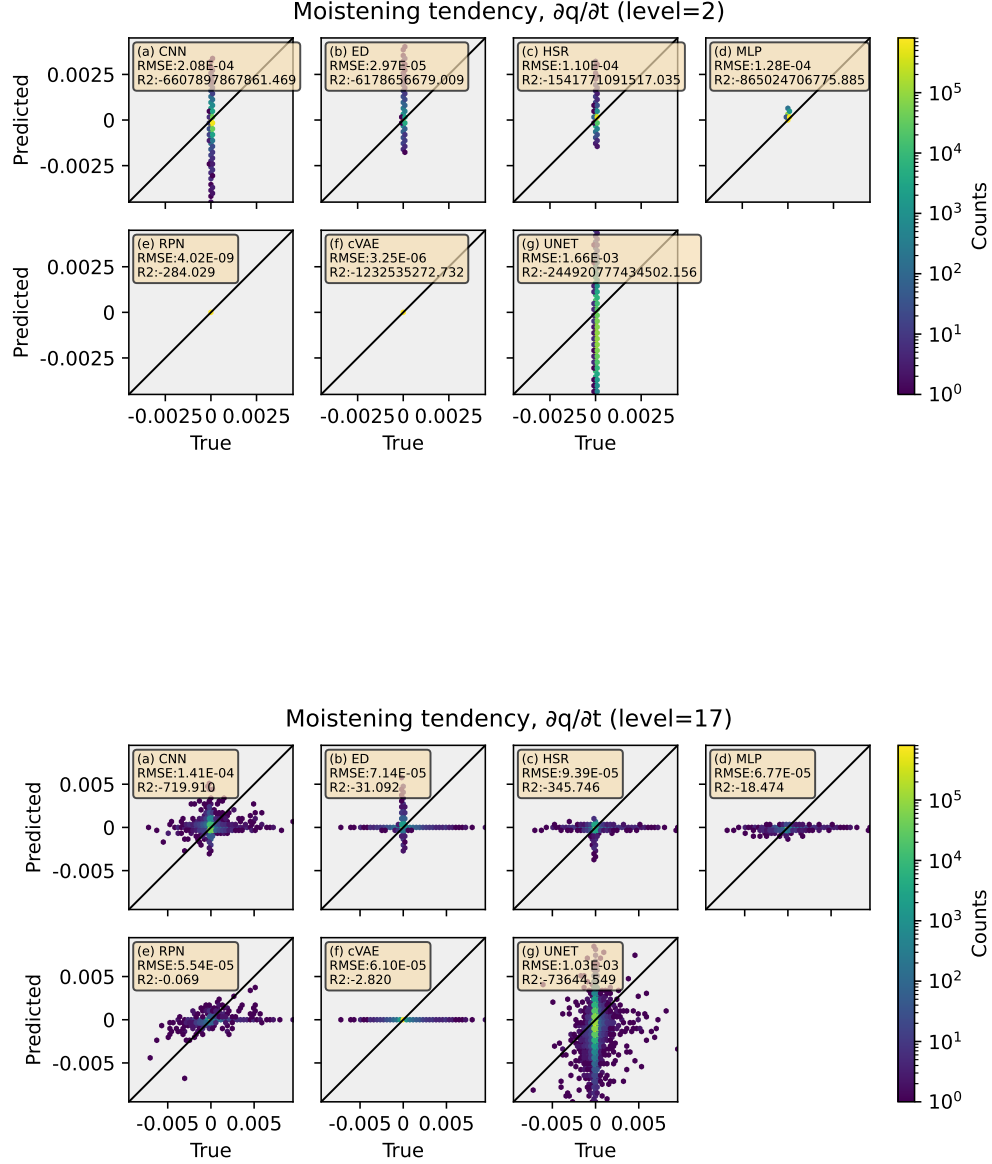


Figure 21: Hexagonally-binned representation of 3D (vertically-resolved) target variables comparing the climate model simulation ("true"; x-axis) with the ML model prediction ("predicted"; y-axis) at four different vertical levels. The color of each hexagonal bin corresponds to the number of data points enclosed.

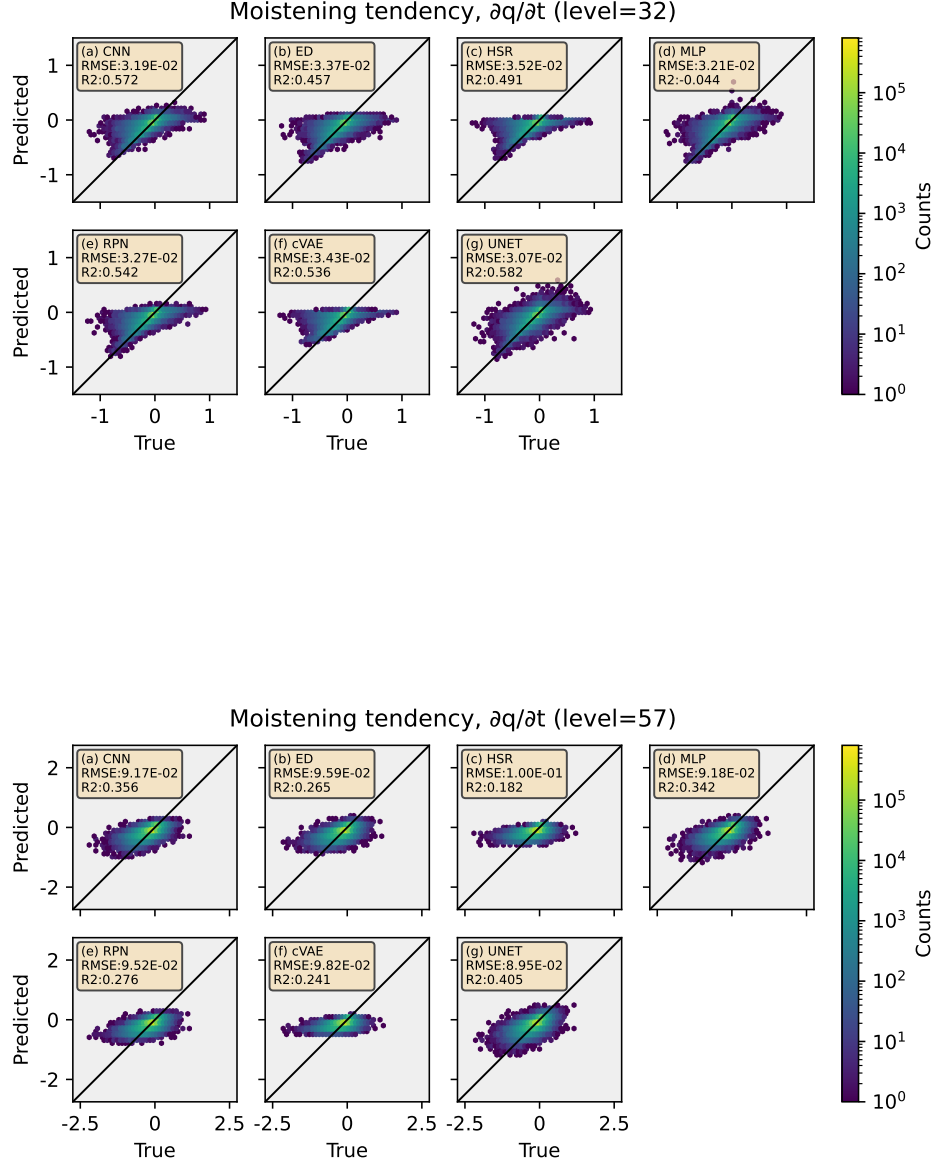


Figure 22: Hexagonally-binned representation of 3D (vertically-resolved) target variables comparing the climate model simulation ("true"; x-axis) with the ML model prediction ("predicted"; y-axis) at four different vertical levels. The color of each hexagonal bin corresponds to the number of data points enclosed.

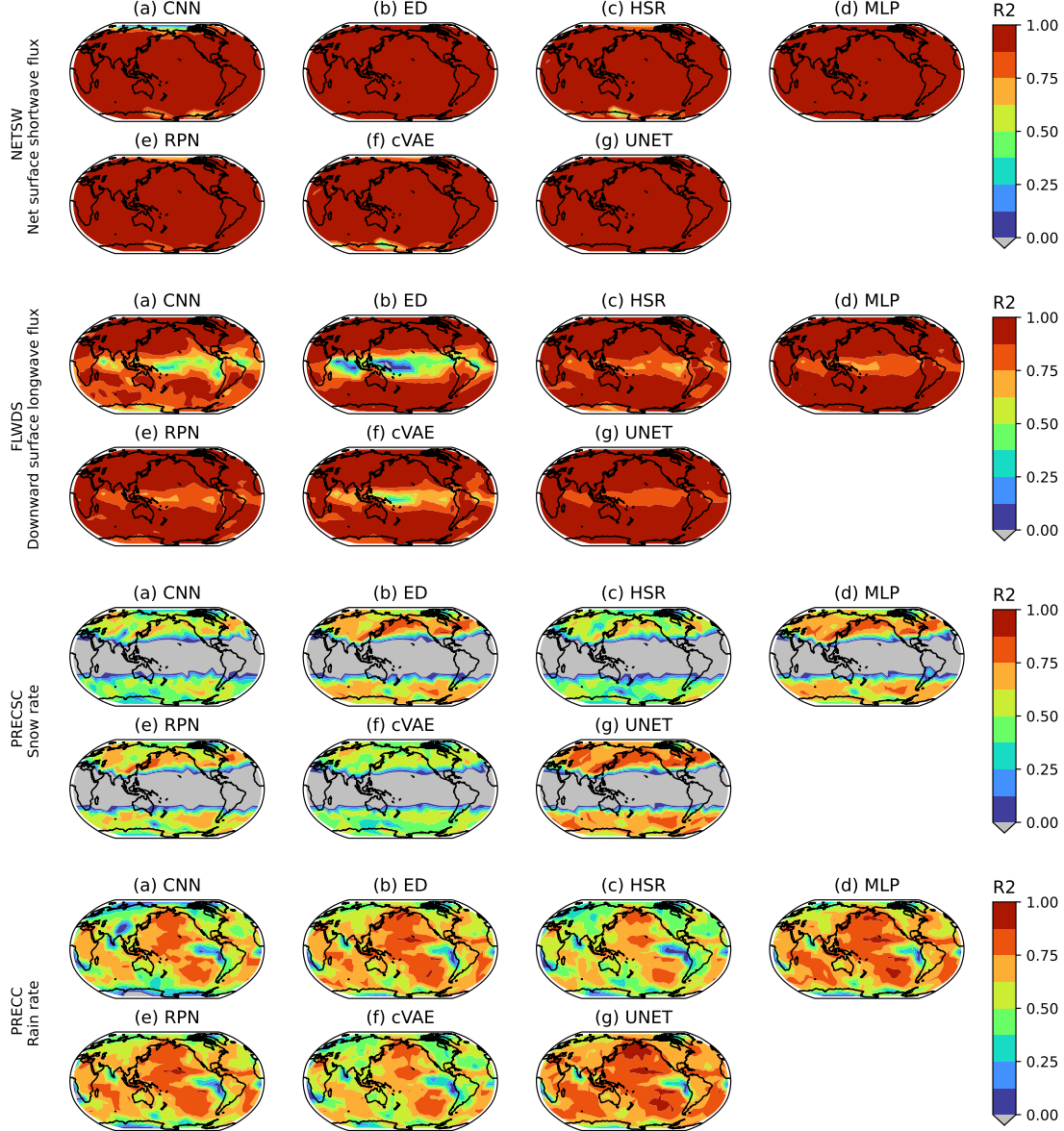
H.3 Global Maps of R^2 

Figure 23: Global maps of R^2 of baseline models (built on the low-res, real-geography dataset). Grey shading shows locations with negative R^2 values.

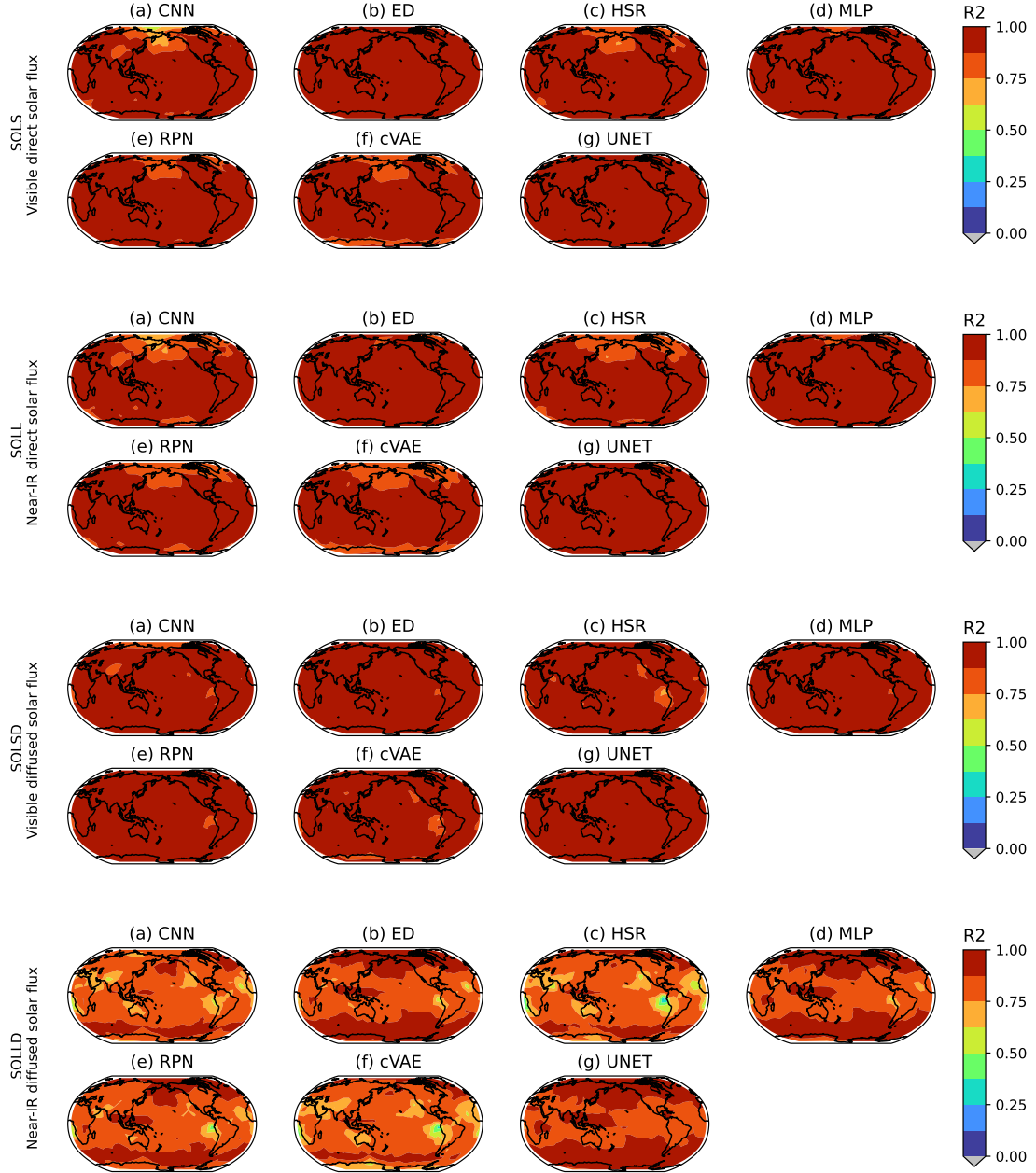


Figure 24: Global maps of R^2 of baseline models (built on the low-res, real-geography dataset). Grey shading shows locations with negative R^2 values.

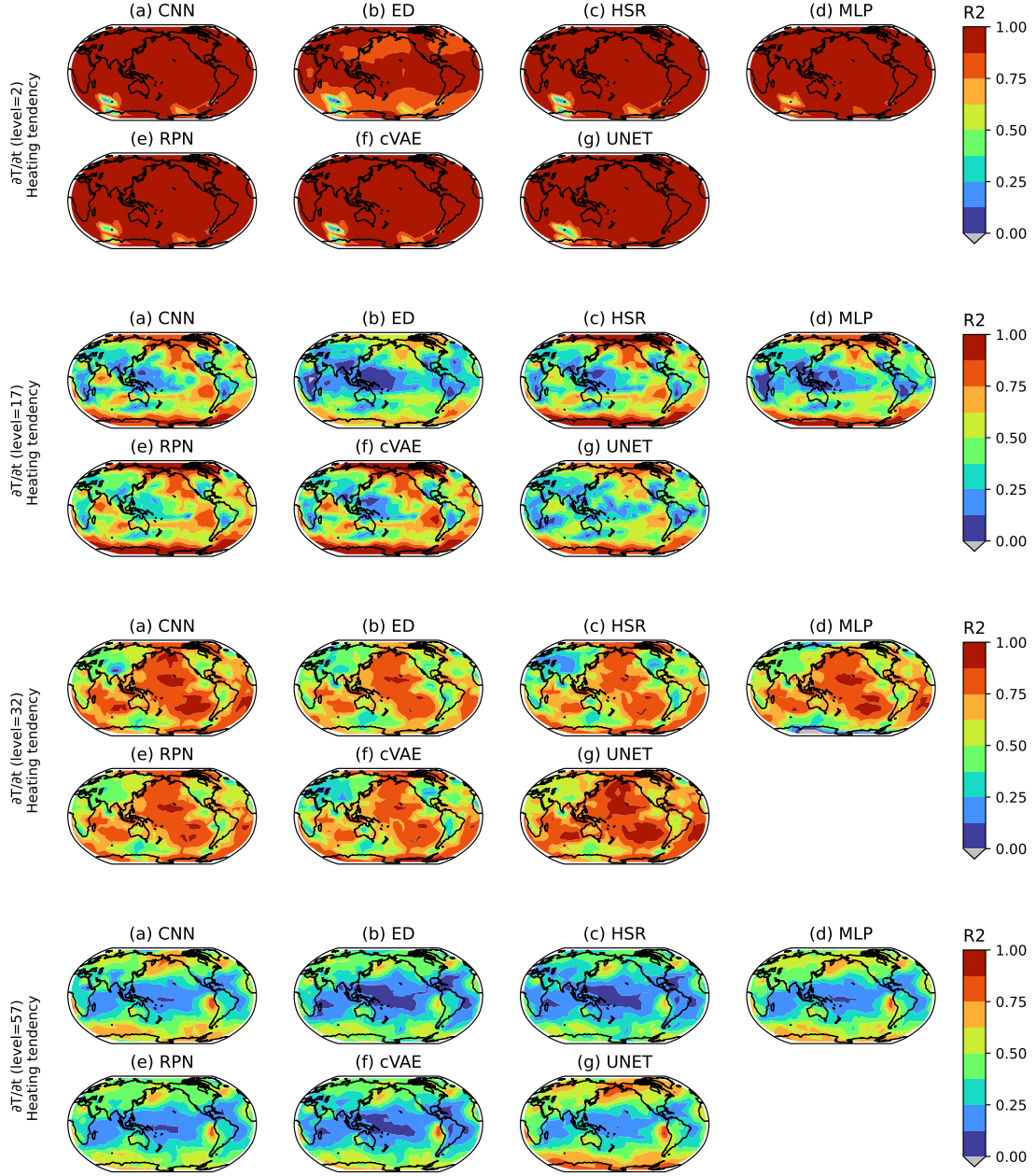


Figure 25: Global maps of R^2 of baseline models (built on the low-res, real-geography dataset). Grey shading shows locations with negative R^2 values.

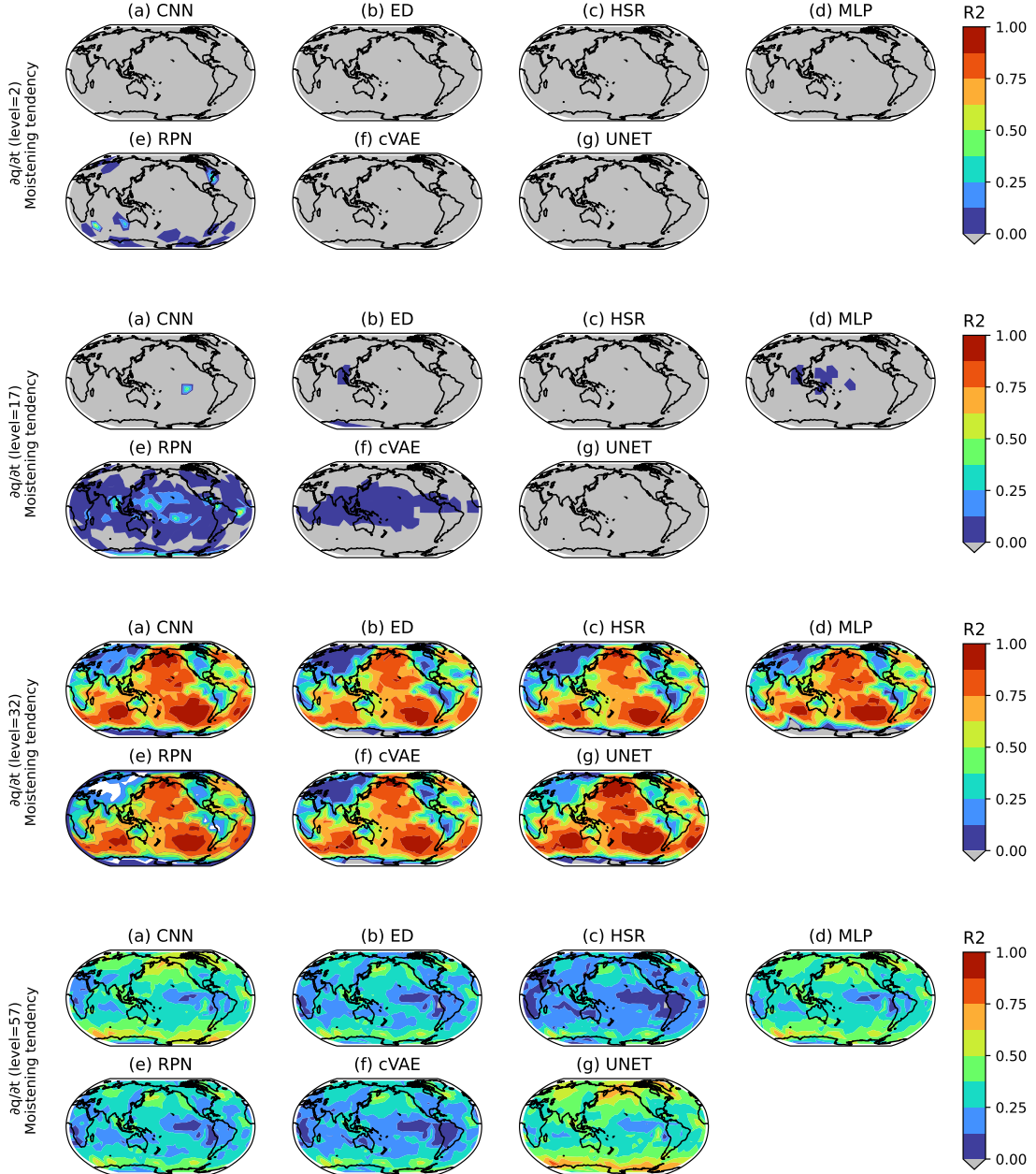


Figure 26: Global maps of R^2 of baseline models (built on the low-res, real-geography dataset). Grey shading shows locations with negative R^2 values.

Appendix I. Datasheet

Motivation

1. **For what purpose was the dataset created?** *Our benchmark dataset was created to serve as a foundation for developing robust frameworks that emulate parameterizations for cloud and extreme rainfall physics and their interaction with other sub-resolution processes.*
2. **Who created the dataset and on behalf of which entity?** *The dataset was developed by a consortium of climate scientists and ML researchers listed in the author list.*
3. **Who funded the creation of the dataset?** *The main funding body is the National Science Foundation (NSF) Science and Technology Center (STC) Learning the Earth with Artificial Intelligence and Physics (LEAP). Other funding sources of individual authors are listed in the acknowledgment section of the main text.*

Distribution

1. **Will the dataset be distributed to third parties outside of the entity (e.g., company, institution, organization) on behalf of which the dataset was created?** *Yes, the dataset is open to the public.*
2. **How will the dataset will be distributed (e.g., tarball on website, API, GitHub)?** *The dataset will be distributed through Hugging Face and the code used for developing baseline models through GitHub.*
3. **Have any third parties imposed IP-based or other restrictions on the data associated with the instances?** *No.*
4. **Do any export controls or other regulatory restrictions apply to the dataset or to individual instances?** *No.*

Maintenance

1. **Who will be supporting/hosting/maintaining the dataset?** *NSF-STC LEAP will support, host, and maintain the dataset.*
2. **How can the owner/curator/manager of the dataset be contacted (e.g., email address)?** *The owner/curator/manager(s) of the dataset can be contacted through following emails: Sungduk Yu (sungduk@uci.edu), Michael S. Pritchard (mspritch@uci.edu) and LEAP (leap@columbia.edu).*
3. **Is there an erratum?** *No. If errors are found in the future, we will release errata on the main web page for the dataset (<https://leap-stc.github.io/ClimSim>).*
4. **Will the dataset be updated (e.g., to correct labeling errors, add new instances, delete instances)?** *Yes, the datasets will be updated whenever necessary to ensure accuracy, and announcements will be made accordingly. These updates will be posted on the main web page for the dataset (<https://leap-stc.github.io/ClimSim>).*

5. **If the dataset relates to people, are there applicable limits on the retention of the data associated with the instances (e.g., were the individuals in question told that their data would be retained for a fixed period of time and then deleted?)** *N/A*
6. **Will older version of the dataset continue to be supported/hosted/maintained?** *Yes, older versions of the dataset will continue to be maintained and hosted.*
7. **If others want to extend/augment/build on/contribute to the dataset, is there a mechanisms for them to do so?** *No.*

Composition

1. **What do the instance that comprise the dataset represent (e.g., documents, photos, people, countries?)** *Each instance includes both input and output vector pairs. These inputs and outputs are instantaneous snapshots of atmospheric states surrounding detailed numerical calculations to be emulated.*
2. **How many instances are there in total (of each type, if appropriate)?** *The high-resolution dataset (ClimSim_high-res) includes 5,676,480,000 instances, and each low-resolution dataset (ClimSim_low-res and ClimSim_low-res_aqua-planet) includes 100,915,200 instances.*
3. **Does the dataset contain all possible instances or is it a sample of instances from a larger set?** *The datasets contain 80% of all possible instances. The rest 20% are reserved as the holdout test set, which will be released once enough models using ClimSim are developed by independent groups.*
4. **Is there a label or target associated with each instance?** *Yes, each instance includes both input and target (prediction) variables.*
5. **Is any information missing from individual instances?** *No.*
6. **Are there recommended data splits (e.g., training, development/validation, testing)?** *We have a hard split between the training/validation set and the test set. The first 8 simulation years-worth dataset is reserved for the training/validation set, and the last 2 simulation years-worth dataset is reserved for the test set. However, we do not have specific recommendations on the split within the training/validation set.*
7. **Are there any errors, sources of noise, or redundancies in the dataset?** *There is one redundancy. Input variable "state_pmid" is redundant since it is a linear function of "state_ps".*
8. **Is the dataset self-contained, or does it link to or otherwise rely on external resources (e.g., websites, tweets, other datasets)?** *The dataset is self-contained.*
9. **Does the dataset contain data that might be considered confidential?** *No.*
10. **Does the dataset contain data that, if viewed directly, might be offensive, insulting, threatening, or might otherwise cause anxiety?** *No.*

Collection Process

1. **How was the data associated with each instance acquired?** *The data associated with each instance is acquired from a series of simulations of a global climate model called E3SM-MMF. References for E3SM-MMF are provided in Appendix A.2.*
2. **What mechanisms or procedures were used to collect the data (e.g., hardware apparatus or sensor, manual human curation, software program, software API)?** *We used many NVIDIA A100 GPU nodes in a high-performance computing cluster called Perlmutter (operated by the U.S. Department of Energy) to run the E3SM-MMF simulations.*
3. **Who was involved in the data collection process (e.g., students, crowdworkers, contractors) and how were they compensated (e.g., how much were crowdworkers paid)?** *Regular employees (e.g., scientists and postdocs) at UC Irvine, LLNL, and SNL were involved in the data collection process. No crowdworkers were involved during the data collection process.*
4. **Does the dataset relate to people?** *No.*
5. **Did you collect the data from the individuals in questions directly, or obtain it via third parties or other sources (e.g., websites)?** *We obtained the dataset from computer simulations of Earth’s climate.*

Uses

1. **Has the dataset been used for any tasks already?** *No, this dataset has not been used for any tasks yet.*
2. **What (other) tasks could be the dataset be used for?** *Please refer to Section 6 in the main manuscript for other applications.*
3. **Is there anything about the composition of the dataset or the way it was collected and preprocessed/cleaned/labeled that might impact future uses?** *The current composition of the datasets are self-sufficient to build a climate emulator. However, it misses some extra variables, which are not essential for such climate emulators but necessary to strictly enforce physical constraints (see Appendix E.1). We plan to include these extra variables in the next release. Any changes in the next release and update to user guidelines will be documented and shared through the dataset webpage (<https://leap-stc.github.io/ClimSim>).*
4. **Are there tasks for which the dataset should not be used?** *No.*

References

Dmitry Alexeev. alexeedm/pytorch-fortran: Version v0.4, April 2023. URL <https://doi.org/10.5281/zenodo.7851167>.

- Gunnar Behrens, Tom Beucler, Pierre Gentine, Fernando Iglesias-Suarez, Michael Pritchard, and Veronika Eyring. Non-linear dimensionality reduction with a variational encoder decoder to understand convective processes in climate models. *J. Adv. Model. Earth Syst.*, 14(8):e2022MS003130, 2022.
- Gunnar Behrens, Tom Beucler, Fernando Iglesias-Suarez, Sungduk Yu, Pierre Gentine, Michael Pritchard, Mierk Schwabe, and Veronika Eyring. Simulating atmospheric processes in earth system models and quantifying uncertainties with deep learning multi-member and stochastic parameterizations. *arXiv preprint arXiv:2402.03079*, 2025.
- James J Benedict and David A Randall. Structure of the madden–julian oscillation in the superparameterized cam. *J. Atmos. Sci.*, 66(11):3277–3296, 2009.
- Tom Beucler, Michael Pritchard, Stephan Rasp, Jordan Ott, Pierre Baldi, and Pierre Gentine. Enforcing analytic constraints in neural networks emulating physical systems. *Phys. Rev. Lett.*, 126(9):098302, 2021.
- Tom Beucler, Pierre Gentine, Janni Yuval, Ankitesh Gupta, Liran Peng, Jerry Lin, Sungduk Yu, Stephan Rasp, Fiaz Ahmed, Paul A O’Gorman, et al. Climate-invariant machine learning. *Science Advances*, 10(6):eadj7250, 2024.
- Mohamed Aziz Bhouri, Michael Joly, Robert Yu, Soumalya Sarkar, and Paris Perdikaris. Scalable bayesian optimization with high-dimensional outputs using randomized prior networks, 2023a. arxiv:2302.07260.
- Mohamed Aziz Bhouri, Liran Peng, Michael S Pritchard, and Pierre Gentine. Multi-fidelity climate model parameterization for better generalization and extrapolation. *arXiv.org*, 2023b.
- Boris Bonev, Thorsten Kurth, Christian Hundt, Jaideep Pathak, Maximilian Baust, Karthik Kashinath, and Anima Anandkumar. Spherical fourier neural operators: Learning stable dynamics on the sphere. In *Proc. ICLR*, 2023.
- Michael P. Brenner, Jeff D. Eldredge, and Jonathan B. Freund. Perspective on machine learning for advancing fluid mechanics. *Phys. Rev. Fluids*, 4:100501, 2019.
- Noah D Brenowitz, Tom Beucler, Michael Pritchard, and Christopher S Bretherton. Interpreting and stabilizing machine-learning parameterizations of convection. *J. Atmos. Sci.*, 77(12):4357–4375, 2020.
- Christopher S Bretherton, Brian Henn, Anna Kwa, Noah D Brenowitz, Oliver Watt-Meyer, Jeremy McGibbon, W Andre Perkins, Spencer K Clark, and Lucas Harris. Correcting coarse-grid weather and climate models by machine learning from global storm-resolving simulations. *J. Adv. Model. Earth Syst.*, 14(2):e2021MS002794, 2022.
- Salva Rühling Cachay, Venkatesh Ramesh, Jason N. S. Cole, Howard Barker, and David Rolnick. Climart: A benchmark dataset for emulating atmospheric radiative transfer in weather and climate models, 2021. arxiv:2111.14671.

- Cambridge-ICCS. A library for coupling (py)torch machine learning models to fortran, 2025. URL <https://github.com/Cambridge-ICCS/FTorch>.
- Costa Christopoulos, Ignacio Lopez-Gomez, Tom Beucler, Yair Cohen, Charles Kawczynski, Oliver RA Dunbar, and Tapio Schneider. Online learning of entrainment closures in a hybrid machine learning parameterization. *Journal of Advances in Modeling Earth Systems*, 16(11):e2024MS004485, 2024.
- Spencer K Clark, Noah D Brenowitz, Brian Henn, Anna Kwa, Jeremy McGibbon, W Andre Perkins, Oliver Watt-Meyer, Christopher S Bretherton, and Lucas M Harris. Correcting a 200 km resolution climate model in multiple climates by machine learning from 25 km resolution simulations. *Journal of Advances in Modeling Earth Systems*, 14(9):e2022MS003219, 2022a.
- Spencer K Clark, Noah D Brenowitz, Brian Henn, Anna Kwa, Jeremy McGibbon, W Andre Perkins, Oliver Watt-Meyer, Christopher S Bretherton, and Lucas M Harris. Correcting a 200 km resolution climate model in multiple climates by machine learning from 25 km resolution simulations. *J. Adv. Model. Earth Syst.*, 14(9), September 2022b.
- Frances V. Davenport, Marshall Burke, and Noah S. Diffenbaugh. Contribution of historical precipitation change to us flood damages. *Proc. Natl. Acad. Sci. USA*, 118(4):e2017524118, 2021.
- Peter D Dueben, Martin G Schultz, Matthew Chantry, David John Gagne, David Matthew Hall, and Amy McGovern. Challenges and benchmark datasets for machine learning in the atmospheric sciences: Definition, status, and outlook. *Artificial Intelligence for the Earth Systems*, 1(3):e210002, 2022.
- DOE E3SM Project. Energy exascale earth system model v2.1.0. [Computer Software] <https://doi.org/10.11578/E3SM/dc.20230110.5>, 2023.
- Imme Ebert-Uphoff, David R Thompson, Ibrahim Demir, Yulia R Gel, Anuj Karpatne, Mariana Guereque, Vipin Kumar, Enrique Cabral-Cano, and Padhraic Smyth. A vision for the development of benchmarks to bridge geoscience and data science. In *17th International Workshop on Climate Informatics*, 2017.
- Kerry A Emanuel. *Atmospheric convection*. 1994.
- Veronika Eyring, Sandrine Bony, Gerald A Meehl, Catherine A Senior, Bjorn Stevens, Ronald J Stouffer, and Karl E Taylor. Overview of the coupled model intercomparison project phase 6 (cmip6) experimental design and organization. *Geoscientific Model Development*, 9(5):1937–1958, 2016.
- Veronika Eyring, Lisa Bock, Axel Lauer, Mattia Righi, Manuel Schlund, Bouwe Andela, Enrico Arnone, Omar Bellprat, Björn Brötz, Louis-Philippe Caron, Nuno Carvalhais, Irene Cionni, Nicola Cortesi, Bas Crezee, Edouard L. Davin, Paolo Davini, Kevin Debeire, Lee de Mora, Clara Deser, David Docquier, Paul Earnshaw, Carsten Ehbrecht, Bettina K. Gier, Nube Gonzalez-Reviriego, Paul Goodman, Stefan Hagemann, Steven Hardiman, Birgit Hassler, Alasdair Hunter, Christopher Kadow, Stephan Kindermann, Sujan Koirala, Nikolay

- Koldunov, Quentin Lejeune, Valerio Lembo, Tomas Lovato, Valerio Lucarini, François Massonnet, Benjamin Müller, Amarjiit Pandde, Núria Pérez-Zanón, Adam Phillips, Valeriu Predoi, Joellen Russell, Alistair Sellar, Federico Serva, Tobias Stacke, Ranjini Swaminathan, Verónica Torralba, Javier Vegas-Regidor, Jost von Hardenberg, Katja Weigel, and Klaus Zimmermann. Earth System Model Evaluation Tool (ESMValTool) v2.0 – an extended set of large-scale diagnostics for quasi-operational and comprehensive evaluation of Earth system models in CMIP. *Geoscientific Model Development*, 13(7):3383–3438, 2020. doi: 10.5194/gmd-13-3383-2020. URL <https://doi.org/10.5194/gmd-13-3383-2020>.
- Veronika Eyring, Vimal Mishra, Gary P. Griffith, Lei Chen, Trevor Keenan, Merritt R. Turetsky, Sally Brown, Frank Jotzo, Frances C. Moore, and Sander van der Linden. Reflections and projections on a decade of climate science. *Nat. Clim. Change*, 11(4): 279–285, 2021.
- Veronika Eyring, William D. Collins, Pierre Gentine, Elizabeth A. Barnes, Marcelo Barreiro, Tom Beucler, Marc Bocquet, Christopher S. Bretherton, Hannah M. Christensen, David John Gagne, David Hall, Dorit Hammerling, Stephan Hoyer, Fernando Iglesias-Suarez, Ignacio Lopez-Gomez, Marie C. McGraw, Gerald A. Meehl, Maria J. Molina, Claire Monteleoni, Juliane Mueller, Michael S. Pritchard, David Rolnick, Jakob Runge, Philip Stier, Oliver Watt-Meyer, Katja Weigel, Rose Yu, and Laure Zanna. Pushing the frontiers in climate modeling and analysis with machine learning. *Nature Climate Change*, accepted, 2024a.
- Veronika Eyring, Pierre Gentine, Gustau Camps-Valls, David M Lawrence, and Markus Reichstein. Ai-empowered next-generation multiscale climate modelling for mitigation and adaptation. *Nature Geoscience*, pages 1–9, 2024b.
- CAT Ferro. Fair scores for ensemble forecasts. *Quarterly Journal of the Royal Meteorological Society*, 140(683):1917–1923, 2014.
- Erich M Fischer, Sonia I Seneviratne, Pier Luigi Vidale, Daniel Lüthi, and Christoph Schär. Soil moisture–atmosphere interactions during the 2003 european summer heat wave. *J. Clim.*, 20(20):5081–5099, 2007.
- W Lawrence Gates, James S Boyle, Curt Covey, Clyde G Dease, Charles M Doutriaux, Robert S Drach, Michael Fiorino, Peter J Gleckler, Justin J Hnilo, Susan M Marlais, et al. An overview of the results of the atmospheric model intercomparison project (amip i). *Bulletin of the American Meteorological Society*, 80(1):29–56, 1999.
- Pierre Gentine, Mike Pritchard, Stephan Rasp, Gael Reinaudi, and Galen Yacalis. Could machine learning break the convection parameterization deadlock? *Geophysical Research Letters*, 45(11):5742–5751, 2018.
- Pierre Gentine, Veronika Eyring, and Tom Beucler. Deep learning for the parametrization of subgrid processes in climate models. In *Deep Learning for the Earth Sciences*, pages 307–314. 2021.

- Wojciech W Grabowski and Piotr K Smolarkiewicz. Crcp: A cloud resolving convection parameterization for modeling the tropical convecting atmosphere. *Phys. D: Nonlinear Phenom.*, 133(1-4):171–178, 1999.
- Arthur Grundner, Tom Beucler, Pierre Gentine, Fernando Iglesias-Suarez, Marco A. Giorgetta, and Veronika Eyring. Deep Learning Based Cloud Cover Parameterization for ICON. *Journal of Advances in Modeling Earth Systems*, 14(12):e2021MS002959, 2022. doi: <https://doi.org/10.1029/2021MS002959>.
- Arthur Grundner, Tom Beucler, Pierre Gentine, and Veronika Eyring. Data-driven equation discovery of a cloud cover parameterization, 2023. arxiv:2304.08063.
- Selma B. Guerreiro, Hayley J. Fowler, Renaud Barbero, Seth Westra, Geert Lenderink, Stephen Blenkinsop, Elizabeth Lewis, and Xiao Feng Li. Detection of continental-scale intensification of hourly rainfall extremes. *Nat. Clim. Change*, 8(9):803–807, 2018.
- Yilun Han, Guang J Zhang, Xiaomeng Huang, and Yong Wang. A moist physics parameterization based on deep learning. *J. Adv. Model. Earth Syst.*, 12(9):e2020MS002076, 2020.
- Yilun Han, Guang J Zhang, and Yong Wang. An ensemble of neural networks for moist physics processes, its generalizability and stable integration. *Journal of Advances in Modeling Earth Systems*, 15(10):e2022MS003508, 2023.
- Walter M Hannah, Christopher R Jones, Benjamin R Hillman, Matthew R Norman, David C Bader, Mark A Taylor, LR Leung, Michael S Pritchard, Mark D Branson, Guangxing Lin, et al. Initial results from the super-parameterized e3sm. *Journal of Advances in Modeling Earth Systems*, 12(1):e2019MS001863, 2020.
- Walter M. Hannah, Andrew M. Bradley, Oksana Guba, Qi Tang, Jean-Christophe Golaz, and Jon Wolfe. Separating physics and dynamics grids for improved computational efficiency in spectral element earth system models. *J. Adv. Model. Earth Syst.*, 13(7):e2020MS002419, 2021.
- Walter M. Hannah, Kyle G. Pressel, Mikhail Ovchinnikov, and Gregory S. Elsaesser. Checkerboard patterns in e3smv2 and e3sm-mmfv2. *Geosci. Model Dev.*, 15(9):6243–6257, 2022.
- Hans Hersbach, Bill Bell, Paul Berrisford, Shoji Hirahara, András Horányi, Joaquín Muñoz-Sabater, Julien Nicolas, Carole Peubey, Raluca Radu, Dinand Schepers, et al. The era5 global reanalysis. *Quarterly Journal of the Royal Meteorological Society*, 146(730):1999–2049, 2020.
- Helge Heuer, Mierk Schwabe, Pierre Gentine, Marco A Giorgetta, and Veronika Eyring. Interpretable multiscale machine learning-based parameterizations of convection for icon. *Journal of Advances in Modeling Earth Systems*, 16(8):e2024MS004398, 2024.
- Torsten Hoeffler, Bjorn Stevens, Andreas F Prein, Johanna Baehr, Thomas Schulthess, Thomas F Stocker, John Taylor, Daniel Klocke, Pekka Manninen, Piers M Forster, et al. Earth virtualization engines: a technical perspective. *Computing in Science & Engineering*, 25(3):50–59, 2023.

- Cathy Hohenegger, Peter Korn, Leonidas Linardakis, René Redler, Reiner Schnur, Panagiotis Adamidis, Jiawei Bao, Swantje Bastin, Milad Behraves, Martin Bergemann, et al. Iconsapphire: simulating the components of the earth system and their interactions at kilometer and subkilometer scales. *Geoscientific Model Development*, 16(2):779–811, 2023.
- Zeyuan Hu, Akshay Subramaniam, Zhiming Kuang, Jerry Lin, Sungduk Yu, Walter M. Hannah, Noah D. Brenowitz, Josh Romero, and Michael S Pritchard. Stable machine-learning parameterization of subgrid processes in a comprehensive atmospheric model learned from embedded convection-permitting simulations. *arXiv preprint arXiv:2407.00124*, 2025.
- Fernando Iglesias-Suarez, Pierre Gentine, Breixo Solino-Fernandez, Tom Beucler, Michael Pritchard, Jakob Runge, and Veronika Eyring. Causally-informed deep learning to improve climate models and projections, 2023. arxiv:2304.12952.
- IPCC. *Climate Change 2021: The Physical Science Basis. Contribution of Working Group I to the Sixth Assessment Report of the Intergovernmental Panel on Climate Change*. 2021.
- Julia Kaltenborn, Charlotte Lange, Venkatesh Ramesh, Philippe Brouillard, Yaniv Gurwicz, Chandni Nagda, Jakob Runge, Peer Nowack, and David Rolnick. Climateset: A large-scale climate model dataset for machine learning. *Advances in Neural Information Processing Systems*, 36:21757–21792, 2023.
- Makoto M Kelp, Daniel J Jacob, Haipeng Lin, and Melissa P Sulprizio. An online-learned neural network chemical solver for stable long-term global simulations of atmospheric chemistry. *Journal of Advances in Modeling Earth Systems*, 14(6):e2021MS002926, 2022.
- Marat Khairoutdinov, Charlotte DeMott, and David Randall. Evaluation of the simulated interannual and subseasonal variability in an amip-style simulation using the csu multiscale modeling framework. *J. Clim.*, 21(3):413–431, 2008.
- Marat F Khairoutdinov and David A Randall. Cloud resolving modeling of the arm summer 1997 iop: Model formulation, results, uncertainties, and sensitivities. *J. Atmos. Sci.*, 60(4): 607–625, 2003.
- Byungsoo Kim, Vinicius C. Azevedo, Nils Thuerey, Theodore Kim, Markus Gross, and Barbara Solenthaler. Deep fluids: A generative network for parameterized fluid simulations. *Comput. Graph. Forum*, 38(2):59–70, 2019.
- Diederik P. Kingma and Max Welling. Auto-encoding variational bayes. In *Proc. ICLR*, 2014.
- Dmitrii Kochkov, Janni Yuval, Ian Langmore, Peter Norgaard, Jamie Smith, Griffin Mooers, Milan Klöwer, James Lottes, Stephan Rasp, Peter Düben, et al. Neural general circulation models for weather and climate. *Nature*, 632(8027):1060–1066, 2024.
- Gabriel J Kooperman, Michael S Pritchard, Melissa A Burt, Mark D Branson, and David A Randall. Robust effects of cloud superparameterization on simulated daily rainfall intensity statistics across multiple versions of the community earth system model. *J. Adv. Model. Earth Syst.*, 8(1):140–165, 2016.

- Zhiming Kuang. Linear time-invariant models of a large cumulus ensemble. *Journal of the Atmospheric Sciences*, 81(3):605–627, 2024.
- Birgit Kühbacher, Fernando Iglesias-Suarez, Niki Kilbertus, and Veronika Eyring. Towards physically consistent deep learning for climate model parameterizations. *arXiv preprint arXiv:2406.03920*, 2024.
- Anna Kwa, Spencer K Clark, Brian Henn, Noah D Brenowitz, Jeremy McGibbon, Oliver Watt-Meyer, W Andre Perkins, Lucas Harris, and Christopher S Bretherton. Machine-learned climate model corrections from a global storm-resolving model: Performance across the annual cycle. *J. Adv. Model. Earth Syst.*, 15(5):e2022MS003400, 2023.
- Remi Lam, Alvaro Sanchez-Gonzalez, Matthew Willson, Peter Wirsberger, Meire Fortunato, Alexander Pritzel, Suman Ravuri, Timo Ewalds, Ferran Alet, Zach Eaton-Rosen, Weihua Hu, Alexander Merose, Stephan Hoyer, George Holland, Jacklynn Stott, Oriol Vinyals, Shakir Mohamed, and Peter Battaglia. Graphcast: Learning skillful medium-range global weather forecasting, 2022. *arxiv:2212.12794*.
- Lisha Li, Kevin Jamieson, Giulia DeSalvo, Afshin Rostamizadeh, and Ameet Talwalkar. Hyperband: A novel bandit-based approach to hyperparameter optimization, 2018. *arxiv:1603.06560*.
- Zongyi Li, Nikola Kovachki, Kamyar Azizzadenesheli, Burigede Liu, Kaushik Bhattacharya, Andrew Stuart, and Anima Anandkumar. Fourier neural operator for parametric partial differential equations, 2021. *arxiv:2010.08895*.
- Zongyi Li, Hongkai Zheng, Nikola Kovachki, David Jin, Haoxuan Chen, Burigede Liu, Kamyar Azizzadenesheli, and Anima Anandkumar. Physics-informed neural operator for learning partial differential equations, 2023. *arxiv:2111.03794*.
- Jerry Lin, Sungduk Yu, Tom Beucler, Pierre Gentine, David Walling, and Mike Pritchard. Systematic sampling and validation of machine learning-parameterizations in climate models. *arXiv preprint arXiv:2309.16177*, 2023.
- Jerry Lin, Zeyuan Hu, Sungduk Yu, Michael S Pritchard, Ritwik Gupta, Tian Zheng, Walter Hannah, Laura Mansfield, Yongquan Qu, Margarita Geleta, Molly Lopez, Maja Rudolph, Ashley Chow, and Walter Reade. Leap - atmospheric physics using ai (climsim), 2024. URL <https://kaggle.com/competitions/leap-atmospheric-physics-ai-climsim>.
- Johnny Wei-Bing Lin and J David Neelin. Influence of a stochastic moist convective parameterization on tropical climate variability. *Geophysical research letters*, 27(22): 3691–3694, 2000.
- Johnny Wei-Bing Lin and J David Neelin. Toward stochastic deep convective parameterization in general circulation models. *Geophysical research letters*, 30(4), 2003.
- Julia Ling, Andrew Kurzawski, and Jeremy Templeton. Reynolds averaged turbulence modelling using deep neural networks with embedded invariance. *J. Fluid Mech.*, 807: 155–166, 2016.

- Ignacio Lopez-Gomez, Costa Christopoulos, Haakon Ludvig Langeland Ervik, Oliver RA Dunbar, Yair Cohen, and Tapio Schneider. Training physics-based machine-learning parameterizations with gradient-free ensemble kalman methods. *Journal of Advances in Modeling Earth Systems*, 14(8):e2022MS003105, 2022.
- Alexandra Sasha Luccioni and Alex Hernandez-Garcia. Counting carbon: A survey of factors influencing the emissions of machine learning. *arXiv preprint arXiv:2302.08476*, 2023.
- Björn Lütjens, Catherine H. Crawford, Campbell D Watson, Christopher Hill, and Dava Newman. Multiscale neural operator: Learning fast and grid-independent pde solvers, 2022. arxiv:2207.11417.
- Jonathan F MacArt, Justin Sirignano, and Jonathan B Freund. Embedded training of neural-network subgrid-scale turbulence models. *Phys. Rev. Fluids*, 6(5):050502, 2021.
- Cristian Martinez-Villalobos and J. David Neelin. Regionally high risk increase for precipitation extreme events under global warming. *Sci. Rep.*, 13:5579, 2023.
- Griffin Mooers, Michael Pritchard, Tom Beucler, Jordan Ott, Galen Yacalis, Pierre Baldi, and Pierre Gentine. Assessing the potential of deep learning for emulating cloud superparameterization in climate models with real-geography boundary conditions. *J. Adv. Model. Earth Syst.*, 13(5):e2020MS002385, 2021.
- Griffin Mooers, Tom Beucler, Mike Pritchard, and Stephan Mandt. Understanding extreme precipitation changes through unsupervised machine learning. *arXiv preprint arXiv:2211.01613*, 2022.
- Griffin Mooers, Mike Pritchard, Tom Beucler, Prakhar Srivastava, Harshini Mangipudi, Liran Peng, Pierre Gentine, and Stephan Mandt. Comparing storm resolving models and climates via unsupervised machine learning. *Scientific Reports*, 13(1):22365, 2023.
- J David Neelin, Ole Peters, Johnny W-B Lin, Katrina Hales, and Christopher E Holloway. Rethinking convective quasi-equilibrium: Observational constraints for stochastic convective schemes in climate models. *Philosophical Transactions of the Royal Society A: Mathematical, Physical and Engineering Sciences*, 366(1875):2579–2602, 2008.
- J David Neelin, Cristian Martinez-Villalobos, Samuel N Stechmann, Fiaz Ahmed, Gang Chen, Jesse M Norris, Yi-Hung Kuo, and Geert Lenderink. Precipitation extremes and water vapor: Relationships in current climate and implications for climate change. *Current Clim. Change Rep.*, 8(1):17–33, 2022.
- J David Neelin, John P Krasting, Aparna Radhakrishnan, Jessica Liptak, Thomas Jackson, Yi Ming, Wenhao Dong, Andrew Gettelman, Danielle R Coleman, Eric D Maloney, et al. Process-oriented diagnostics: Principles, practice, community development, and common standards. *Bulletin of the American Meteorological Society*, 104(8):E1452–E1468, 2023.
- Ruijia Niu, Dongxia Wu, Kai Kim, Yi-An Ma, Duncan Watson-Parris, and Rose Yu. Multi-fidelity residual neural processes for scalable surrogate modeling. 2024.

- Matthew R Norman, David C Bader, Christopher Eldred, Walter M Hannah, Benjamin R Hillman, Christopher R Jones, Jungmin M Lee, LR Leung, Isaac Lyngaas, Kyle G Pressel, et al. Unprecedented cloud resolution in a gpu-enabled full-physics atmospheric climate simulation on olcf’s summit supercomputer. *Int. J. High Perform. Compu. Appl.*, 36(1): 93–105, 2022.
- Tom O’Malley, Elie Bursztein, James Long, François Chollet, Haifeng Jin, Luca Invernizzi, et al. Kerastuner. <https://github.com/keras-team/keras-tuner>, 2019.
- Ian Osband, John Aslanides, and Albin Cassirer. Randomized prior functions for deep reinforcement learning, 2018. arxiv:1806.03335.
- Jordan Ott, Mike Pritchard, Natalie Best, Erik Linstead, Milan Curcic, and Pierre Baldi. A fortran-keras deep learning bridge for scientific computing, 2020. arxiv:2004.10652.
- Paul A O’Gorman. Precipitation extremes under climate change. *Current Clim. Change Rep.*, 1:49–59, 2015.
- Hamid A Pahlavan, Pedram Hassanzadeh, and M Joan Alexander. Explainable offline-online training of neural networks for parameterizations: A 1d gravity wave-qbo testbed in the small-data regime. *Geophysical Research Letters*, 51(2):e2023GL106324, 2024.
- Pardeep Pall, MR Allen, and Dáithí A Stone. Testing the clausius–clapeyron constraint on changes in extreme precipitation under co 2 warming. *Climate Dynamics*, 28:351–363, 2007.
- Jaideep Pathak, Shashank Subramanian, Peter Harrington, Sanjeev Raja, Ashesh Chattopadhyay, Morteza Mardani, Thorsten Kurth, David Hall, Zongyi Li, Kamyar Azizzadenesheli, Pedram Hassanzadeh, Karthik Kashinath, and Animashree Anandkumar. Fourcastnet: A global data-driven high-resolution weather model using adaptive fourier neural operators, 2022. arxiv:2202.11214.
- Angeline G. Pendergrass and Dennis L. Hartmann. Two modes of change of the distribution of rain. *J. Clim.*, 27(22):8357–8371, 2014.
- W Andre Perkins, Noah D Brenowitz, Christopher S Bretherton, and Jacqueline M Nugent. Emulation of cloud microphysics in a climate model. *Journal of Advances in Modeling Earth Systems*, 16(4):e2023MS003851, 2024.
- Devayani Prabhat, Karthik Kashinath, Mayur Mudigonda, Sol Kim, Lukas Kapp-Schwoerer, Andre Graubner, Ege Karaismailoglu, Leo von Kleist, Thorsten Kurth, Annette Greiner, Ankur Mahesh, Kevin Yang, Colby Lewis, Jiayi Chen, Andrew Lou, Sathyavat Chandran, Ben Toms, Will Chapman, Katherine Dagon, Christine A Shields, Travis O’Brien, Michael Wehner, and William Collins. Climateset: an expert-labeled open dataset and deep learning architecture for enabling high-precision analyses of extreme weather. *Geosci. Model Dev.*, 14(1):107–124, 2021.
- PyTorch Contributors. Torchscript documentation [software], 2024. URL <https://pytorch.org/docs/stable/jit.html#pytorch-functions-and-modules>.

- Evan Racah, Christopher Beckham, Tegan Maharaj, Samira Ebrahimi Kahou, Prabhat, and Christopher Pal. Extremeweather: A large-scale climate dataset for semi-supervised detection, localization, and understanding of extreme weather events, 2017. arxiv:1612.02095.
- David Randall. *Atmosphere, clouds, and climate*, volume 6. 2012.
- David Randall, Marat Khairoutdinov, Akio Arakawa, and Wojciech Grabowski. Breaking the cloud parameterization deadlock. *Bull. Am. Meteorol. Soc.*, 84(11):1547–1564, 2003.
- David A Randall. Beyond deadlock. *Geophys. Res. Lett.*, 40(22):5970–5976, 2013.
- Stephan Rasp. Coupled online learning as a way to tackle instabilities and biases in neural network parameterizations: general algorithms and lorenz 96 case study (v1. 0). *Geosci. Model Dev.*, 13(5):2185–2196, 2020.
- Stephan Rasp, Michael S Pritchard, and Pierre Gentine. Deep learning to represent subgrid processes in climate models. *Proc. Natl. Acad. Sci. USA*, 115(39):9684–9689, 2018.
- Stephan Rasp, Stephan Hoyer, Alexander Meroze, Ian Langmore, Peter Battaglia, Tyler Russell, Alvaro Sanchez-Gonzalez, Vivian Yang, Rob Carver, Shreya Agrawal, et al. Weatherbench 2: A benchmark for the next generation of data-driven global weather models. *Journal of Advances in Modeling Earth Systems*, 16(6):e2023MS004019, 2024.
- Colorado J. Reed, Ritwik Gupta, Shufan Li, Sarah Brockman, Christopher Funk, Brian Clipp, Kurt Keutzer, Salvatore Candido, Matt Uyttendaele, and Trevor Darrell. Scale-mae: A scale-aware masked autoencoder for multiscale geospatial representation learning, 2023. arxiv:2212.14532.
- Corrado Ronchi, Roberto Iacono, and Pier S Paolucci. The “cubed sphere”: A new method for the solution of partial differential equations in spherical geometry. *Journal of computational physics*, 124(1):93–114, 1996.
- Andrew Ross, Ziwei Li, Pavel Perezhogin, Carlos Fernandez-Granda, and Laure Zanna. Benchmarking of machine learning ocean subgrid parameterizations in an idealized model. *Journal of Advances in Modeling Earth Systems*, 15(1), 2023.
- Stéphane Ross, Geoffrey Gordon, and Drew Bagnell. A reduction of imitation learning and structured prediction to no-regret online learning. In *Proceedings of the fourteenth international conference on artificial intelligence and statistics*, pages 627–635. JMLR Workshop and Conference Proceedings, 2011.
- Clayton Sanford, Anna Kwa, Oliver Watt-Meyer, Spencer K Clark, Noah Brenowitz, Jeremy McGibbon, and Christopher Bretherton. Improving the reliability of ml-corrected climate models with novelty detection. *Journal of Advances in Modeling Earth Systems*, 15(11): e2023MS003809, 2023a.
- Clayton Hendrick Sanford, Anna Kwa, Oliver Watt-Meyer, Spencer Koncius Clark, Noah Domino Brenowitz, Jeremy McGibbon, and Christopher S Bretherton. Improving the reliability of ml-corrected climate models with novelty detection. *Authorea Preprints*, 2023b.

- Tapio Schneider, João Teixeira, Christopher S Bretherton, Florent Brient, Kyle G Pressel, Christoph Schär, and A Pier Siebesma. Climate goals and computing the future of clouds. *Nat. Clim. Change*, 7(1):3–5, 2017.
- Sonia I Seneviratne, Thierry Corti, Edouard L Davin, Martin Hirschi, Eric B Jaeger, Irene Lehner, Boris Orlowsky, and Adriaan J Teuling. Investigating soil moisture–climate interactions in a changing climate: A review. *Earth-Sci. Rev.*, 99(3-4):125–161, 2010.
- Sonia I Seneviratne, Xuebin Zhang, Muhammad Adnan, Wafae Badi, Claudine Dereczynski, A Di Luca, Subimal Ghosh, Iskhaq Iskandar, James Kossin, Sophie Lewis, et al. Weather and Climate Extreme Events in a Changing Climate. In V. Masson-Delmotte, P. Zhai, A. Pirani, S.L. Connors, C. Péan, S. Berger, N. Caud, Y. Chen, L. Goldfarb, M.I. Gomis, M. Huang, K. Leitzell, E. Lonnoy, J.B.R. Matthews, T.K. Maycock, T. Waterfield, O. Yelekçi, R. Yu, , and B. Zhou, editors, *Climate Change 2021: The Physical Science Basis. Contribution of Working Group I to the Sixth Assessment Report of the Intergovernmental Panel on Climate Change*, chapter 11, page 1513–1766. Cambridge University Press, Cambridge, United Kingdom and New York, NY, USA, 2021. URL <https://www.ipcc.ch/report/ar6/wg1/>.
- Steven C Sherwood, Mark J Webb, James D Annan, Kyle C Armour, Piers M Forster, Julia C Hargreaves, Gabriele Hegerl, Stephen A Klein, Kate D Marvel, Eelco J Rohling, et al. An assessment of earth’s climate sensitivity using multiple lines of evidence. *Reviews of Geophysics*, 58(4):e2019RG000678, 2020.
- A Pier Siebesma, Sandrine Bony, Christian Jakob, and Bjorn Stevens. *Clouds and climate: Climate science’s greatest challenge*. 2020.
- Yang Song and Stefano Ermon. Generative modeling by estimating gradients of the data distribution. *Advances in neural information processing systems*, 32, 2019.
- Akshay Subramaniam, Man Long Wong, Raunak D Borker, Sravya Nimmagadda, and Sanjiva K Lele. Turbulence enrichment using physics-informed generative adversarial networks, 2020. arxiv:2003.01907.
- Makoto Takamoto, Timothy Praditia, Raphael Leiteritz, Dan MacKinlay, Francesco Alesiani, Dirk Pflüger, and Mathias Niepert. Pdebench: An extensive benchmark for scientific machine learning, 2023. arxiv:2210.07182.
- Mark Taylor, Peter M Caldwell, Luca Bertagna, Conrad Clevenger, Aaron Donahue, James Foucar, Oksana Guba, Benjamin Hillman, Noel Keen, Jayesh Krishna, et al. The simple cloud-resolving e3sm atmosphere model running on the frontier exascale system. In *Proceedings of the International Conference for High Performance Computing, Networking, Storage and Analysis*, pages 1–11, 2023.
- Claudia Tebaldi, Kevin Debeire, Veronika Eyring, Erich Fischer, John Fyfe, Pierre Friedlingstein, Reto Knutti, Jason Lowe, Brian O’Neill, Benjamin Sanderson, et al. Climate model projections from the Scenario Model Intercomparison Project (ScenarioMIP) of CMIP6. *Earth System Dynamics*, 12(1):253–293, 2021. doi: 10.5194/esd-12-253-2021. URL <https://esd.copernicus.org/articles/12/253/2021/>.

- Stefan N. Tulich. A strategy for representing the effects of convective momentum transport in multiscale models: Evaluation using a new superparameterized version of the weather research and forecast model (sp-wrf). *J. Adv. Model. Earth Syst.*, 7(2):938–962, 2015.
- Peidong Wang, Janni Yuval, and Paul A O’Gorman. Non-local parameterization of atmospheric subgrid processes with neural networks. *J. Adv. Model. Earth Syst.*, 14(10):e2022MS002984, 2022a.
- Xin Wang, Yilun Han, Wei Xue, Guangwen Yang, and Guang J Zhang. Stable climate simulations using a realistic general circulation model with neural network parameterizations for atmospheric moist physics and radiation processes. *Geosci. Model Dev.*, 15(9):3923–3940, 2022b.
- Duncan Watson-Parris, Yuhan Rao, Dirk Olivié, Øyvind Seland, Peer Nowack, Gustau Camps-Valls, Philip Stier, Shahine Bouabid, Maura Dewey, Emilie Fons, et al. Climatebench v1.0: A benchmark for data-driven climate projections. *J. Adv. Model. Earth Syst.*, 14(10):e2021MS002954, 2022.
- Oliver Watt-Meyer, Gideon Dresdner, Jeremy McGibbon, Spencer K Clark, Brian Henn, James Duncan, Noah D Brenowitz, Karthik Kashinath, Michael S Pritchard, Boris Bonev, et al. Ace: A fast, skillful learned global atmospheric model for climate prediction. *arXiv preprint arXiv:2310.02074*, 2023.
- Oliver Watt-Meyer, Brian Henn, Jeremy McGibbon, Spencer K Clark, Anna Kwa, W Andre Perkins, Elynn Wu, Lucas Harris, and Christopher S Bretherton. Ace2: Accurately learning subseasonal to decadal atmospheric variability and forced responses. *arXiv preprint arXiv:2411.11268*, 2024.
- Elliot Wong-Toi, Alex Boyd, Vincent Fortuin, and Stephan Mandt. Understanding pathologies of deep heteroskedastic regression, 2023. arxiv:2306.16717.
- Victor Xing, Corentin Lapeyre, Thomas Jaravel, and Thierry Poinot. Generalization capability of convolutional neural networks for progress variable variance and reaction rate subgrid-scale modeling. *Energies*, 14(16):5096, 2021.
- Yibo Yang, Georgios Kissas, and Paris Perdikaris. Scalable uncertainty quantification for deep operator networks using randomized priors. *Comput. Methods Appl. Mech. Eng.*, 399:115399, 2022.
- Sungduk Yu, Mike Pritchard, Po-Lun Ma, Balwinder Singh, and Sam Silva. Two-step hyperparameter optimization method: Accelerating hyperparameter search by using a fraction of a training dataset. *Artif. Intell. Earth Sys.*, 2023, *Under Review*.
- Sungduk Yu, Walter Hannah, Liran Peng, Jerry Lin, Mohamed Aziz Bhouiri, Ritwik Gupta, Björn Lütjens, Justus C Will, Gunnar Behrens, Julius Busecke, et al. Climsim: A large multi-scale dataset for hybrid physics-ml climate emulation. *Advances in Neural Information Processing Systems*, 36, 2024.
- Janni Yuval and Paul A O’Gorman. Stable machine-learning parameterization of subgrid processes for climate modeling at a range of resolutions. *Nature Comm.*, 11(1):3295, 2020.

Janni Yuval, Paul A O’Gorman, and Chris N Hill. Use of neural networks for stable, accurate and physically consistent parameterization of subgrid atmospheric processes with good performance at reduced precision. *Geophys. Res. Lett.*, 48(6):e2020GL091363, 2021.

Laure Zanna and Thomas Bolton. Data-driven equation discovery of ocean mesoscale closures. *Geophys. Res. Lett.*, 47(17):e2020GL088376, 2020.